The Ion-Neutral Structure of the Lower Atmosphere of Mars

A Thesis

Submitted for the Award of Ph.D. degree of

MOHANLAL SUKHADIA UNIVERSITY

in the

Faculty of Science

By

Ashimananda Modak

Under the Supervision of

Prof. Varun Sheel

PROFESSOR

PLANETARY SCIENCES DIVISION

PHYSICAL RESEARCH LABORATORY, AHMEDABAD, INDIA

DEPARTMENT OF PHYSICS

FACULTY OF SCIENCE

MOHANLAL SUKHADIA UNIVERSITY, UDAIPUR (RAJ)

Year of submission: 2019

DECLARATION

I, **Ashimananda Modak**, S/o Mr. Gurucharan Modak, resident of Room No-B005, PRL Navarangpura Hostel, Ahmedabad – 380009, hereby declare that the research work incorporated in the present thesis entitled "**The Ion-Neutral Structure of the Lower Atmosphere of Mars**" is my own work and is original. This work (in part or in full) has not been submitted to any University for the award of a Degree or a Diploma. I have properly acknowledged the material collected from secondary sources wherever required.

I have properly acknowledged the material collected from the secondary sources wherever required and I have run my entire thesis on the anti-plagiarism software namely, 'iThenticate'.

I solely own the responsibility for the originality of the entire content.

Date:

Ashimananda Modak

(Author)

CERTIFICATE

I feel great pleasure in certifying that the thesis entitled, "**The Ion-Neutral Structure of the Lower Atmosphere of Mars**" embodies a record of the results of investigations carried out by Mr. Ashimananda Modak under my guidance. He has completed the following requirements as per Ph.D regulations of the University.

(a) Course work as per the university rules.
(b) Residential requirements of the university.
(c) Regularly submitted six monthly progress reports.
(d) Presented his work in the departmental committee.
(e) Published minimum of one research paper in a referred research journal.

I recommend the submission of thesis.

Date:

Prof. Varun Sheel
Professor,
Planetary Sciences Division
Physical Research Laboratory,
Ahmedabad - 380 009.

Countersigned by
Head of the Department

Dedicated to my Family

Acknowledgments

The thesis has come to its present form due to noble efforts of many. I sincerely wish to thank all those who gave their support with dedication and have been my teachers, friends, colleagues and family.

I feel much honored in expressing my deepest sense of gratitude to Prof. Varun Sheel under whose able guidance I could shape out my thesis. Without his support the thesis would not have been possible. His constant support, inspiration, encouragement and motivation during this entire work period, accelerated the thesis work. I have been greatly benefitted from his discussions, remarks and suggestions. His positive attitude towards solving scientific problems teaches me a lot. His supervision helped me throughout my research and writing of this thesis.

I am very much indebted to Prof. S.A. Haider, who is also a member of Doctoral Science Committee (DSC) for my thesis work. His suggestions, discussions and motivation in the research area helped me in many ways. His friendly behaviour towards students is also encouraging. I also thank Dr. Lokesh Sahu (DSC) for his support in rigorous reviewing the thesis and fruitful remarks. I thank my DSC members for keeping me motivated for the thesis work.

I would like to thank Prof. Anil Bharadwaj, the current Director, Physical Research Laboratory (PRL), and previous Directors of PRL Profs. Utpal Sarkar and J. N. Goswami. I would also like to thank Prof. P. Janardhan, Dean, PRL for providing me all the support and means necessary to complete the thesis work.

I sincerely thank Dr. M. Roy, Head, Physics Department and Prof. B.L. Ahuja, Dean, Post Graduate Studies, Mohanlal Sukhadia University for their kind cooperation throughout the thesis work. I am also very grateful to Prof. N. Laksmi and Late Prof. K.Venugopalan for their administrative supports.

I am grateful to the faculty of PRL for their encouraging and friendly behaviour which acted as a positive catalysts towards the completion of the work. These include Raghu Rangarajan, Bhas Bapat, Dilip Angom, Niraj Rastogi, Lokesh Sahu, Sanjeev Kumar, S.D. Rindani, S. Mohanty, Namit Mahajan and K. K. Marhas. Their works and concerns kept me highly motivated and eased me at various stages of my thesis work.

I am thankful to the Computer Center staff, namely Jigar sir, Tejas sir, Mishra ji, Samuel sir, Alok sir and others for their extended help regarding computational problems and the use of High Performance Computation (HPC) facility. Most of the modeling and computational work for the thesis have been done on HPC. I cordially appreciate their support for providing me a smooth computational facility. I thank the Computer center

group also for arranging seminars and lectures on various topics which facilitates my knowledge on the various aspects of computational learning.

Thanks are due to Rajesh sir, Venkat sir, Negi ji, Shyam Lal sir and Chinmoy bhaiya for cheerful interactions. Their support at many stages of my stay in PRL kept me fresh. Discussion with them on various topics related to atmospheric science, enriched my knowledge.

I also thank Dr. Bhushit for advice and help during reviews at PRL and Ph.D. registration at Udaipur and also for his concern about my progress.

I am very fortunate to have colleagues like Deepak, Shefali, Siddhi, and Masoom. I thank them for their moral support, and for creating a fun-loving working atmosphere. When in need, instant help and support were provided by our group of colleagues. I am truly indebted to them for their positive support and concerns for me. I also thank the members of the adjacent labs such as Pabari sir, Amit sir, Priybrata da, Alka, Srirag, Sonam and Dinesh for their cooperation in maintaining the work environment for research.

I thank to my batchmates Lalit, Apurv, Venky, Bivin, Jinia, Rajat, Rahul, Sanjay, Manglanand, Pankaj bhalla, Samiran, Ritwik, Prashant, Anand, Newton, Chandana, Deepti and Deepak for the cheerful moments during the period of our course work. I am thankful to them for many memorable experiences. I specially thank Lalit, Jinia, Apurv, Venky and Bivin for their constant support and care.

I thankfully acknowledge all student members of PRL namely, Rohit bhaiya, Arvind bhaiya, Fazlul bhiaya, Ashis bhiaya, Ikshu, Anirban, Manu, Abhaya, Shraddha, Girish(Chhota), Gaurava, Arun Chitra, Yashpal, Aadhi,Lakshmi, Midhun, Bhavya Girish (Bada), Prahalad, Navpreet, Satish, Rukmani, Javir, Ali, Anil, Ashis, Aman, Bhavesh, Bharti, Rupa, Niharika, Vishnu, Nijil, Subir, Kaustav, Nidhi, Akangsha,, Shivangi, Harish, Shivani, and all others for helping me in several ways.

I feel happy to make few recent and new friends at PRL, Sovan, Ramanuj, Sudipto and Tanmoy. Friendship with them keeps me rejuvenated.

Finally, I thank all the members of my family, to whom this thesis is dedicated. Thakurda, Thakuma, Dadu, dida, Jethu, Jethima, Kaku, Kakima, Pishi Pishababu, Baro mama, Late Mejo mama, Chhoto mama and my all cousins Dada, Didi, Chiku, Sathi, Piku, Shankar, Priyanka, Abhishek and Ruchika. It is my pleasant duty to recall with gratitude the everlasting affection, encouragement and all support I have been receiving from my family members. I also take this opportunity to thank my parents (Ma and Baba) for life lessons and unparalleled affection and love.

I also dedicate this thesis to my lovely sisters Papia and Dalia for being in my life and making it the most beautiful one. I gathered courage from the wishes to meet my lovely and cute niece, Mistu.

Last but not least, I thank all the persons who have, directly or indirectly, helped me during my Ph.D. Thesis. And above all I thank God.

Abstract

The atmosphere of Mars is mostly CO_2 and other species such as O_3, O, HO, HO_2, H_2O and CO are found in trace amounts but are important in the photochemistry and stability of the CO_2 dominated atmosphere. The orbital properties of Mars and variations in exposure to solar influx lead to seasonal and latitudinal variations of the short lived trace gases, which is not well studied in the literature. Systematic global observations have recently become available for O_3, but are lacking for the other species. We study the spatio-temporal variability of these species based on available observations, and a photochemistry coupled global general circulation model (GCM) for Mars. The GCM simulated seasonal distribution of temperature, N_2, Ar, CO, H_2O, O_3 agree well with inferences from observations wherever available. We retrieve two years (MY 27 and MY 28) of total columnar O_3 from raw spectral data provided by the SPICAM instrument onboard the Mars Express, using a forward radiative transfer model. The seasonal variability is studied in tropical, mid and high latitudes and is compared with the GCM simulations. The high latitudes exhibit the largest seasonal variations in O_3, with a winter high and a summer low and comparison with GCM results is good in general. We have studied the correlation of ozone with dust, retrieved simultaneously from SPICAM observations. In southern tropical latitudes, the columnar ozone is seen to increase during a global dust storm year (MY 28) compared to the ozone column values during a year without global dust storm (MY 27), though the water vapour column between these years remains unchanged. This indicates towards the radiative impact of dust on ozone and its retrieval. We also study the effect of transport on columnar amount of ozone through ozone-carbon monoxide correlation as CO is considered a tracer of dynamics. The dynamical contribution to the ozone column is found to be significant during winter over the southern polar region. In this thesis, we have also studied in detail, the important source and sink processes of odd oxygen (O_3 and O) and their contributions in different locations and seasons. The odd oxygen species are short lived and hence generally taken

in photochemical equilibrium in model calculations. However our study shows that these species do not always remain in photochemical equilibrium. The equilibrium exists only below 30 km, which may extend to 45 km depending on the hygropause level. Thus we have used the effect of water vapour on the loss rates of odd oxygen ($O+O_3$) to classify different photochemical regimes.

Along with these neutral species, Martian lower atmosphere also contains positive and negative ions. Earlier studies using the PRL ion-dust model have shown that the lower ionosphere of Mars is dominated by hydrated ions such as $H_3O^+(H_2O)_2$ and $H_3O^+(H_2O)_3$, $CO_3^-H_2O$, $CO_3^-(H_2O)_2$, and $NO_2^-H_2O$. Dust in the Martian ionosphere acts as a loss agent for the positive and negative ions, while the trace neutral species discussed above are sources for these ions through ion-neutral chemistry. We have investigated the structure of the lower ionosphere of Mars for seasons Ls = 0° – 90°, Ls = 90° – 180°, Ls = 180° – 270° and Ls = 270° – 360° over the equatorial, mid-latitude and polar regions for MY 27. The study shows that over polar region the D-layer can disappear due to lack in water vapour even in minimum dust loading scenarios. Thus the ion densities of the major positive and negative ions are strongly dependent on the available water vapour. In the mid and low latitude regions, the ion densities depend on the competing effect of the dust and water vapour.

Keywords: Martian lower atmosphere, atmospheric trace gases, Martian lower ionosphere, Mars GCM, SPICAM, ozone, water vapour, dust in Martian atmosphere, Seasonal variability of ions, hygropause,.

Contents

Introduction **1**

1.1 Neutral composition of the Martian atmosphere 6

1.1.1 Martian Photochemistry 9

1.1.2 Martian dust 11

1.2 Ions in the Martian ionosphere 12

1.3 Objectives 15

Methodology **17**

2.1 Ozone and dust retrieval 17

2.1.1 Raw Data and retrieval method 19

2.1.2 Forward model 20

2.1.3 Model atmosphere 22

2.1.4 Rayleigh scattering 22

2.1.5 Dust scattering 23

2.1.6 Fitting method 25

2.2 General Circulation Model (GCM) for Mars 27

2.2.1 Dust scenarios in the model 27

2.2.2 Water cycle and clouds 28

2.2.3 Radiative transfer 28

2.2.4 CO_2 seasonal cycle 29

2.2.5 Photochemistry 30

2.3 Ion model 32

2.3.1 Ion chemistry of the lower atmosphere 33

Thermal structure and composition of the Martian atmosphere **36**

3.1 Observations of temperature 36

3.2 Temperature structure based on GCM 39

3.3 Composition overview based on observation 40

3.4 Atmospheric composition simulated by GCM 45

3.4.1 Nitrogen and Argon 45
3.4.2 Carbon Monoxide 47
3.4.3 Water Vapour 49
3.4.4 Ozone 50
3.5 Conclusion 51
Spatio-temporal variability of odd oxygen 53
4.1 Competing pathways in odd oxygen photochemsitry 54
4.1.1 Seasonal variation in production and loss rates of odd oxygen 57
4.1.2 Comparison among the production and loss rates 64
4.1.3 Comparison with one dimensional models 68
4.2 Ozone and dust from observations and comparison with model 70
4.2.1 Comparison of observed ozone with GCM simulations 71
4.2.2 Dust optical depths retrieved from SPICAM 73
4.2.3 Ozone and dust 74
4.2.4 CO-O_3 correlation 77
4.3 Conclusion 80
Martian Lower Ionosphere 86
5.1 Introduction 86
5.2 Objective 90
5.3 Ion-dust model 91
5.4 Input parameters 92
5.5 Results and discussions 96
5.5.1 Positive ions 96
5.5.2 Negative ions 101
5.6 Summary and Conclusion 106
Summary and Scope for future work 108
6.1 Summary 108
6.2 Major results of the study 109
6.2.1 Temperature and neutral species simulated by GCM 109

6.2.2 Spatio-temporal variability of odd oxygen species 110
6.2.3 Martian lower ionosphere 111
6.3 Scope for future work 112
References 114

List of Figures

1.1: A schematic of the seasons on Mars…….....3

1.2: Seasonal variation of surface pressure from Viking landers…….4

1.3: A globally and seasonally averaged temperature profile of Mars from MCD……5

2.1: A typical raw spectra recorded in nadir geometry by SPICAM……....18

2.2 Phase function comparison…….24

2.3: Scattering and extinction efficiencies……....25

2.4: An example of a fitted spectrum…….26

2.5: Chemical scheme for ion chemistry……...34

2.6: Positive and negative ion densities……35

3.1: Zonal mean average of temperature…….……..38

3.2: Global distribution of Ar from LMD-GCM……..46

3.3: Global distribution of N_2 from LMD-GCM……..47

3.4: Global distribution of CO from LMD-GCM…….48

3.5: Global distribution of H_2O from LMD-GCM……49

3.6: Global distribution of O_3 from LMD-GCM……...51

4.1. Vertical profiles of net O_x production, water vapour mixing ratios, and water vapour saturation values……...56

4.2: Vertical number density profiles of O, O_3, HO_2, OH, and H…….58

4.3: Seasonal variation of the daytime loss rates of O_x over 60ºN–90ºN……...59

4.4: Seasonal variation of the nighttime loss rates of O_x, over 60ºN–90ºN……..60

4.5: Seasonal variation of the daytime loss rates of O_x over 60ºS–90ºS……61

4.6: Seasonal variation of the daytime loss rates of Ox over 60ºS–90ºS……..62

4.7: Seasonal variation of the daytime loss rates of Ox over 20ºS–40ºS……63

4.8: Seasonal variation of the nighttime loss rates of Ox over 20ºS–40ºS…….64

4.9: Comparison among the loss rates of O_x…….69

4.10: Global Ozone-column distribution, retrieved from SPICAM for MY 27……....71

4.11: Comparison of Ozone values from SPICAM and LMD-GCM……....72

4.12: Dust optical depth retrieved from SPICAM……....73

4.13: Correlation of ozone and dust……..75

4.14: Seasonal variation of water vapour columnar over 30ºS-0º and 0º-30ºN……..……76

4.15: Comparison of ozone from SPICAM and GCM simulated values for MY 28 over the latitude regions 30ºS-0º and 0º-30ºN……...77

4.16: Correlation between O_3 and CO from the LMD-GCM…….79

4.17: Ozone vertical profiles simulated for 3D and 1D version of LMD-GCM……80

5.1: Electron density profile retrieved from radio occultation science experiment (ROSE) on board MAVEN …… ……...87

5.2: Model structure of Martian ionosphere…….89

5.3: Temperature profiles for the ion-dust model…….92

5.4: Water vapour profiles for the ion-dust model…….94

5.5 Dust number density profiles for the ion-dust model……..95

5.6: Seasonal variation of ion H_3O^+ ….……..…...97

5.7: Seasonal variation of ion $H_3O^+H_2O$……98

5.8: Seasonal variation of ion $H_3O^+(H_2O)_2$……99

5.9: Seasonal variation of ion $H_3O^+(H_2O)_3$……..100

5.10: Seasonal variation of ion CO_4^-……102

5.11: Seasonal variation of ion $CO_3^-H_2O$……....103

5.12: Seasonal variation of ion $CO_3^-(H_2O)_2$……....104

5.13 Seasonal variation of ion $NO_2^-H_2O$……105

List of Tables

1.1: Comparison of orbital parameters of Earth and Mars……2

3.1: Recent mixing ration of Martian atmospheric composition……45

4.1: Column integrated production and loss rates of O_x……82

4.2: Percentage contribution (in %) of each loss process of O_x……84

List of Abbreviations

AU: Astronomical Unit.

CRISM: Compact Reconnaissance Imaging Spectrometer for Mars.

ESA: European Space Agency.

GCM: General Circulation Model.

GCR: Galactic Cosmic Rays.

GFDL-GCM: Geophysical Fluid Dynamic Laboratory GCM.

IRTF: Infrared Telescope Facility.

LMD: Laboratoire de Météorologie Dynamique.

MARCI: the MARs Colour Imager.

MaRS: Mars express orbiter Radio Science experiment.

MARSIS: Mars Advanced Radar for Subsurface and Ionosphere Sounding.

MAWD: Mars Atmospheric Water Detection.

MCD: Mars Climate Database.

MEX: Mars Express.

MGS: Mars Global Surveyor.

MRO: Mars Reconnaissance Orbiter.

MTGCM: Mars Thermospheric GCM.

MAVEN: Mars Atmosphere and Volatile EvolutioN.

NASA: National Aeronautics and Space Administration.

PFS: Planetary Fourier Spectrometer.

PRL: Physical Research Laboratory.

ROSE: Radio Occultation Science Experiment.

RPA: Retarding Potential Analyzer.

SPICAM: SPectroscopy for the Investigation of the Characteristics of the Atmosphere of Mars.

TES: Thermal Emission Spectra.

THEMIS: THermal EMission Imaging System.

Chapter 1

Introduction

Mars is one of the inner terrestrial planets of our solar system which revolves around the Sun in an elliptical orbit of eccentricity with 0.093, and is also referred to as red planet because of its appearance. Mars being ten times lighter than Earth, possesses almost three times smaller gravitational pull. The radius of the planet is half the radius of Earth. The average distance between Sun and Mars is 1.48 AU. The rotational axis inclination is about 25.2^o, similar to that of Earth. Therefore just as on Earth, there are seasons on Mars as well. A complete full rotation of Mars along its own axis takes 24 hour 39 minutes and 35 seconds, which is a little longer than the Earth's diurnal period (86400 seconds). Martian days are termed as Sols. One Martian year is 668.6 sols (~ 687 Earth day), almost twice as long as that of Earth's. A particular seasons on Mars is represented by the angle between Sun and Mars with respect to the northern hemispheric spring equinox. This angle is called Solar Longitude (Ls) or Aerocentric Longitude. Thus at northern hemispheric spring equinox, Ls = 0° (see Figure 1.1), Ls = 90° corresponds to northern summer solstice, Ls = 180° corresponds to northern autumn equinox and Ls = 270° corresponds to northern winter solstice. Due to the high elliptic orbit of Mars (eccentricity=0.093), the length of the four seasons is not uniform; Ls = 0° – 90° (259.8 sols); Ls = 90° – 180° (210.7 sols); Ls = 180° – 270° (210.7 sols); Ls = 270° – 360° (210.7 sols).The Martian perihelion occurs at Ls = 251° during the southern summer and aphelion occurs as Ls = 71° during northern summer. During perihelion the Sun-Mars distance is 1.38 AU and during aphelion the

distance increases to 1.67 AU. A comparison of the orbital parameters between Earth and Mars is given in Table 1.

Properties	Mars	Earth
Mass (Kg)	6.46×10^{23}	5.98×10^{24}
Radius (km)	3394	6369
Gravity at surface (ms^{-2})	3.72	9.81
Average distance from Sun (AU)	1.52	1
Length of year (Earth days)	687	365
Length of solar day (hours)	24.66	24
Spin-axis inclination (degree)	25.2	23.5
Surface pressure (mb)	6	1013
Orbital eccentricity	0.017	0.093
Atmospheric Constituents	CO_2 (95.7 %)	CO_2 (0.03 %)
	O_2 (0.173 %)	O_2 (20.9 %)
	H_2O (0 – 200 ppm)	H_2O (~2 %)
	CO (749 ppm)	CO (0.2 ppm)
	Ar (2.03 %)	Ar (1.6 %)
	Kr(0.3 ppm)	Kr(1.1 ppm)
	Xe (0.08 ppm)	Xe (0.09 ppm)
	Ne (2.5 ppm)	Ne (18 ppm)

Table 1: Comparison of the orbital parameters of Mars with those of Earth.

Thus we see that Mars and Earth are similar in many aspects, for example the diurnal period and spin-axis inclination. Early Mars (more than 3.8 billion years ago) was warm and wet (Ehlmann et al., 2008). According to one dimensional studies performed by Forget and Pierrehumbert, (1997), average surface temperature was 40 ^{o}K higher and surface pressure could have been a few hundred to thousands of millibar which produced completely different climatic conditions than the current frigid dry desert state. Due to lack of intrinsic magnetic field, solar wind consisting of energetic particles enters the dense part of the Martian atmosphere and ionizes the atmospheric constituents, which then follow the tail of solar magnetic field (Lundin, 1990; Chassefiere and Leblanc, 2004). Thus solar wind wiped out directly the dense atmosphere of Mars. Lower gravitational pull and photochemistry of Mars also contributed to the escape. Long lived molecular hydrogen (H_2) produced from photolysis of water vapour was transported into the

thermosphere and exosphere, where it got converted into atomic hydrogen (H) and escaped the atmosphere (Lammer et al., 2003; Chaffin et al., 2016). Similarly other species also escaped from the atmosphere of the planet. The escape processes thus left a thin

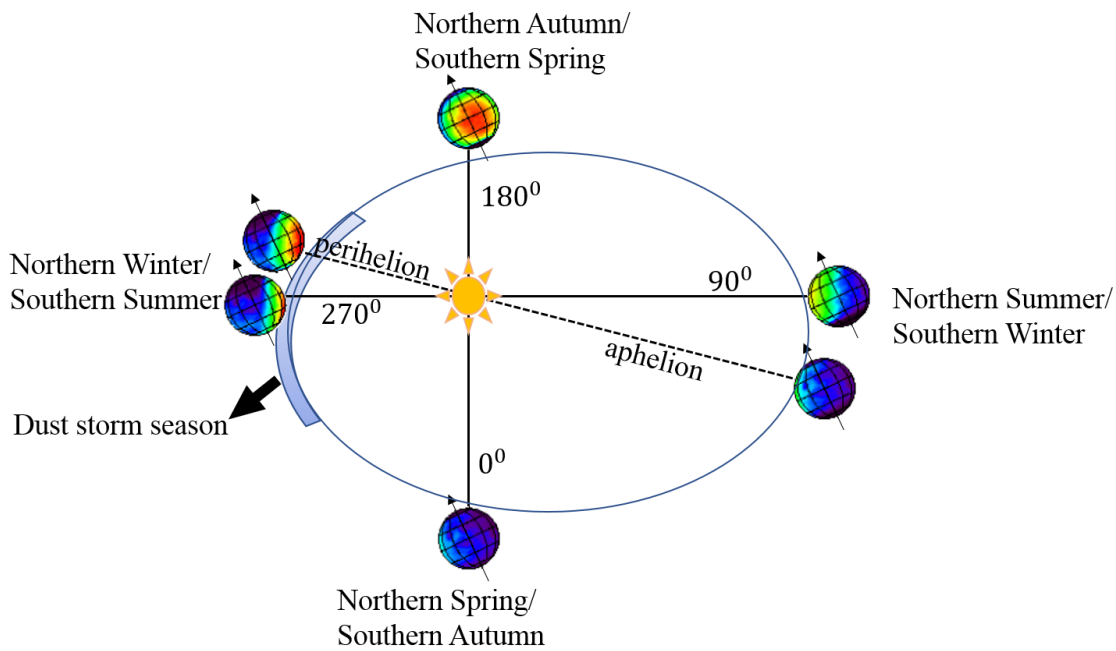

Figure 1.1: A schematic of the seasons on Mars.

atmosphere which currently surrounds Mars and extends from ground to nearly 500 km. The average surface pressure of the recent Martian atmosphere is 6mb which is almost 150 times smaller than that on Earth (Schofield et al., 1997). The atmospheric pressure decreases with altitude following the hydrostatic law (Seiff and Kirk, 1977). According to the in-situ measurements by Viking Lander 1 and 2, the surface pressure undergoes a seasonal cycle (Hess et al., 1977). This phenomenon occurs due to condensation of atmospheric CO_2 onto the polar caps. During Ls = 90° – 180°, a significant percentage (~ 30%) of the atmosphere condenses over the polar caps (mainly southern polar cap) signature of which is identified in the in-situ measurement of Viking landers.

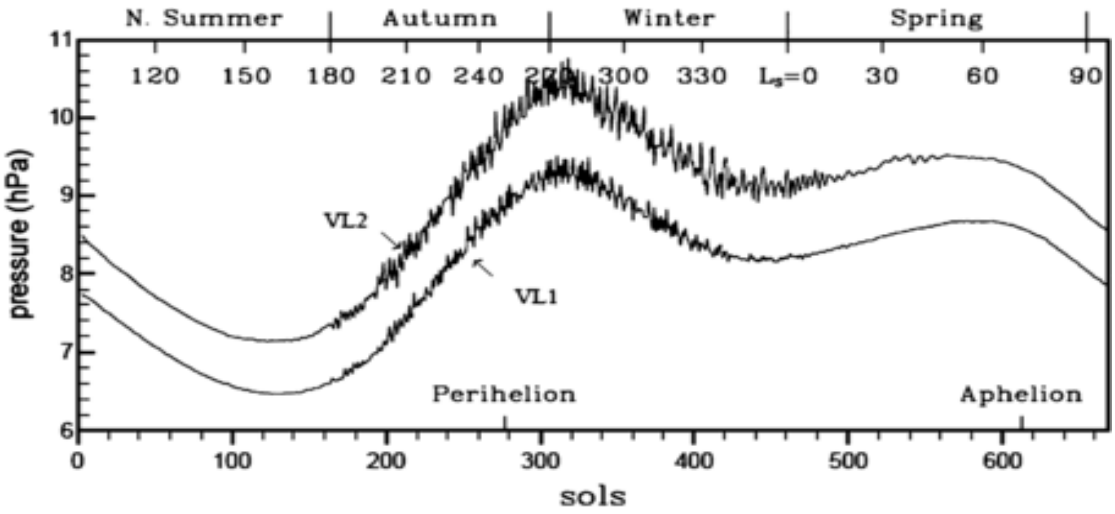

Figure 1.2: Seasonal variation of surface pressure at the location of Viking Lander 1 and Viking Lander 2. Image credit: Haider and Mahajan, (2014).

Based on an average (global and seasonal average) temperature profile, the Martian atmosphere can be divided into four layers: the troposphere, mesosphere, thermosphere and exosphere. A global average profile of temperature is shown in Figure 1.3. The profile has been derived from Martian Climate Database (MCD) (Millour, 2015). The temperature values plotted in Figure 1.3 are corresponding to the noon of the sols. The shaded region is implying the seasonal extent of the temperature profile. Depending on the season, time of the sol and latitude, it varies from a minimum of about 130 ^{o}K over the northern polar region during northern winter to 300 ^{o}K over southern tropical region during the perihelion season (McCleese et al., 2010). Temperature decreases with altitude in the troposphere with almost constant lapse rate (-dT/dh) as can be seen from the Figure 1.3. The lapse rate which implies decrease of temperature with altitude becomes smaller above 40 km. Due to the absence of ozone or any other heating agent, the Martian atmosphere does not have a stratosphere as in the Earth's atmosphere. Instead, it has a mesosphere which starts above 40 km with smaller lapse rate. Mesosphere extends from 40 to 100 km. The lower mesosphere is roughly isothermal while in the upper part of the mesosphere (80 – 100 km) the temperature shows increased lapse rate. Above mesosphere

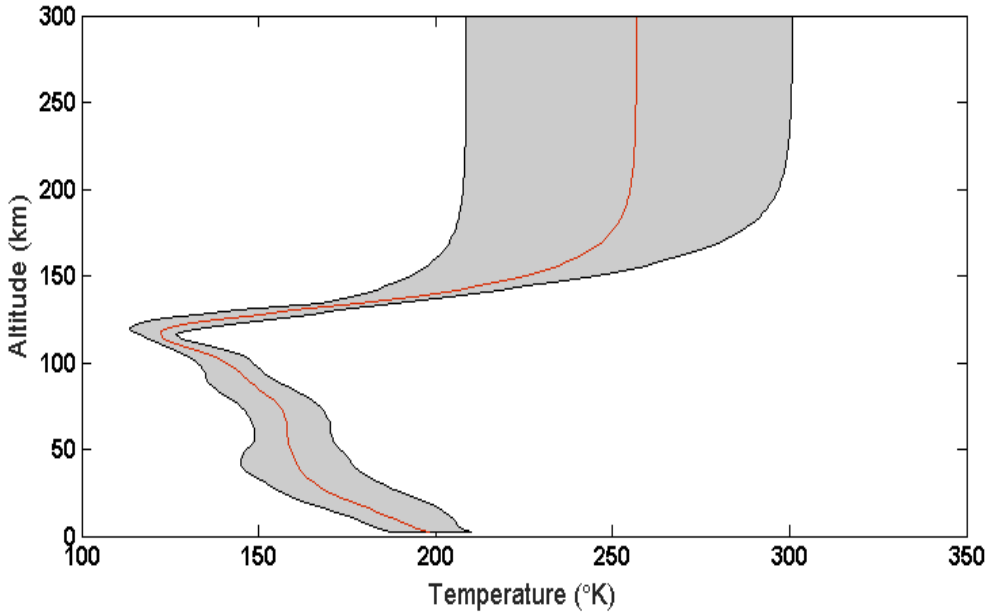

Figure 1.3: A globally and seasonally averaged temperature profile of Mars derived from Mars Climate Database. The shaded region is the seasonal spread of the global averaged temperature.

EUV (Extreme Ultra Violet) heating temperature rises and the increase continues up to 200 km. This region is called thermosphere. The EUV absorption in the Martian thermosphere is weaker than the Earth's thermosphere due to low density and lower solar influx. Above 200 km the atmospheric density becomes almost negligible and the variation in temperature becomes insignificant. Exosphere extends above this height in the atmosphere and from this region atmospheric gases can escape depending on its energy and direction of motion.

Martian atmosphere is mostly composed of CO_2 (95.7%) while N_2 (2.07%) and Ar (2.03%) are the other major species (Franz et al., 2015). The remaining 0.2% of the Martian atmosphere comprises of CO, O_2, H_2, H_2O, Ne, Kr, Xe, and O_3. In the remaining part of this chapter, we briefly describe the neutrals and ions that contribute to the Martian atmosphere.

1.1 Neutral composition of the Martian atmosphere

Martian atmosphere has been explored by many spacecrafts and Earth based instruments. First glimpse to the Martian atmospheric composition was given by G.P Kuiper when he detected the strong absorptions of CO_2 around 1.6 µm and 2.0 µm in the spectra from the Martian atmosphere. Spinrad, Mǔnch, and Kaplan detected presence of water vapour in the Martian atmosphere in 1963. Oxygen line in the spectra from Mars was first detected in 1968 by Belton and Hunten (1968) using the McMath telescope. However, the presence of O_2 was finally confirmed by Barker (1972). In the next few years carbon monoxide (CO), atomic oxygen (O) and atomic hydrogen (H) were discovered by Kaplan et al. (1969), Barth et al. (1969), and Barth et al. (1971) respectively. The First in-situ measurement in the Martian atmosphere was made by the mass spectrometers on the Viking landers (1 & 2). Both the landers determined a few neutral constituents and discovered pressure cycle (Hess et al., 1980) at their landing sites. Since then, several orbiters, landers and rovers have provided valuable observations that have improved our understanding the Martian atmosphere. For example, the Thermal Emission Spectrometer (TES) onboard the Mars Global Surveyor (MGS) spacecraft launched by NASA, has observed the Martian atmosphere at different latitudes and longitudes from the middle of the Martian Year (MY) 23 to MY 28. For the purpose of timekeeping and also to indicate the beginning of systematic studies by the scientific community, the counting of Martian Year was first used by Clancy et al., 2000 where they defined MY 1 to begin at April 11, 1955 when Mars was at Ls = 0°. These observations include extensive measurements of temperature profiles (Smith et al., 2001; Bernie et al., 2000; Hinson et al., 2004) and neutrals (Christensen et al., 2000). TES observations are also extensively used for the understanding of dust storms (Smith et al., 2009) and water cycle (Smith et al., 2002). Among the other missions to Mars, the MARs Colour Imager (MARCI) onboard the Mars Reconnaissance Orbiter (MRO) spacecraft (Clancy et al., 2016) and the SPectroscopy for the Investigation of the Characteristics of the Atmosphere of Mars

(SPICAM) onboard the Mars Express (MEX) (Montmessin et al., 2017), have produced almost five years of observation which helped study the behavior of ozone and dust. Both these spacecrafts were launched by the European Space Agency (ESA). Water vapour is studied from the SPICAM IR observations. The observations from Compact Reconnaissance Imaging Spectrometer for Mars (CRISM) (Murchie et al., 2007) onboard MRO are used to study CO and water vapour (Smith et al., 2009). From the most recent in-situ mass spectrometric measurement made by the Curiosity rover of NASA, the mixing ratios of the constituents such as CO_2, N_2, Ar and O_2 were determined. The mixing ratio is a ratio of the density of any constituent divided by the total density of air. These are found to be 0.957, 0.0207, 0.0203 and 0.017×10^{-3} for CO_2, N_2, Ar and O_2 respectively. From the measurements discussed above, CO mixing ratio is known to be 700 ppm (Smith et al., 2009), whereas H_2O and O_3 are variable. Water vapour (H_2O) varies from 10 – 200 ppm (McConnochie et al., 2018) and O_3 varies from 0.02 – 2.0 ppm.

Apart from the species discussed above, there are indications that methane (CH_4) exists on Mars. Methane was first detected by the Planetary Fourier Spectrometer (PFS) on Mars Express (Formisano et al., 2004). Methane is observed to show seasonal variation over a background amount of 0.7 ppbv (Webster et al., 2015). The formation of methane cannot be explained with the existing photochemical models (Lefevre and Forget, 2009). Sulfur dioxide (SO_2) is believed to exist in trace amounts (~ 2 ppbv), the first detection of which was made by Encrenaz (2011) based on observations from the Texas Echelon Cross Echelle Spectrograph (TEXES). The Martian atmosphere also contains Nitrogen species, mainly the NO_x chemical family ($NO+NO_2$). The number density of NO and NO_2 at surface is ~ 10^8 cm^{-3} and ~ 10^7 cm^{-3} respectively (Millour et al., 2015). Water vapour (H_2O) (Number density at surface varies from ~ 10^{11} cm^{-3} to ~ 10^{14} cm^{-3} between summer and winter) and its derivatives such as HO_x ($HO+HO_2$) (10^5 cm^{-3} to 10^7 cm^{-3}) radicals are one of the most important components of the Martian atmosphere. There are no observations for many species such as NO_x, HO_x. The number density for these species given above is predicted by theoretical photochemical models. The theoretical models for Martian atmosphere started developing in early seventies (Parkinson and Hunten, 1972;

McElroy and Dunnahue, 1972). Their work mostly addressed the major question regarding the stability of the CO_2 atmosphere. The question was partly solved by the inclusion of water vapour in the photochemical models. The photochemical models such as by Liu and Dunahue (1976), Kong and McElroy (1977), Izakov and Krasitskii (1977) and Krasnopolsky and Parshev (1979) were developed for mean atmospheric conditions and included more complex chemistry. Other one dimensional models (Nair et al., 1994 and Atreya and Gu, 1995) discuss the possible effect of heterogeneous chemistry on the Martian photochemical cycle. There have been attempts to study the seasonal and diurnal variation in photochemistry (Shimazaki and Simizu, 1979, Shimazaki, 1981 and Rodrigo et al., 1990). These one dimensional models are unable to account for the three dimensional transport by wind and therefore they were inadequate for the seasonal and spatial studies of the atmosphere. Consequently, three dimensional models were developed for the Martian atmosphere. A general circulation model (GCM) for Mars has been developed at the LMD (Laboratoire de Météorologie Dynamique), France (Hourdin et al., 1993) which simulates atmospheric circulation. Few other GCMs besides LMD-GCM that model the Martian atmosphere are Mars GCM (MGCM) (Lewis, 2003), Mars Thermospheric GCM (MTGCM) and Geophysical Fluid Dynamic Laboratory (GFDL)-GCM (Richardson and Wilson, 2002). Numerical simulation of LMD-GCM have been used earlier to explain the surface pressure results of Viking observation. A seasonal cycle of pressure variation (see Fig 1.2) was recognized from the Viking lander's surface pressure measurements (Hess et al., 1979). This pressure cycle helped in explaining condensation and sublimation of CO_2 on polar regions which was put forward by the thermal model of Leighton and Murray, (1966). Based on numerical studies, Hourdin et al. (1993) attributed the pressure cycle variation to two other factors namely, orography and the effect of dynamics other than condensation and sublimation. A photochemical model was coupled to the LMD-GCM (Lefevre et al., 2004), the simulation of which agreed reasonably with observations such as water vapour and ozone. Later inclusion of heterogeneous chemistry in the photochemical module improved the agreement (Lefevre et al., 2008).

1.1.1 Martian Photochemistry

In the present atmosphere of Mars, the most dominant gas CO_2 shows significant seasonal variation through the condensation and sublimation onto the polar caps and the regolith. A significant percentage of the atmosphere (~ 30 %) condensates and sublimates onto the polar caps which leads to the seasonal pressure cycle in the atmosphere (Forget and Pierehert 1997). The condensation of CO_2 within the atmosphere also occurs in the form of CO_2 ice and CO_2 snow. CO_2 mostly sediments in the form of CO_2 ice. In order to address the problem of stability of the Martian atmosphere, the models attempted to explain the recovery of CO_2, after it is photodissociated by the reaction below

$$\mathrm{CO_2} + \mathrm{h\nu} \rightarrow \mathrm{CO} + \mathrm{O}, \quad (\lambda < 200 \text{ nm}) \tag{1.1}$$

Though the reverse reaction $\mathrm{CO} + \mathrm{O} + \mathrm{M} \rightarrow \mathrm{CO_2} + \mathrm{M}$ is rotationally forbidden, the Martian atmosphere is believed to sustain 95.7% of CO_2 due to the water vapour in the atmosphere. Water vapour produces catalytic radicals H and OH as a result of photodissociation with photons of wavelength less than 240 nm, as per the reaction below.

$$\mathrm{H_2O} + \mathrm{h\nu} \rightarrow \mathrm{H} + \mathrm{OH}, \lambda < 240 \text{ nm}. \tag{1.2}$$

The catalytic radicals regulate the lost CO_2 by converting CO into CO_2 through the following reaction.

$$\mathrm{CO} + \mathrm{OH} \rightarrow \mathrm{CO_2} + \mathrm{H} \tag{1.3}$$

Argon, the most dominant noble gas in the Martian atmosphere (2.07%) does not take part in chemical reactions. However, it does show seasonal variation at a particular location on Mars due to transport (Sprague et al., 2007). Molecular nitrogen is the other species comparable to Argon in terms of percentage contribution. The initiation of the nitrogen chemistry happens in the upper atmosphere at altitudes greater than 100 km. In the upper atmosphere, molecular nitrogen gets dissociated with energetic electrons (> 9.76 ev) and produces odd nitrogen (N). Odd nitrogen in metastable state ($N(^2D)$) produces nitric oxide (NO) as a result of quenching with CO_2 (Nier and McElroy, 1977). NO is the

most abundant odd nitrogen species in the Martian atmosphere. The consequent reactions of NO with O, O_3, OH and HO_2 produce other nitrogen compounds such as HNO_2, HNO_3, NO_2 and N_2O.

Among, the other tracer species (mixing ratio < ~ 1%) water vapour exhibits the most important role in the Martian photochemistry. It produces the HO_x radicals which stabilizes the atmosphere. The seasonal cycle of water vapour has a significant impact over the amount of tracers such as O_3 and O, the study of which is one of the objectives of the thesis. Apart from contributing to the atmospheric stability as discussed above, the HO_x radicals play a key role in odd oxygen chemistry, which has been studied in detail in this work. Source of the water vapour in the Martian atmosphere are the water trapped beneath the southern and northern polar caps (Fedorova et al., 2006). Martian regolith can also trap water when the temperature is low enough (Bottger et al., 2005). The northern polar cap is the greatest source of water vapour. THEMIS (Thermal Emission Imaging System) measurement (Smith, 2002) shows that water column amount can reach as high as 100 pr-µm over the northern polar region during summer when the polar cap releases water vapour. 1 pr-µm (precipitable-micron) of H_2O column is defined as the total amount water vapour in a unit cross-sectional area column if condensed as liquid water can produce a micrometer thick layer of liquid water (3.34×10^{18} molecules cm^{-2}). Compared to the northern polar region the seasonal maximum in water column is almost half (50 pr-µm) over the southern polar region, while during winter water vapour is almost absent in the polar region.

Ozone is a trace gas that has been extensively studied in the Earth's atmosphere in terms of its photochemistry and radiative properties. Ozone is also formed in the Martian atmosphere following the Chapman mechanism similar to that on Earth.

$$CO_2 + h\nu \rightarrow CO + O, (\lambda < 200 \text{ nm}) \quad (1.4)$$

$$O + O_2 + M \rightarrow O_3 + M \quad (1.5)$$

The abundance of ozone in the Martian atmosphere, however, is about 100 times less than that in the Earth's atmosphere. Since the observations from Mariner 9, ozone is used widely for the validation of the photochemical models. Ozone has a strong correlation with water vapour which will be discussed in Chapter 4, and thus can be used as proxy of HO_x radicals which are derivative of H_2O. The amount of ozone is also used to determine the habitability of the Martian atmosphere since it absorbs solar UV rays.

1.1.2 Martian dust

Dust is an important component of the Martian atmosphere. Dust heating through absorption of radiation, has a strong impact on the thermal and dynamical state of the atmosphere. The atmospheric variability is also influenced by the dust cycle. Dust was detected in the Martian atmosphere as early as Mariner 9 (Anderson and Leovy, 1978) and also in the in-situ observations by Viking landers (Pollack et al., 1979). These dust particles are lifted by various processes such as surface wind stress, near surface saltation and dust devils (Newman et al., 2002). Dust particles can float in the atmosphere for a long time as the gravitational pull of Mars is low. In the Martian atmosphere, dust storms are a common phenomenon. Every year during perihelion season (Ls = 240° – 360°), regional dust storm occurs which increases the opacity of the atmosphere up to 0.3 – 0.5 (9µm optical depth) (Smith 2009, Sheel and Haider, 2016). Most of these regional dust storms originate in the southern tropical regions (Kass et al., 2016). In some years these local dust storms grow into a global or planet encircling dust storm. One such global dust storm occurred during MY 25 and another one in MY 28, which is captured in the observation of THEMIS and TES (Sheel and Haider, 2016).

Dust being radiatively active in the Marian atmosphere, it absorbs infrared radiation emitted by the planet (Gierasch and Goody, 1972) and also it interacts with UV (Perrier et al., 2006) and in the visible region weakly. The atmospheric dust plays a role in the ion and neutral chemistry of the atmosphere. Dust has been found to be a sink for the HO_x radicals in the Martian atmosphere (Lefevre and Monmessin, 2008). Other trace elements such as NOx, H_2O_2 also take part in heterogeneous chemistry inflicted by dust. Dust acts

as a sink for ions in the ionosphere of Mars. Both the positive and negative ions are destroyed during dust storms due to attachment to dust particles (Sheel and Haider, 2016).

1.2 Ions in the Martian ionosphere

As a result of the ionization of neutral species in Martian atmosphere caused by solar radiation and particle impact, the atmosphere contains positive and negative ions and electrons at all altitudes which forms the ionosphere. Thus the ionosphere of Mars extends upto the surface, unlike the Earth's ionosphere (Withers, 2009; Haider et al., 2009). First in-situ measurement of the upper ionosphere was made the Viking retarding potential analyzers (RPA) which determined the ionospheric peak density (Hanson et al., 1977). Other observations of the ionosphere are available from missions such as MGS (Bougher et al., 2004), Mars Odyssey (Krymskii et al., 2003), MEX (Bertaux et al., 2006) and MAVEN (Withers, 2018) (Mars Atmosphere and Volatile EvolutioN) accelerometers of MGS and MRO (Bougher et al., 2007), and MARSIS (Mars Advanced Radar for Subsurface and Ionosphere Sounding) (Gurnett et al., 2005). Radio occultation experiments on Mars Express (Patzold et al., 2005) and that on MGS (Withers, 2006) acquired a large number of dataset of Martian upper (> 100 km) ionosphere. These observations have proved useful in studying the variation in the electron densities due to solar events (Jakosky et al., 2017) or magnetic field (Mendillo et al., 2018).

Depending on the sources of ionization Martian ionosphere can be divided into two regions - the upper and lower ionosphere. The upper ionosphere is ionized by solar EUV and X rays while the lower ionosphere is mainly created due to impact ionization of galactic cosmic rays (GCR). The Martian upper ionosphere contains the E and F layer peak while the lower ionosphere contains the D region. The peak in electron density for the E region (10^5 cm^{-3} for Earth and ~$2x10^4$ cm^{-3} for Mars) (Schunk and Nagy, 2009) are produced in the altitude region 90 – 120 km for both Earth and Mars (Kelly, 1989; Brasseur and Solomon, 2005; Bougher et al., 2001; Fox, 2004, Haider et al., 2009, 2016). The Martian lower atmosphere is similar to the D layer of Earth in terms of comparable negative ion concentration. However, the peak occurs at altitudes between 60 and 75 km

for Earth (Richmond, 1987; Kelly, 1989), whereas on Mars it is much lower. Martian Upper and lower ionosphere greatly differs in composition. In the upper atmosphere electron density is the dominant component of the negatively charged species, while the dominant positive ions are O_2^+, NO^+ and CO_2^+ (Haider et al., 2009). On the other hand, in the lower ionosphere negative ions such as $CO_3^-(H_2O)_2$, $CO_3^-(H_2O)_2$ and $NO_2^-H_2O$ and positive hydrated ions such as H_3O^+, $H_3O^+H_2O$, $H_3O^+(H_2O)_2$ are dominant with low electron density (Sheel and Haider, 2016).

The common ionization process in the upper ionosphere of Mars is the photoionization of CO_2 by the solar extreme ultraviolet and X-ray radiation ($\lambda < 100$ nm).

$$\mathrm{CO_2 + h\nu \rightarrow CO_2^+ + e} \tag{1.6}$$

CO_2^+ ion is almost immediately removed by O leading to $\mathrm{O_2^+}$ (Nagy et al., 2004). $\mathrm{O_2^+}$ ions are destroyed in the dissociative recombination and produce energetic O molecules. This process mainly occurs in the upper atmosphere above 100 km because solar EUV cannot penetrate any deeper in the atmosphere. The reaction of charge removal ($\mathrm{CO_2^+ + O \rightarrow O_2^+ + CO}$) is very fast compared to the other processes which make O_2^+ the most dominant ion (between 130 and 240 km) in the upper atmosphere (Withers, 2009). Other major ions are CO_2^+, O^+ and NO^+.

The Other notable process of the upper ionosphere is the production of N atoms and NO^+ ions. In the Martian atmosphere N atoms are produced by the dissociative recombination of N_2^+ and electrons or by the collisions of N_2 molecules with energetic electrons. The collision generates energetic nitrogen atom $N(^2D)$.

$$\mathrm{N_2^+ + e \rightarrow N + N} \tag{1.7}$$

$$\mathrm{N_2 + e \rightarrow N(4S) + N(2D) + e} \tag{1.8}$$

The $N(^2D)$ reacts with CO_2 and produce nitric oxide.

$$N(2D) + CO_2 \rightarrow NO + CO \tag{1.9}$$

NO^+ is produced following the below reactions

$$N_2^+ + O \rightarrow NO^+ + N \tag{1.10}$$

$$O_2^+ + NO \rightarrow NO^+ + O_2 \tag{1.11}$$

This thesis is mainly concentrated in the study of the lower atmosphere, i.e. below 100 km, where the observations are rare. First theoretical study of the lower ionosphere was made by Whitten et al. (1971) with a few neutrals and after almost three decades, Molina-Cuberos et al. (2002) developed an ion-neutral model which consisted of more than 100 reactions and included new neutral and nitrogen derivate ionic species. Comparatively, recent studies by Sheel and Haider (2012 and 2016) showed the effect of galactic cosmic rays and atmospheric dust storms on the production and densities of 35 positive and negative ions including more than 100 reactions. These studies were based on one dimensional photochemical equilibrium models. As discussed above, the atmospheric components such as dust, water vapour, and ozone show seasonal variations which are important parameters in determining the ion concentrations of the lower atmosphere. Therefore, the present lower ionosphere is expected to vary seasonally which is one of the objectives of the thesis work. The major source of ionization in the lower atmosphere are galactic cosmic rays (GCR), since ionizing solar UV radiation cannot penetrate below 100 km. The neutrals of the lower ionosphere get ionized and initially produce positive ions such as CO_2^+, Ar^+, N_2^+, O_2^+, CO^+, H_2^+, H_2O^+, O^+, O_3^+, NO^+, NO_2^+.

$$X + GCR \rightarrow X^+ + e \tag{1.12}$$

Other complex ions such as $CO_2^+CO_2$, $O_2^+CO_2$, H_3O^+, $H_3O^+H_2O$, $H_3O^+(H_2O)_2$, and $H_3O^+(H_2O)_3$ are found in the lower atmosphere as a result of complex chemical reactions (Sheel and Haider, 2012).

Due to the ionization by precipitating GCR particles Martian lower atmosphere contains free electrons, as given by the above reaction. These free electrons are captured by the electron affinitive neutrals such as O, O_2 and O_3 and produce O^- and O_2^-.

$$O_2 + e + CO_2 \rightarrow O_2^- + CO_2 \tag{1.13}$$

$$O + e \rightarrow O^- + h\nu \tag{1.14}$$

$$O_3 + e \rightarrow O^- + O_2 \tag{1.15}$$

Further reactions lead to the dominant ions such as CO_3^-, CO_4^-, and their hydrated ions in the lower atmosphere (Sheel and Haider, 2012).

The temporal variations in the upper ionosphere are a result of the variations in the ionizing solar EUV radiation and X-rays. However, D region of the Martian ionosphere is subjected to the seasonal changes due to the temporal changes in the neutral densities of species like water vapour and of dust, the study of which is one of the objectives of this thesis work.

1.3 Objectives

The progress in understanding the Martian atmosphere made in the last few decades laid out the ground for the more complex analysis of the neutral and ion composition of the atmosphere. The one dimensional perspective of the Martian atmosphere is well understood from photochemical models. However, the seasonal and geographic variations of atmospheric constituents are linked to many phenomena such as water cycle, dust cycle and transport of the atmospheric constituents. For such studies, one needs to employ realistic general circulation models (GCM). The ionosphere of Mars affects and is affected by, the chemistry, dynamics, and energetics of the neutral atmosphere. For example, as discussed above, the variation in the lower ionosphere is triggered by the variation in the density of water vapour. The objective of the research work is to give an overview of the important neutral species and to understand their seasonal and latitudinal variation. The

previous ion models examined the formation of the ions considering mean atmospheric conditions. With the ability to run a GCM for a specific Martian year, we have now the opportunity to study the ionosphere in a more realistic fashion. The specific objectives for the thesis work are listed below.

1. To understand the seasonal and spatial behavior of the trace neutral species in the Martian atmosphere.

2. To estimate the densities of the major ions over different latitudes and during different seasons with the help of ion model developed at PRL with 35 ion species and with 12 neutral species as input which will be derived from the current version of GCM.

3. To understand the effect of dust on the positive and negative ions of the lower atmosphere for various season.

The specified research objectives are achieved from observations and modeling of the Martian atmosphere. For these studies, carried out for this thesis, the applied methodologies are described in chapter 2. In Chapter 2 we describe first the procedure to retrieve ozone and dust opacities from the radiance recorded by the UV spectrometer SPICAM. This consists of building an appropriate forward model for the Martian atmosphere to generate theoretical radiances corresponding to each observation, by determining Rayleigh and Mie scattering for atmospheric gases and dust respectively and employing a nonlinear fitting method to ultimately determine the ozone column and dust optical depths. In chapter 2, we also describe photochemistry coupled LMD-GCM which we run for MY 27. Lastly, we discuss about the PRL ion-dust model which uses as input, the neutral densities from the LMD-GCM simulation to study the seasonal variation in ion species of the lower atmosphere. Chapter 3 is dedicated to giving an overview of the temperature and composition corresponding to the MY 27, as simulated by the GCM. Study of the important tracers such as O, O_3, CO, and HO_x are the subject matter of Chapter 4. Chapter 5 describes the seasonal and latitudinal variation in the ion densities and their dependence on the dust and water vapour for the MY 27. We summarize and conclude the thesis with also a discussion about future work in chapter 6.

Chapter 2

Methodology

The aim of the thesis work is to study the ion-neutral structure of the lower atmosphere of Mars extending from the surface to 80 km. In this chapter we describe the models used for the study, namely the PRL ion-dust model and the photochemical coupled general circulation model (GCM) Observations of ozone and dust optical depths, are used in the current work. The observed quantities are retrieved from the radiance measurement obtained by a UV spectrometer SPICAM onboard Mars EXpress (MEX). The retrieval procedure will also be discussed in chapter 2.

The GCM is used to study seasonal variability of trace atmospheric constituents at different latitudes. The ozone and dust optical depths retrieved from radiance measurements are used to study ozone-dust correlation and spatio-temporal variability of ozone. Observed ozone is also compared with GCM simulations. The ion-dust model developed earlier at PRL, is used to study seasonal variability of the lower ionosphere at different latitudes in the current work.

2.1 Ozone and dust retrieval

Observations from SPICAM (Spectroscopy for the Investigation of the Characteristics of the Atmosphere of Mars) UV spectrometer onboard the Mars Express (MEX) are used to retrieve columnar ozone. These observations are available in the form

of radiance recorded by the spectrometer in nadir view (Perrier et al., 2006; Bertaux et al., 2006). The spectral resolution of the spectrometer is about 1 nm/pixel, and the resolving power is 120–300. A typical recorded spectra is shown in Figure 2.1.

The spectrometer is made of two units, one is called sensor unit and the other is called data processing unit. Lights are collected by a parabolic mirror which directs them to the slit of the spectrometer after which photons are collected at the CCD camera and a counting in ADU is produced through the data processing unit. The spectrometer is operated in various modes, such as nadir, limb, grazing limb, solar occultation, and star occultation. For our purpose of retrieving columnar ozone and dust optical depths, we have used the observations obtained in nadir mode. For descriptive discussion of UV sp-

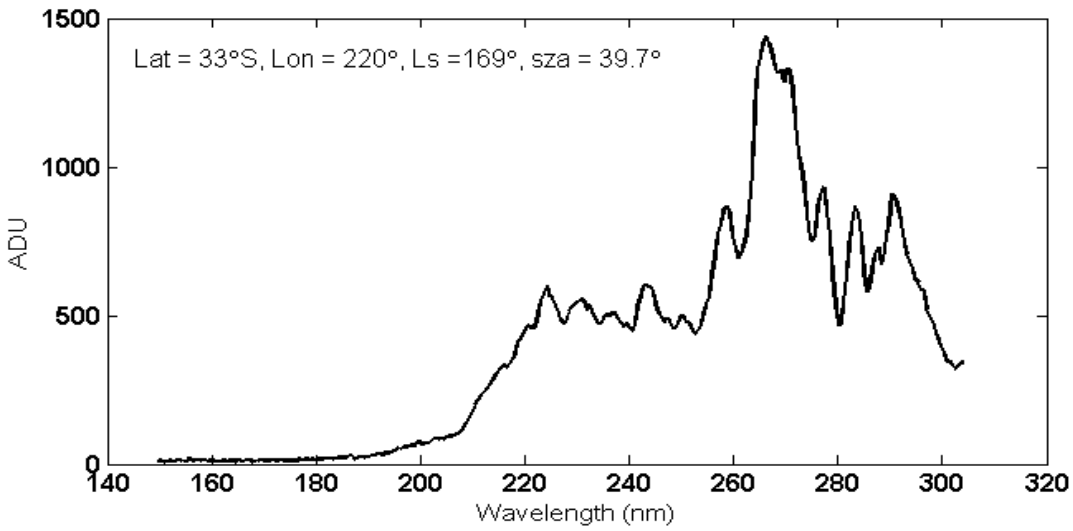

Figure 2.1: A typical raw spectra recorded in nadir geometry by SPICAM.

-ectrometer and the definition of the observing modes one can refer to Bertaux et al. (2006).

SPICAM records the UV radiation in dayside, back scattered by the atmospheric gases and dust in Martian atmosphere. Observations are recorded in the wavelength range of 110–320 nm, allowing measurement of ozone, which has a characteristics Hartley band absorption spectrum in the wavelength range of 210 nm to 300 nm, with a peak at 255 nm. This characteristic absorption gets imprinted in the back scattered solar radiation received by SPICAM. In this wavelength region other gases such as CO_2, N_2, O_2, H_2O, are less

absorptive in comparison with O_3, which makes the ozone column determination easier. For the current purpose of retrieval we have used ozone absorption cross sections from Malicet et al. (1995), which is consistent with the recent reports by Gorshelev et al. (2014) and Serdyuchenko et al. (2014). The absorption cross section values represent the ability of a molecule to absorb photons. However, Rayleigh scattering and absorption and scattering by dust have to be accounted for while retrieving ozone. In order to retrieve ozone and dust values from the SPICAM observations, theoretical spectra need to be compared with the observational spectra. An iteration is performed until the ozone and dust values correspond to the best fitted theoretical spectra. The radiative transfer model and the model atmosphere used to do so, are described in section 2.1.2.

2.1.1 Raw Data and retrieval method

The Mars Express which is in an elliptical polar orbit with a 7 hour period, started observations in January 2004, at Ls = 331° (MY 27). We have retrieved observations for MY 27 and MY 28. This corresponds to 4149 orbits from orbit number 61 (MY 27, Ls = 7°; 19 March 2004) to orbit number 5055 (MY 28, Ls =359.74^o; 9 December 2007). The numbers of orbits in individual years MY 27 and MY 28 were 2331 and 2216 respectively. The analysis resulted in around 51721 spectra with high-S/N (Signal to noise ratio) (28273 spectra for MY 27, 23448 spectra for MY 28).

We have taken level 1A data from the Geosciences Node of ESA's Planetary Science Archive (ftp://psa.esac.esa.int/pub/). These data are corrected for dark charge, electronic noise, erroneous data, damaged by cosmic rays and saturations. Each nadir observation is typically 30 minutes long and records almost 1000 spectra, spectral radiance being recorded each second. SPICAM records spectra in five contiguous bins each second. Each bin is characterized by the number of CCD lines grouped together (Bertaux et al., 2006). Spectra recorded in each bin are averaged to obtain a mean spectrum from which ozone is extracted. We then averaged 50 consecutive spectra to improve the signal to noise ratio. This results in 30 to 40 individual spectra. Each recorded radiance (I) is divided by the flux at the top of the atmosphere (F) yielding the radiance factor I/F.

Perrier et al. (2006) has reported that the spectra suffer from the internal stray light by 8 – 12 % of its total intensity. Bertaux et al. (2006) reported the stray light contribution to the recorded data as 10% of recorded intensity. We integrated each spectrum over the operating range of SPICAM-UV spectrometer.

$$I = \int I_{\lambda} d\lambda \tag{2.1}$$

Let us say, $I_{stray}(\lambda)$ represents the stray light associated with any particular spectra recorded by SPICAM at wavelength λ.

$$I_{stray}(\lambda) = 0.1 \times I \times (I_b(\lambda) / \int I_b(\lambda) d\lambda) \tag{2.2}$$

where $I_b(\lambda)$ is the intensity (ADU) associated with the stray light spectra (Bertaux et al., 2006).

Then, the corrected spectra is given as

$$I_{corrected}(\lambda) = I_{SPICAM}(\lambda) - I_{stray}(\lambda). \tag{2.3}$$

The averaging over 50 consecutive spectra results in 30 to 40 individual spectra. This has been done in order to increase the signal to noise ratio. The final intensity is expressed in terms of KR/nm (Kilo Rayleigh per nanometer). The final quantity is converted into radiance factor (I/F) where πF is the solar flux received by SPICAM.

2.1.2 Forward model

To simulate a theoretical spectrum corresponding to each observational spectrum, we developed a forward model. We solve the following radiative transfer equation in the nadir direction using SHDOM (Simple Harmonic Discrete Ordinate Method) (Evans, 1998) model for a plane parallel atmosphere.

$$\frac{dI_{\nu}}{d\tau_z} = S_{\nu} - I_{\nu} \tag{2.4}$$

where, $I_{\nu}$is the spectral radiance at height z in units of power per unit area, per unit solid

angle, per unit frequency interval in the neighborhood of the frequency ν. S_ν is the source function at height z. The optical depth of the atmosphere at height z is defined as

$$\tau_\nu(z) = \int_0^z k_\nu(z')\,\rho_i(z')dz'$$

(2.5)

where $k_\nu$is the coefficient of extinction due to absorption and scattering by a species *i* whose density is ρ_i. The integral form of the above radiative transfer equation is written as

$$I_\nu(z) = \int_0^z S_\nu(z')k_\nu(z')\rho_i(z')\exp\left[-\int_{z'}^z k_\nu(t)\rho_i(t)dt\right]dz' + I_\nu(0)\exp(-\tau_\nu(z)) \quad (2.6)$$

where, the variable $t = z - z'$. Numerically, we perform the above integral using the discrete ordinate method and representing the angular part of the source function S_ν and I_ν in terms of spherical harmonics expansion. The method is called the simple harmonic discrete ordinate method, SHDOM (Evans, 1998). This method is computationally more efficient than standard methods. The source function includes contributions due to the scattering and absorption from diffused radiation. Mathematically, the source term in the direction Ω can be written as

$$S_\nu = \frac{\tilde{\omega}}{4\pi}\int_0^{4\pi} I(\tau,\Omega')P(\Omega,\Omega')d\Omega' + \frac{\tilde{\omega}}{4\pi}F_\odot P(\Omega,\Omega_0)e^{-\frac{\tau}{\mu_0}} + (1-\tilde{\omega})B[T(\tau)] \quad (2.7)$$

where Ω is the solid angle defined by the angles (θ,φ). $\tilde{\omega}$ is the single scattering albedo, $P(\Omega,\Omega')$ is the phase function between the directions Ω and Ω', $F_\odot$ is the direct solar flux at the top of the atmosphere. $B[T(\tau)]$ is the Planck function for the IR radiation from Mar's surface. The source function comprises of the single scattering, multiple scattering, and the absorption terms. Multiple scattering for diffuse radiation along the direction Ω is given by the first term on the right hand side. The term physically represents the contributions of diffuse radiations from all the directions towards the direction, Ω. The second term represents the single scattering contribution of the direct solar flux along the direction Ω. The last term represents thermal radiation from the surface of Mars which is neglected in our forward modelling. Phase function which is a measure of the angular distribution of the incident energy is expressed as a Legendre series expansion.

$$P(\cos\Theta) = \sum \chi_L P_L(\cos\Theta) \tag{2.8}$$

Ideally, the series is continued to infinite terms but in our analysis, we have truncated when the values of expansion coefficients become less than 0.00001.

2.1.3 Model atmosphere

In order to extract ozone column from the spectra of the recorded radiance, a model atmosphere is required corresponding to the geometry of every spectrum. Such an atmosphere is built with the help of Mars Climate Database (MCD) version 5.2 (Millour et al., 2015) and is divided into 12 equal layers up to 60 km. Changes in surface pressure can greatly affect the theoretical radiance. The MCD version 5.2 takes care of the Martian topography with help of MOLA (Mars Orbiter Laser Altimeter) data, due to which the surface pressure derived from MCD are non-scaled. Therefore, for a given place, vertical layers start from the surface and there is no reference level used in the forward model. For the ozone extraction, surface pressure, temperature profile and dust vertical profile is an important input. For the determination of the radiative properties of the atmosphere, appropriate calculation of dust extinction and Rayleigh scattering needs to be done. Among the other inputs, we have provided dust effective radius, dust density and ozone vertical profiles from MCD to the radiative transfer model suitable for the geometry of the spectra to be fitted.

2.1.4 Rayleigh scattering

Rayleigh scattering is the simplest kind of scattering which is responsible for the blue colour of the sky. The scattered intensity is proportional to a factor $\frac{1}{\lambda^4}$ where λ is the wavelength of the incident radiation. Since the Martian atmosphere is CO_2 dominated, it is 2.5 times more scattering than Earth's atmosphere (Forget and Pierrehumbert, 1997). Recent reevaluation of Mars' atmospheric gases by Franz et al. (2015) shows that the atmosphere is made up of 95.7% of CO_2, 2.07% of Ar and 2.03% of N_2. Thus calculation of CO_2 Rayleigh scattering cross section becomes important. Theoretically, Rayleigh cross section (σ_ν) is defined as follows.

$$\sigma_\nu = \frac{24\pi^3\nu^4}{N^2}\left(\frac{n_\nu^2-1}{n_\nu^2+2}\right)^2 F_k(\nu) \tag{2.9}$$

where ν is the wave number, N is the number density of the gas under experiment, n_ν is refractive index and $F_k(\nu)$ is King's factor (Sneep and Ubachs, 2005). For the cross section of N_2 and Ar we have calculated refractive index from the expression given below (Thalman et al., 2014)

$$(n-1)\times 10^8 = A + \frac{B}{C-\nu^2} \tag{2.10}$$

Once refractive index n is calculated, the cross section can be obtained from the Equation (2.9). Laboratory measured Rayleigh scattering cross section for CO_2 does not agree with the calculation from Equation (2.9) (Sneep and Ubachs, 2005) and it is not exactly proportional to$1/\lambda^4$. Following Willame et al. (2017) we have calculated the cross section from the equation $\sigma = \overline{\sigma}\times\nu^{4+\epsilon}$ fitted on the measured data where the values of the parameters are $\overline{\sigma} = 2.247\text{x}10^{-45}$ and $\epsilon = 0.3801$. The parameters values are better than 1% and the experiment was made for the wavelength range between 408 and 532 nm which we have extrapolated to the UV region which is important for ozone retrieval.

2.1.5 Dust scattering

Rayleigh scattering is important when the size of particles is comparable with the wavelength of the incident radiation. The comparison is measured by the size factor $2\pi a/\lambda$ where a is the radius of the particles. Mie scattering becomes important when the size factor is greater than unity. In the Martian atmosphere effective radius (r_{eff}) ranges from 2.0 µm near the surface to 0.05 µm above 50 km. Dust scattering and absorption are calculated from Mie theory considering spherical dust particles. The phase function for dust scattering is calculated from the Legendre series expansion. The coefficients of the following series for phase function is calculated and fed as input to the SHDOM solver. The refractive index in the UV wavelength range of consideration has been taken from Wolff et al. (2010). In Figure 2.2, the phase function for a particles of radius 0.1µm and

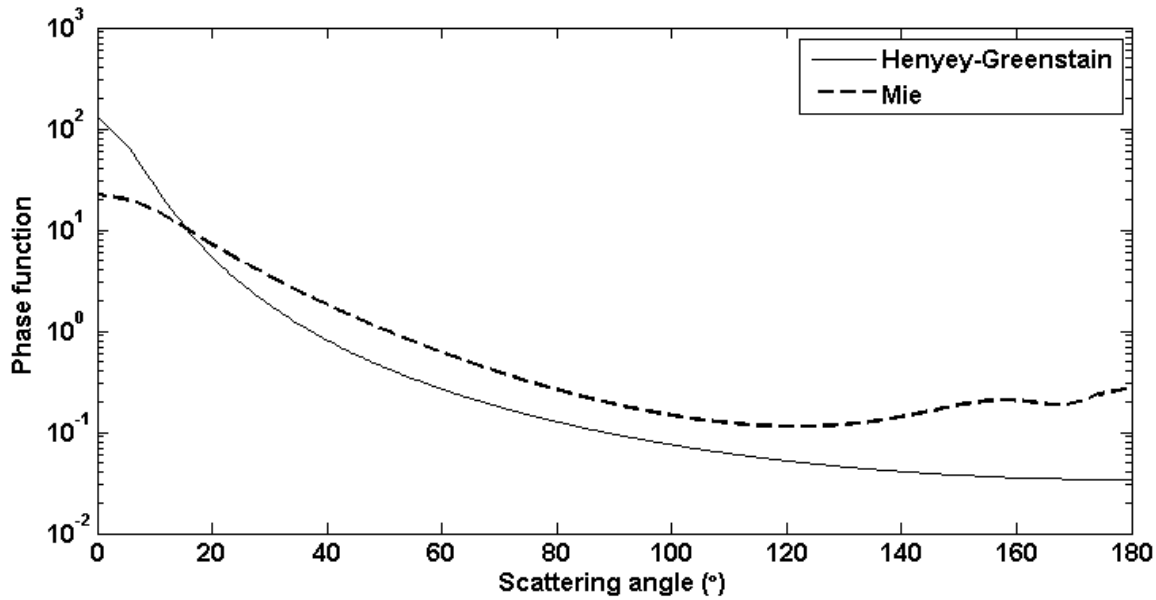

Figure 2.2: Phase function for particle of radius 0.1μm calculated from Mie theory and compared with Henyey–Greenstein phase function.

it's comparison with Henyey-Greenstain phase function are shown. In our calculation we have used full series of phase function. And a truncation has been used only when the values of coefficients are less than 0.00001. The scattering and extinction coefficient are shown in Figure 2.3 for wavelength 220 nm.

Scattering and Extinction efficiencies (Figure 2.3) are calculated for refractive index,$m = 1.0486 - i * 0.0155$. The real part is a slowly varying function of wavelength and that is why we have taken a constant value 1.486 for the present retrieval from Wolff et al. (2009). As for the imaginary part the proper behavior with wavelength in the region 200 – 300 nm is not known. For this region we have used a value suggested in Wolff et al. (2009) for λ= 668 nm. The real part represents the dust scattering while the imaginary part represents absorption by dust. As can be seen from Figure 2.3, the smaller particles scatter more than 90% of incident radiation. In the higher radius the SSA reduces to values approaching 0.6.

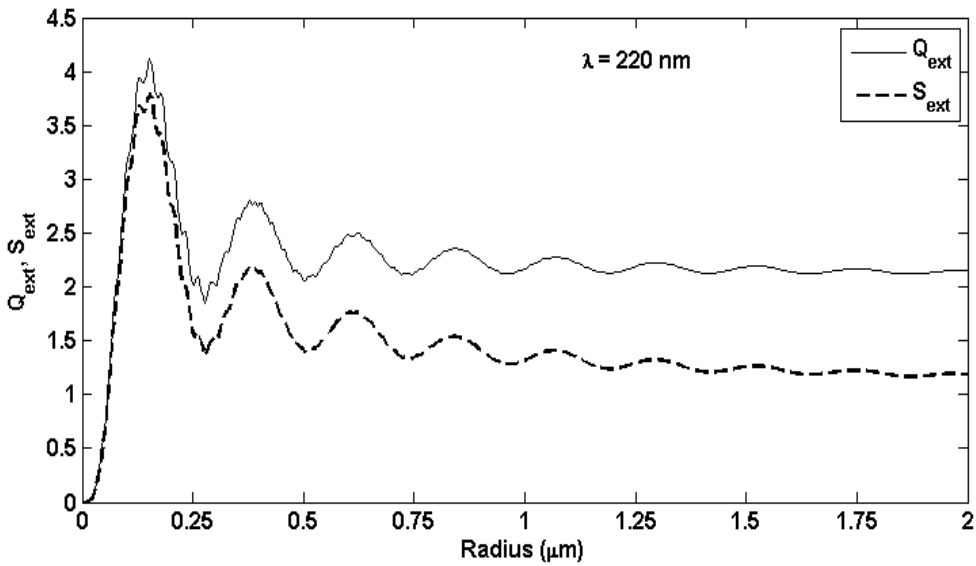

Figure 2.3: Scattering and extinction efficiencies for m=1.486-i*0.0155 and λ=220nm.

2.1.6 Fitting method

Now that we have both the theoretical and observational spectra, we compare them by using a best fit to determine columnar ozone. For this, we select nine points from the observed spectra in the range 210–300 nm. Corresponding to the observed radiance at each point, a theoretical radiance has been calculated using the radiative transfer model discussed in section 2.1.2, with a prior value of ozone column, surface albedo and dust opacity. Mars surface albedo varies from place to place and therefore albedo at 210nm and 300nm are also retrieved simultaneously with ozone. However, the values of albedo are forced to be less than one. All the parameters are kept positive throughout the retrieval. In order to determine total column ozone, the sum of the square of weighted differences (χ^2), has to be minimized. For this purpose, we have used Levenberg-Marquardt minimization method (LM method) which is a nonlinear chi-square minimization method where multiple parameters can be fitted. L-M method which updates the parameters values adaptively works better than gradient descent and Gauss-Newton method. The convergence criterion for the method is that chi-square defined as follows is less than unity.

$$\chi^2 = \left(y - \hat{y}(p)\right)^T W(y - \hat{y}(p)) \qquad (2.11)$$

where $y(\lambda_i)$ are the observations which are functions of wavelength λ_i and $\hat{y}(\lambda_i; p)$ is the fitting function for a vector of parameters p and W is the inverse of the error covariance matrix. We estimate the uncertainties on the ozone column due to our retrieval method. For a known ozone column, we generate synthetic spectra with the forward model. Ozone column are then retrieved assuming that these synthetic spectra were observed by SPICAM. For high dust and moderate ozone (~10 µm-atm (1 µm-atm = 2.69×10^{15} molecules/cm^2)), the errors range between 10% and 30%. The errors are in the same range for low dust and low ozone (~0.5µm-atm). For low dust and high ozone (~ 20µm-atm), errors in retrieved ozone values are within 10% (Perrier et al., 2006). An example of a fitted spectrum for the orbit number 902 (Latitude=31.92°N, L_s=95.31°) is shown in Figure 2.4, where the radiance factor (as de-

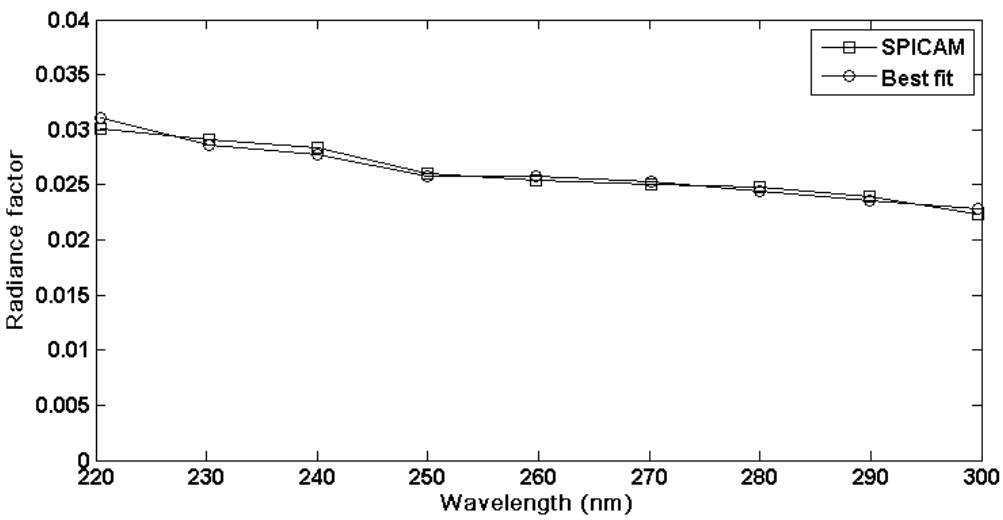

Figure 2.4: Fitted spectrum for orbit number 902 (Latitude=31.92°N, Ls=95.31°). An ozone columnar value of 0.23µm-atm is retrieved for this spectrum.

-fined in section 2.1.1) is plotted against the wavelength. An ozone columnar value 0.23µm-atm is retrieved for this spectrum. The retrieved values of albedo are commensurate with a poor reflector of the UV radiation and are lower compared to those retrieved by Perrier et al. (2006) in the polar region and also during some seasons in the

equatorial region. We have observed that the retrieved ozone values are not very sensitive to the values of albedo especially when there are clouds present.

2.2 General Circulation Model (GCM) for Mars

In this work, we use the LMD General Circulation Model (LMD-GCM), developed in a collaboration of the Laboratoire de Météorologie Dynamique, LATMOS (Laboratoire ATmospheres, Milieux, Observations Spatiales), The Open University, the University of Oxford and the Instituto de Astrofisica de Andalucia. This model uses physical parameterisations such as effects due to CO_2 and dust adsorption and emission, thermal conduction in the soil, CO_2 condensation and sublimation, sub-grid scale dynamics, vertical diffusion, and convection (Forget et al., 1999). In this thesis work, the GCM has been used to study the spatio-temporal variability of trace constituents of the Martian atmosphere.

The LMD-GCM comprises the physical processes such as seasonal sublimation and condensations of CO_2 or CO_2 cycle, water cycle and dust cycle which are specific to Martian atmosphere. These cycles directly change the tracers' densities in the atmosphere. Radiative transfer calculations in the model determine the incoming solar radiation which dissociates the neutral species of the lower atmosphere (Madeleine et al., 2011).

2.2.1 Dust scenarios in the model

Dust is the most unpredictable component of the Martian atmosphere. The strong spatial variability and radiative effect make it difficult to model dust variability due to which prediction of dust storms is difficult. The model uses dust scenarios obtained by assimilation of various observations of orbiters Vikings (Clancy et al., 2000), MGS (Smith 2004), MRO (Murchie et al., 2007) and rovers "Spirit" and "Opportunity" (Bell et al., 2003) into the LMD-GCM. The recent dust climatology is developed by Montabone et al. (2015). The data assimilation is done based on the observations between April of 1999 and July of 2013. The vertical profile of dust is calculated by transported tracers

representing dust mass and dust mixing ration. The photochemistry does not include reactions on the dust surface directly but the dust scenarios affect the solar irradiance which has effect on the photochemistry, i.e. dust profiles are interactive with the GCM radiative scheme (Madeleine et al., 2011). The predicted spatial distribution of dust is used to compute the 3D opacity field, and each opacity profile is then multiplied by a constant to match an interpolation of numerous sets of observations from orbiters and landers using a Kriging method of data assimilation (Montabone et al., 2015). Radiative transfer in the model is able to reasonably reproduce the observed thermal structure of the atmosphere and columnar dust opacities (Madeleine et al., 2011), after incorporation of appropriate dust radiative properties (Wolff et al., 2006, 2009). The model, however, could not generate the high altitude tropospheric dust.

2.2.2 Water cycle and clouds

Major source of the water vapour for the Martian atmosphere is the water ice beneath the polar caps. The water cycle initially incorporated in the model (Montmessin et al., 2004), overestimated the cloud opacities of equatorial cloud belt, as radiative feedback of clouds and their interaction with dust particles were neglected. The scheme does not use the nucleation of ice particles onto dust particles, instead it uses the number of ice particles as a fraction of the available dust particles. A new microphysical scheme is introduced in the GCM that considers the radiative effects of clouds to represent cloud particles nucleation on dust particles, ice particle growth, and scavenging of dust particles resulting from the condensation of ice. Overall, a better simulated thermal structure from the use of radiatively active clouds, leads to a qualitative improvement of the modeled water cycle in the GCM (Navarro et al., 2014). In the cloud scheme introduced by Navarro et al. (2014), ice cover is taken as a function of temperature in latitudes greater than 65°.

2.2.3 Radiative transfer

Proper knowledge of dust distribution and its radiative properties (extinction coefficient, single scattering albedo and asymmetry parameter) is important for the

construction of temperature profile of any atmosphere. The dust radiative properties incorporated by Madeleine et al. (2011), in the model is used to overestimate observed temperature. Due to the overestimation in the dust loading, the absorption of solar radiation in the atmosphere was increased which resulted in an overestimation in temperature. In the current version of LMD-GCM dust is transported according to van Leer scheme and the vertical distribution is achieved as described in section 2.2.1. The radiative properties of dust are improved by Wolff, (2006) and (2009) using CRISM observations. The inclusion of the improved radiative properties in the radiative transfer calculation of the model and tuning the dust optical depth (dod) to match the observed ones, improved the temperature calculations in the model.

2.2.4 CO_2 seasonal cycle

During winter, CO_2 condenses onto polar caps. The condensation reduces as much as ~ 30% of the atmospheric mass (Forget and Pierrehumbert, 1997). This polar process affects the mixing ratios of the non-condensable gases as well. The condensation alters the atmospheric mass which indirectly affects the other derivative species such as O, CO, OH. Present GCM calculates the changes in the gas amounts due to condensation. Therefore, consideration of the heat exchange between surface and atmosphere, atmospheric condensation and sublimation are important for the photochemistry of the Martian atmosphere. The heat exchange between surface and atmosphere is governed by the following equation.

$$C\frac{\partial T}{\partial t} = \nabla . F_c \qquad (2.12)$$

where C (unit : $J.m^{-3}.K^{-1}$) is the volumetric specific heat, defined by $C_p\rho$ where C_p is specific heat at constant pressure and ρ is the density in $Kgm^{-3}$of Martian soil. And F_c is the conductive heat flux between surface and atmosphere. F_c is defined by $F_c = \lambda\nabla T$ andλ is the heat conductivity of the Martian soil. Condensation of CO_2 directly affects the surface pressure of the atmosphere. If δm is the ice condensed per unit time per unit area

then, the change in the surface pressure is $\delta p_0 = -g\delta m$ where g is the gravitational acceleration.

2.2.5 Photochemistry

Ozone, water vapour, carbon monoxide, and other species are simulated by a photochemical module (Lefèvre et al., 2004) coupled to the GCM. The module consists of 36 chemical and 14 photochemical reactions. The chemical species are transported by the van Leer advection scheme. The advection scheme uses wind fields updated by the dynamical core to determine the species concentration at each model grid point every 90 seconds (dynamical timestep). The chemical fields are exchanged between the GCM and photochemical model each physical timestep (20 x dynamical timestep) for a fully interactive coupling among dynamics, physical parameterisations, and chemical species. The temperature simulated by the GCM is an input to the reaction rates that are temperature dependent, as the photochemistry is coupled to the GCM. The long lived species such as CO are calculated using implicit methods described in Shimazaki 1985, and short lived species such as $O(^1D)$ are considered in photochemical equilibrium for all time. The physical processes change tracer concentrations independently.

2.2.6 Simulation condition

The LMD-GCM model is run with appropriate initial and boundary conditions for the year MY 27. Prior to MY 27, the model is run for three Martian years and the tracer mixing ratios thus simulated, form their initial conditions for the MY 27. This allows ample time for spin-up and stabilization of the water cycle and photochemistry. At the very beginning of this 4-year simulation, tracers were initialized globally with minimal mixing ratios (~10^{-8} for ozone, ~10^{-5} for water vapour, ~10^{-10} to 10^{-18} for other species**)**; Argon, N_2 and, O_2 were initialized with values derived by Franz et al. (2015). The tracers are set to zero flux at the surface and at the top of the model as boundary conditions, except for the condensable species H_2O and CO_2 that are condensed out of the atmosphere or sublimated from the ground depending on temperature. Regular gridding of resolution 64x48 (3.75° latitude × 5.675° longitude) is used. For vertical gridding, 32 discrete hybrid sigma-

pressure levels have been used, extending to an altitude of ~122 km. We kept the seasonal cycle of CO_2 and water cycle on. Dust has been treated as a tracer. One sol has been divided into 960 dynamical time steps and we have kept physical time steps 30 minute long. Dynamical time step is the time step used to integrate hydrodynamical equations in the dynamical part of the model (to simulate wind, temperature, and surface pressure). Physical timestep is the timestep to integrate equations in the physical part of the model that deals with chemical reactions, condensation, sublimation and radiative processes. After completing 20 dynamical timesteps, one physical time step is completed. We run the model on the PRL 100 Tf HPC (High Performance Computing) Linux cluster with 100 nodes at the Physical Research Laboratory Ahmedabad, India.

The tracers considered by us are dust, CO_2, CO, O, $O(^1D)$, O_2, O_3, H, H_2, OH, HO_2, H_2O_2, N_2, Ar and water. Seasonal release of CO_2 and its condensation affects the tracers. During winter, CO_2 condenses onto polar caps, which reduces the atmospheric mass by as much as 30% (Forget and Pierrehumbert, 19997). A simple scheme of vertical eddy diffusion is applied in LMD-GCM. The effect of turbulent mixing on tracers are determined by the following equation of diffusion

$$\frac{\partial}{\partial t} = \frac{1}{\rho}\left(\frac{\partial}{\partial z}\left(\rho K_z \frac{\partial}{\partial z}\right)\right) \tag{2.13}$$

where ρ is tracers density and K_z is the mixing (or eddy diffusion) coefficient (Hourdin et al., 1993). The results of the GCM simulation presented in this thesis work does not include heterogeneous chemistry (Lefevre et al., 2008).

Sources of uncertainties in the model are associated with important photochemical and kinetics parameters for Mars. These include reaction rate coefficients and also temperature dependent absorption cross section for CO_2, O_2, O_3 and H_2O_2 used for the computation of photolysis rates. Their effect on the photochemical coupled LMD-GCM simulated ozone is discussed in detail by Lefevre et al. (2004). CO_2 photolysis is the primary source of odd oxygen at all altitudes, and also CO_2 absorption spectrum effects

photolysis of species like H_2O and O_2. Thus uncertainties in the temperature dependent CO_2 absorption cross sections, for example, have shown to change the values of J_{H2O} by about 100% between 30 and 50 km. This sensitivity of CO_2 absorption cross sections to low temperatures (below 200 ^oK) in the middle altitude regions (140-160 ^oK), is not seen for lower altitudes where temperature is higher.

2.3 Ion model

The one-dimensional ion-dust model which simulates densities of positive and negative ions in the presence of dust in the Martian atmosphere was developed at the Physical Research Laboratory (PRL) (Haider et al, 2010; Sheel and Haider, 2012; Sheel and Haider, 2016). The model has been used to study the lower ionosphere of Mars and the effect of dust on the ionosphere. In this ion model, more than 100 reactions have been incorporated, such as ion-neutral, electron-neutral, photodissociation of positive and negative ions, electron photodetachment, ion-ion, and ion-electron recombination. These chemical reactions are defined below.

Ion-neutral reaction

$$X^+ + Y \rightarrow X + Y^+ \qquad \text{charge exchange}$$

$$X^+ + Y \rightarrow Z + W^+ \qquad \text{ion-neutral chemical reaction}$$

Electron-neutral reaction (Electron Capture)

$$Z + e + M \rightarrow Z^- + M$$

Photodissociation of positive and negative ions

$$XY^+ + h\nu \rightarrow X + Y^+$$

Recombination

$$X^+ + Y^- \rightarrow \text{neutral products} \qquad \text{ion-ion recombination}$$

$$X^+ + e \rightarrow X \qquad \text{ion-electron recombination}$$

Electron photodetachment

$$Z^- + h\nu \rightarrow Z + e$$

The following continuity equation is solved for the ion densities, X_i

$$\frac{dX_i}{dt} = P_i - X_i l_i = P_i - L_i \qquad (2.14)$$

where P_i is the production rate of ith gas and l_i is the loss rate coefficient and L_i is the loss rate of the ith gas. The production and loss rate of the reaction of general form $A^+ + B \rightarrow C^+ + D$ is given by $k[A^+][B]$ where k is the temperature dependent reaction rate coefficient. The above continuity equation is solved under steady state condition to calculate the densities of 35 positive and negative ions.

2.3.1 Ion chemistry of the lower atmosphere

Figure2.5 shows the chemical scheme used in the ion-dust model. In the model 12 neutral species CO_2, Ar, N_2, O_2, CO, H_2, H_2O, O, O_3, NO, NO_2 and HNO_3 are ionized by galactic cosmic rays which produces the initial positive ions CO_2^+, Ar^+, N_2^+, O_2^+, CO^+, H_2^+, H_2O^+, O^+, O_3^+, NO^+, NO_2^+ and HNO_3^+. The scheme is built using a total of 40 ions. Besides the 12 initial ions, other 23 ions are produced via the scheme shown in Figure 2.5. These ions are $O_2^+CO_2$, H_3O^+, $H_3O^+H_2O$, $H_3O^+(H_2O)_2$, $H_3O^+(H_2O)_3$, H_3O^+ $(H_2O)_4$, H_3O^+HO, $CO_2^+CO_2$, CO^+, NO^+CO_2, $O_2^+(CO_2)_2$, $O_2^+H_2O$, $O_2^+(H_2O)_2$, O_4^+, $CO_3^-H_2O$, CO_3^- $(H_2O)_2$, CO_3^-, CO_4^-, NO_2^-, $NO_2^-H_2O$, NO_2^- $(H_2O)_2$, NO_3^-, $NO_3^-H_2O$, NO_3^- $(H_2O)_2$, O_2^-, O_3^- and O^-.

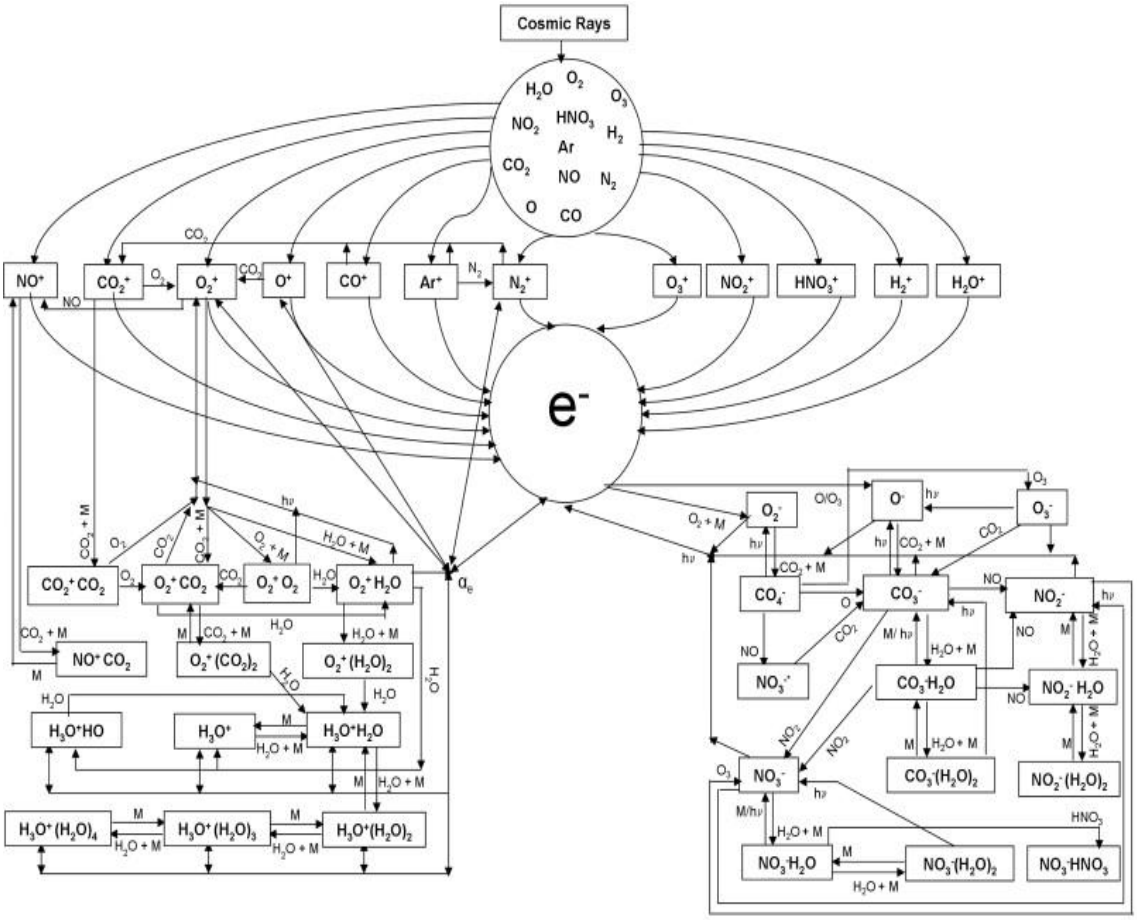

Figure 2.5: Chemical processes in the lower ionosphere of Mars. Image credit: Sheel and Haider, (2012).

The vertical profiles of the positive and negative ions obtained under a very low dust loading are shown in the Figure 2.6. The upper panel of Figure 2.6 shows the positive ion densities and the lower panel shows the negative ion densities. From the Figure 2.6 (upper panel) it is clear that the major positive ions are $H_3O^+(H_2O)_2$ and $H_3O^+(H_2O)_3$ while other ions minor in comparison. The major negative ions are $CO_3^-H_2O$, CO_3^- $(H_2O)_2$, and NO_2^- H_2O as can be seen from the lower panel of Figure 2.6.

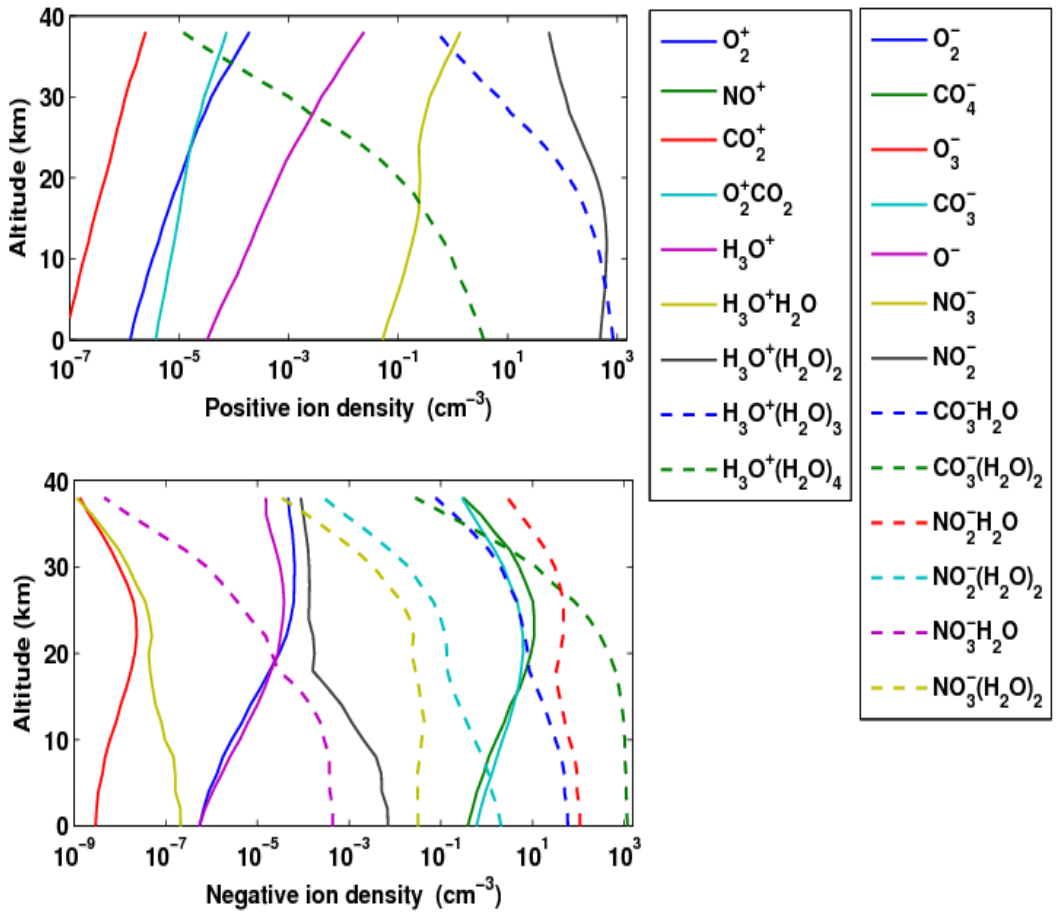

Figure 2.6: Model calculation of positive and negative ions from Haider et al. (2010) for low dust loading.

Chapter 3

Thermal structure and composition of the Martian atmosphere

Temperatures of the atmosphere and its gaseous composition, are the fundamental parameters that characterize any planetary atmosphere. The goal of this chapter is to present an overview of the Martian atmospheric composition and thermal structure. Although CO_2 is the major component of the atmosphere, other minor constituents and trace gases play an important role in the photochemistry and ion chemistry, just as on Earth. For example, the atmospheric constituents such as O_3, H_2O, CO, and dust etc. are known to have substantial role in determining the stability of the atmosphere. Like the Earth's atmosphere, in the Martian atmosphere due to occurrences of polar warming and polar vortices, temperature structure departs from the depicted temperature profile of chapter 1. Thus, a brief description of the temperature and important neutral constituents, and their seasonal and latitudinal variations are provided in this chapter based on theory and observations.

3.1 Observations of temperature

As described in chapter 1, based on vertical profile of temperature, Martian atmosphere can be divided into troposphere, mesosphere, thermosphere and exosphere. The measurements of surface temperature of Mars predate the space era. First estimate of the surface temperature distribution of Mars was obtained by (Gifford, 1956) radiometrically

from the ground based observations at Lowell observatory between 1926 and 1943. First successful measurements of the meteorological parameters (including temperature) were made with the two landers from Viking orbiters (Chamberlain et al., 1976; Hess et al., 1977*;* Tillman et al., 1994).

Our understanding of Martian atmospheric composition and thermal structure increased substantially with the success of the Viking mission. Viking lander 1 (VL1) landed on the site Lat = 22.5^{o}N and Lon = 48°W and VL2 landed on 48°N Lon = 226°W (Nier and Mc Elroy, 1977). The Viking measurements of the temperature profiles have been accomplished with several instruments during descend of the lander. A set of three axes accelerometer measured the atmospheric density as a function of altitude between 25 and 120 km from which temperature profiles were derived. During the parachute decent, pressure and temperature were also directly measured below 6km (Seiff and Kirk, 1977). The temperature profiles retrieved over the two sites of VL1 and VL2 reveal surface temperatures of 238 ^{o}K and 226 ^{o}K respectively corresponding to solar zenith angles 44° (Nier and Mc Elroy, 1977). From these profiles, a lapse rate of 3.7^o K/km is obtained in the boundary layer which generally lies below 10 km in the Martian atmosphere. The lapse rate was found to decrease to 1.6 K/km between the top of the boundary layer and 40km. A boundary layer of a planetary atmosphere is generally the lower portion of the atmosphere which is strongly influenced by the presence of the planetary surface beneath. This part mediates the primary interactions between surface and the atmosphere. From the surface, the temperature falls to around 160 K at ~40km, above which the atmosphere is nearly isothermal up to 120 km. In this region, fluctuations in the temperature profiles have been observed, which has been attributed to the thermal tides (McDunn et al., 2013).

Observations of temperature profiles have been made by TES onboard MGS from 1999 to 2003 (Smith, 2004). These observations reveal that the planet tends to cool during the aphelion season (Ls = 0°– 180°) while in the perihelion season (Ls = 180° - 360°) there can be an increase in temperature. An increase of 10-15 ^{o}K in the global average temperature during Ls = 180° – 360° has been indicated by the TES observations. A similar

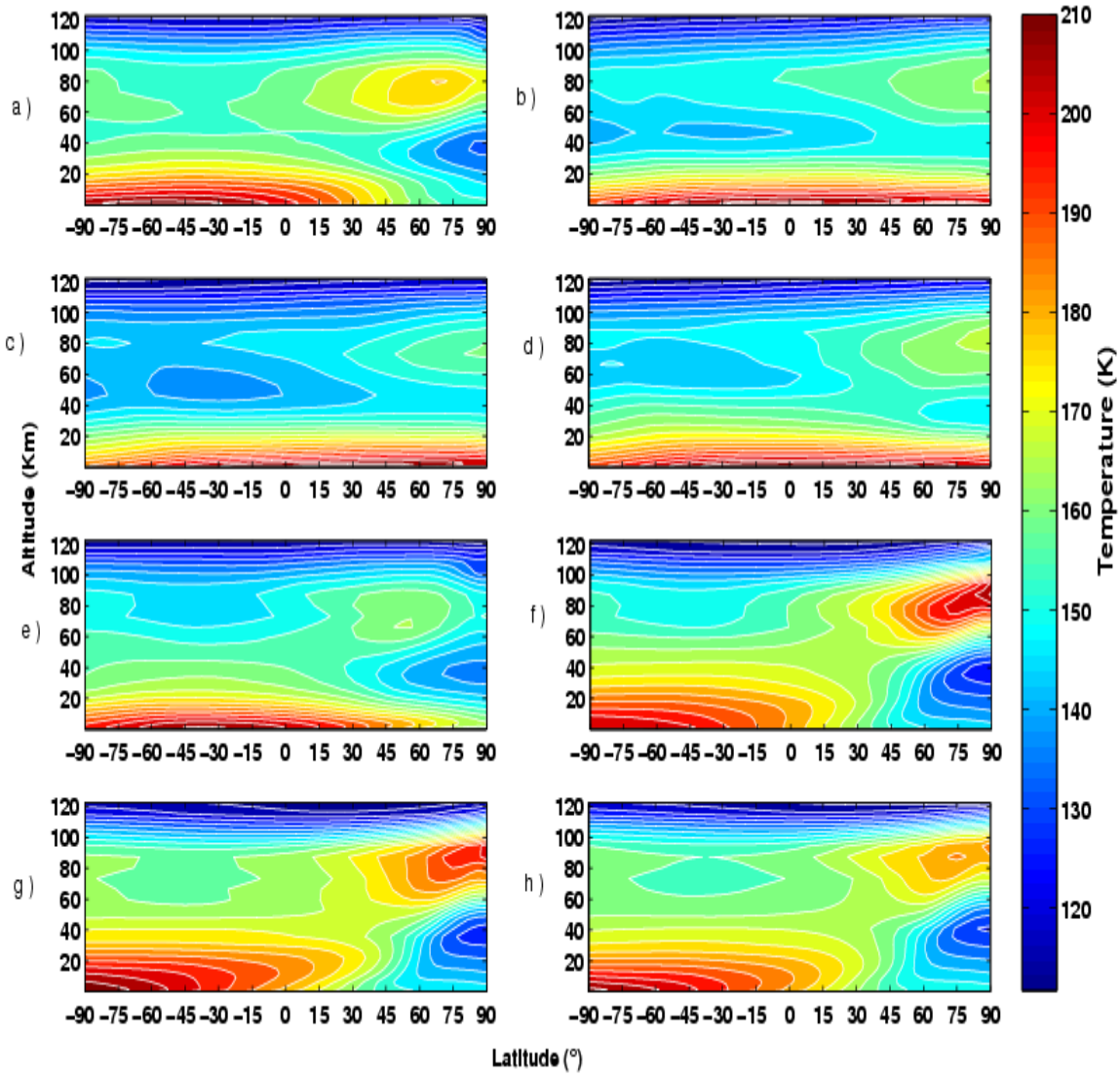

Figure 3.1: Zonal mean average of temperature for (SZA <96º) corresponding to Ls = a) 0º, b) 45º, c) 90º, d) 135º, e) 180º,f) 225º, g) 270º and h) 315º.

increase has been deduced from four to five years of observations by ground based millimeter studies. A detail thermal structure of Mars' atmosphere is presented in McCleeseet. al., 2010. They have also discussed the effect of polar warming and polar vortices in the temperature profiles as a function of latitude and seasons.

3.2 Temperature structure based on GCM

A temperature structure derived from GCM simulations is shown in Fig 3.1. These data are zonally averaged. Each panel from a – h shows latitude-altitude plot of temperature corresponding to Ls = 0°, 45°, 90°, 135°, 180°, 225°, 270° and 315° respectively. In panel (a), we show vertical temperature structure as a function of latitude for Ls = 0° which corresponds to the northern vernal equinox. A surface temperature ~ 200 ^oK is calculated in the latitude region 45^oS to 90^oS. Temperature decreases with altitude and becomes 148° – 150° K at altitudes 40 to 55 km. In the region above this altitude (60 – 80 km) temperature becomes higher ~ 160 ^oK and above 80km temperature falls off. A similar vertical variation of temperature is recorded in the observations made with MCS-MRO (McCleese et al., 2010). However, the surface temperature was 8 – 10 ^oK higher in MCS observation and the lowest temperature recorded in altitude between 40 km and 55 km was 140 ^oK which is 8 – 10 ^oK colder than the GCM-simulated temperature. The increase in temperature between 60 km and 80 km is due to polar warming and the decrease in the 40 km - 60 km region is due to the formation of polar vortices. Over the northern polar region, a distinct polar vortex can be seen in the Figure 3.1(a), whereas in the observations a mild northern polar vortex with temperatures 10 ^oK higher is seen. The corresponding temperatures from the GCM simulation are between 129 ^oK and 131 ^oK over the latitudes 60^oN – 90^oN. The polar warming effect over this region is distinct. A 30 ^oK rise in temperature can be seen compared with the temperatures in the polar vortices. The warming is not present in the equatorial region but a nearly isothermal temperature structure is found. A similar kind of warming is apparent in the MCS observations (McCleese et al., 2010).

In Figure 3.1(b) which shows the temperature profile at Ls = 45°, the southern polar vortex seems to be intensified which is in accordance with the MRO-MCS observations but the polar warming decreases. The atmospheric region corresponding to the polar vortex (40 km-55 km) gets colder by 5 – 6 ^oK compared to that during Ls = 0° over southern high latitudes. In this altitude region colder temperature is found to expand up to

equatorial region which is also visible in the MRO-MCS nighttime observations. In the meantime, temperature rises in northern higher latitudes between altitudes 40 km – 50 km destroying the polar vortex. The effect of polar vortex and polar warming decreases compared to the effect during Ls = 0°.

The temperature between 40 km – 60 km becomes coldest over the southern hemispheric region during Ls = 90° (Figure 3.1 (c)).The effect of polar warming decreases and vanishes over the higher latitudes of the southern hemisphere during remaining seasons of the year (Figure 3.1 (d – h)**).** The increase in temperature due to polar warming is minimum (Figure 3.1 (c)) during the season Ls = 90° over northern high latitudes and also the effect of polar vortex is almost absent. During Ls = 180° the temperature between 40 km and 60 km rises slightly by 5° K–6° K in the southern hemisphere (Figure 3.1 (d)). A hint of formation of polar vortex over the northern hemisphere can be seen during Ls = 180° which started to build up in the later seasons which conformed by the MCS-observations. Also the polar warming effect gets intensified as the planet approaches towards perihelion. The maximum effect of polar warming is seen over the northern high latitudes during Ls = 225° (Figure 3.1 (f)) which then decreases (Figure 3.1 (g) and (h)). Thus, the LDM-GCM temperature simulation matches qualitatively with the observational results from MCS-MRO. The discrepancy between model results and observations can arise from the fact that the observations were made during MY 29 while the simulation is for MY 27.

3.3 Composition overview based on observation

As per our current knowledge, the composition of the Martian atmosphere is given in Table 3.1. The atmosphere consists of few major parent species such as CO_2, Ar, and N_2. CO_2 is the dominant component whose mixing ratio in the homosphere is 95.7% according to the most recent measurement by the Curiosity rover (Franz et al., 2015). First detection of CO_2 was made by Kuiper (1952) but the abundance of CO_2 estimated by him was 4.4 meter-amagot (1 meter-amagot = 2.69×10^{21} molecules-cm^{-2}) which corresponds to half of the atmospheric pressure of Earth. First acceptable abundance of CO_2 was estimated to be

55 m-atm (1 m-atm = 2.69×10^{21} molecules/cm^2) from the observation of near infrared spectrum of Mars (Kaplan et al., 1964). In the space era, the Viking measurements substantially improved our knowledge about the Martian atmosphere. The first sampling of the atmosphere was done by the mass spectrometer in the aeroshell of the Viking lander-1. The sampling reveals presence of N_2 and Ar and also the amount of Ar was determined to be much less (1.6%) than the amount (35 %) predicted for the first time by Mars 6 flyby. The atmospheric N_2 mixing ratio is 2.0%. However, N_2 and Ar do not play a role in the Martian photochemistry.

CO_2 is constantly photolyzed producing CO and O and subsequently O_2. The understanding from simple photochemical models (McElroy and Hunten, 1970; McElroy and McConnel, 1971) predicted high amount of CO but the infrared observations on Mars by Kaplan et al. (1969), Kakar et al. (1977) and Good and Schloerb, (1981) predicted much lower values than those predicted by the previous photochemical models. CO was detected for the first time from high resolution Fourier transform spectra by Kaplan et al. (1969) and the mixing ratio retrieved was 800±300 ppm. Current spacecraft measurements such as by CRISM onboard MRO, PFS onboard MEX, OMEGA onboard MEX, have observed CO through its absorption spectra in the near infrared. These observations infer an approximate mixing ratio of 700 ppm for CO in the Martian atmosphere. A similar concentrations for CO have also been reported by the ground based observations such as spatially-resolved high-resolution spectroscopy (Krasnopolsky, 2003 and Krasnopolsky, 2015) and in-situ observations (Franz et al., 2015). These observations of CO in trace amounts prove that CO is indeed converted back to CO_2, thus explaining the stability of the Martian atmosphere.

The role of water vapour was suggested by models to be important in the oxidation of CO back to CO_2 and thus maintain the stability of the Martian atmosphere (McElroy and Donahue, 1972). It was first detected by Spinrad et al. (1963). Water vapour on Mars is a variable trace gas which decreases in winter and reappears during southern spring and summer (Barker et al., 1970). Condensation and sublimation of the polar frost constitute the seasonal cycle of water vapour. First detailed knowledge of water vapour came from

the MAWD instrument onboard Viking orbiter (Farmer et al., 1977; Jakosky and Farmer, 1982). MAWD measured water vapour columnar abundance as high as 100 pr-µm during Ls = 120° over northern polar region and a global and seasonal average water abundance of 10 pr-µm. Farmer and Doms, (1979) studied global and seasonal variation of water vapour and found that there is a net transport of water vapour from southern polar region to northern polar region in a year. This extra water vapour corresponds to 1 – 2 mg/cm^2 of the deposited ice. Ground based observations such as Clancy and Nair, (1996), and Sprague et al. (1992) observed similar variation of water vapour as MAWD. An attempt of systematic mapping of water vapour has been made by TES onboard MGS (Smith, 2002 and 2004; Pankine et al., 2010). The observations by TES (Smith et al., 2002) measured an annual average of 17 pr-µm in the regions between 10°S and 40°N and 12 pr-µm elsewhere. TES observation also predicted a water vapour gradient from south to north but lower than that predicted by MAWD. Observations have also been made by the instruments SPICAM, PFS and OMEGA (Fedorova et al., 2006; Melchiorri et al., 2007; Tschimmel et al., 2008; Sindoni et al., 2011; Maltagliati et al., 2011 and 2013) on board MEX. Observations have found the maximum water vapour column in the northern polar of about 50-65 pr-µm while over southern polar region the column amount is 25 pr-µm (Fouchet et al., 2007; Tschimmel et al., 2008; Smith et al., 2009; Maltagliati et al., 2011). Systematic attempts to understand the water cycle on Mars have been done by many models (Richardson and Wilson, 2002; Bottger, 2005)

Ozone is one of the important components in the photochemistry of Martian atmosphere and it also plays important role in the stability of the atmosphere. It was detected for the first time by the absorptions of the Hartley band (centered at 255 nm) in the UV as well as IR features by the ultraviolet (UV) spectrometer on board Mariner 7 flyby (Barth and Hord, 1971). Global distribution of ozone (longitudinal averaged) is reported from remote sensing observations by Perrier et al. (2006) and Clancy et al. (2016). In the previous modelling studies ozone was underestimated (Nair et al., 1994), however, Lefevre et al. (2004) obtained a better agreement with observations after establishing a complete water cycle. Various studies have shown that ozone is anti-

correlated with the abundance of water vapour (Willame et al., 2017; Clancy et al., 2016; Fast et al., 2006; Fedorova et al., 2006; Lefevre et al., 2004). This anti-correlation was inferred for the first time from Mariner 9 observations (Barth et al., 1973).

The photolysis of water vapour included in the chemical model lead to the prediction of H_2O_2. H_2O_2 first was detected by Maguire, (1977) from the analysis of the Mariner 9 IR spectra. Later SO_2 was observed by the ground based submillimeter heterodyne spectroscopy (Clancy et al., 2004) and by the thermal infrared imaging spectroscopy (Encrenaz et al., 2004). The main source of the production of H_2O_2 is $HO_2 + HO_2 \rightarrow H_2O_2 + O_2$ and is mainly destroyed by the photolysis. These mechanism was suggested by the one dimensional photochemical model (Parkinson and Hunten, 1972). A higher limit on the H_2O_2 amount was set to 30 ppb by Krasnopolsky et al. (1997) and Encrenaz et al. (2011) from observations with TEXES at InfraRed Telescope Facility (IRTF) derived an upper limit of 0.3 ppb. Clancy et al. (2004) found an average mixing ratio of 18 ppb in the atmosphere below 30 km using ground based observation. In the regions of high water vapour H_2O_2 can be found as high as 20 – 30 ppb which comes down to values below 5 ppb during summer (Encrenaz et al., 2015).

Martian atmosphere also contains CH_4. Formisano et al. (2004) detected methane in very small amount 10±5 ppbv. However, an upper limit of 1.3 ppb was set by Webster et al. (2013) and later its seasonal variability was discovered by in-situ measurements on Curiosity rover (Webster et al., 2015) where methane mixing ratio varies from 0.69 to 7.2 ppb. The origin of methane is not well known (Lefevre and Forget 2009). SO_2 which is thought to be a tracer of CH_4 was detected by Mariner 9 (Maguire, 1977). The global upper limit to SO_2 established by Krasnopolsky, (2005) is 1 ppb. In the present study, we do not include methane or sulfur chemistry in the photochemistry coupled GCM.

Dust is an important component of the Martian atmosphere. It modulates thermal structure of the Martian atmosphere and hence temperature (Gierasch and Goody, 1972; McDunn et al., 2010). Viking landers 1 and 2 measured optical depth during the global dust storm of MY 12. It has been found that before the onset of the global dust storm,

optical depth values (in the visible) rose to 1 on the site of the Viking landers (Pollack et al., 1979). During the dust storm the optical depth may increase to values greater than 2 (Smith et al., 2009). During high dust loading, the temperature is found to decrease. Hence dust may have significant effect on the Martian photochemistry (Lindner, 1988). The Martian surface is the primary source of the suspended dust is the Martian atmosphere. Dust is introduced in the atmosphere through process such as mean wind stress, saltation mechanism, convective vortices (dust devils) and also through electrical effect (Kahre et al., 2004). So far we have a fair understanding of the dust properties from the TES infrared spectral data onboard MGS. Dust optical properties retrieved by Wolff, (2003) predicted an effective radius between 1.5 – 1.6 µm for low and moderate dust loading. Dust single scattering albedo were retrieved from the MARCI spectral data corresponding to the operating wavelength band (Wolff, 2010).

Martian atmosphere is characterized by global dust storms, regional dust storms, and local dust storms (Martin and Zurek, 1993; Smith, 2009; Sheel and Haider, 2016). Due to the differential heating of the Martian surface and due to the topography, seasonal and spatial distribution of dust in Mars is interesting. These dust events change the vertical profile of dust (Heavens et al., 2011; Sheel and Haider, 2016). Dust optical depth varies seasonally during a non-dust storm year, and also with the global and regional storms (Sheel and Haider, 2016). The annual variations of these storms are not fully known. The observations made with THEMIS onboard Mars Odyseey, TES onbarod MGS and MCS onboard MRO have produced data covering MY24 – MY31. These observations show that Martian atmosphere is relatively dust free during Ls = 0° – 180°, but a background dust loading of optical depth 0.1 is always present (Sheel and Haider, 2016). In the latter seasons, regional dust storm appears almost every year. The regional dust storms mostly remain bounded in the southern hemisphere and in the equatorial region and the values of optical depth is higher in the southern hemisphere (Sheel and Haider, 2016). It is still not well known why global dust storms on Mars occur during a particular year and not in others. In the LMD-GCM, dust observations from various missions are assimilated with an aim to provide more realistic simulations (Montabone et al., 2015). The dust scheme

used in the GCM is called semi-interactive scheme (Madeleine et al., 2011), where the vertical abundances of the dust varies with atmospheric mixing but the total columnar abundance of the dust is adjusted according to the dust climatological optical depths (Montabone et al., 2015).

Species	Atmospheric amount	Reference
CO_2	95.7%	Franz et al., 2015
Ar	2.03%	Franz et al., 2015
N_2	2.07%	Franz et al., 2015
O_2	0.173%	Franz et al., 2015
CO	749 ppm	Franz et al., 2015
H_2O	0 – 200 ppm (column averaged) (variable)	McConnochie et al., 2018
O_3	0.02 – 0.2 ppm	Various studies
SO_2	< 2 ppb	Encrenaz et al., 2011
CH_4	0.7 – 7.2 ppb	Webster et al., 2015

Table 3.1: Recent measured mixing ratios of the Martian atmospheric composition

3.4 Atmospheric composition simulated by GCM

As described in chapter 2 the photochemistry coupled LMD-GCM is validated by many observations. The dust scenarios assimilated in the model enable it to produce spatial and seasonal distribution of the atmospheric trace species corresponding to a specific Martian year of the assimilated dust (Montabone et al., 2015). We simulate the GCM for MY 27 and present the results in the below sections.

3.4.1 Nitrogen and Argon

Figure 3.2 and 3.3 show the global map of Ar and N_2 respectively. In the lower atmosphere, N_2 is not very reactive and it only produces NO in the upper atmosphere above 120 km (Mc.Elroy et al., 1977), while Ar is a noble gas. Thus N_2 or Ar do not

participate in the photochemistry of the lower atmosphere below 100 km, which implies that their seasonal distribution is only governed by dynamical transport. The mixing ratios of N_2 and Ar have been estimated from the measurements by the Curiosity rover (Franz et al., 2015). These measurements were made on mission sols 45 (Ls = 175°) and sols 77 (Ls = 194.4°) over the Gale crater (4.5895°S, 137.4417°E), yielding an N_2 mixing ratio of

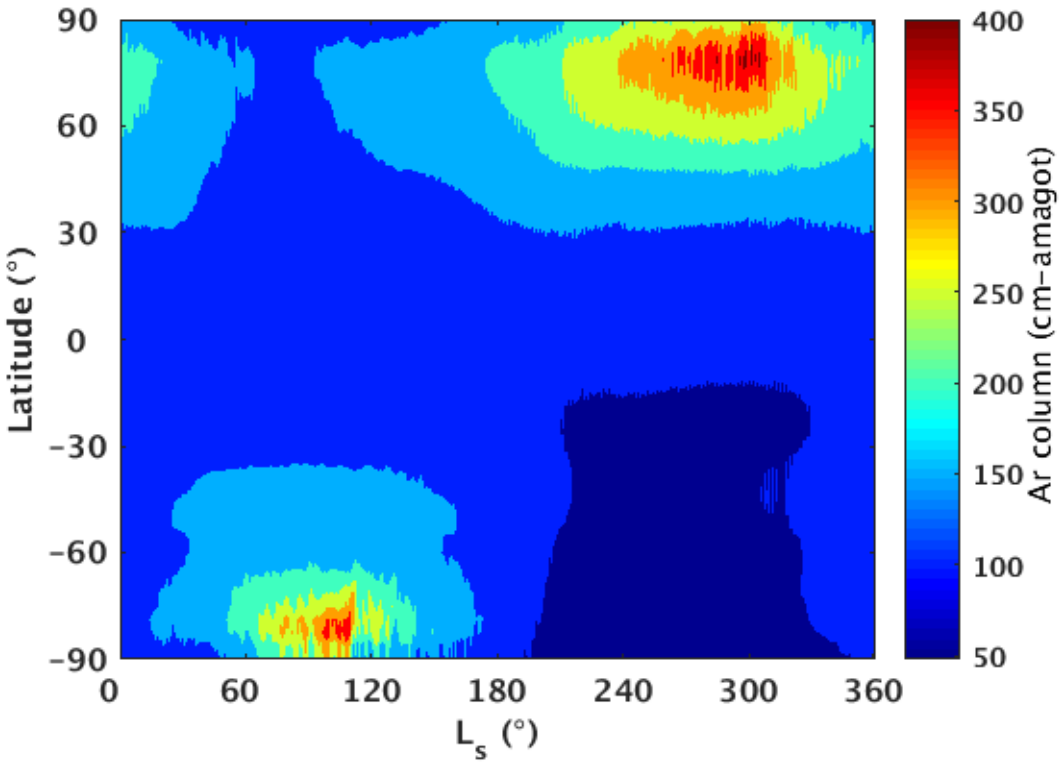

Figure 3.2: Ar columnar distribution (cm-amgot) as a function of latitude and season for MY 27

0.0203 and Ar mixing ratio of 0.0207. The mixing ratios of N_2 calculated from the GCM, corresponding to the mission sols 45 and 77, over the landing site are 0.0192 and 0.0186 respectively. Similarly, the GCM simulated mixing ratios for Ar over the sites are 0.0196 and 0.0190 respectively. The seasonal variability of Ar discussed by Sprague et al. (2007) shows that the maximum abundance is found near the end of the southern autumn and in the beginning of the southern winter in the latitudes between 75°S – 90°S. From the GCM

results, we have found that the maximum abundance of Ar occurs during Ls = 99º – 109º, i.e., the beginning of southern winter.

3.4.2 Carbon Monoxide

Figure 3.3 shows the seasonal variation of the columnar amount of CO in units of cm-amagot (2.69×10^{19}molecules-cm^{-2}). The columnar amounts are averaged over all the

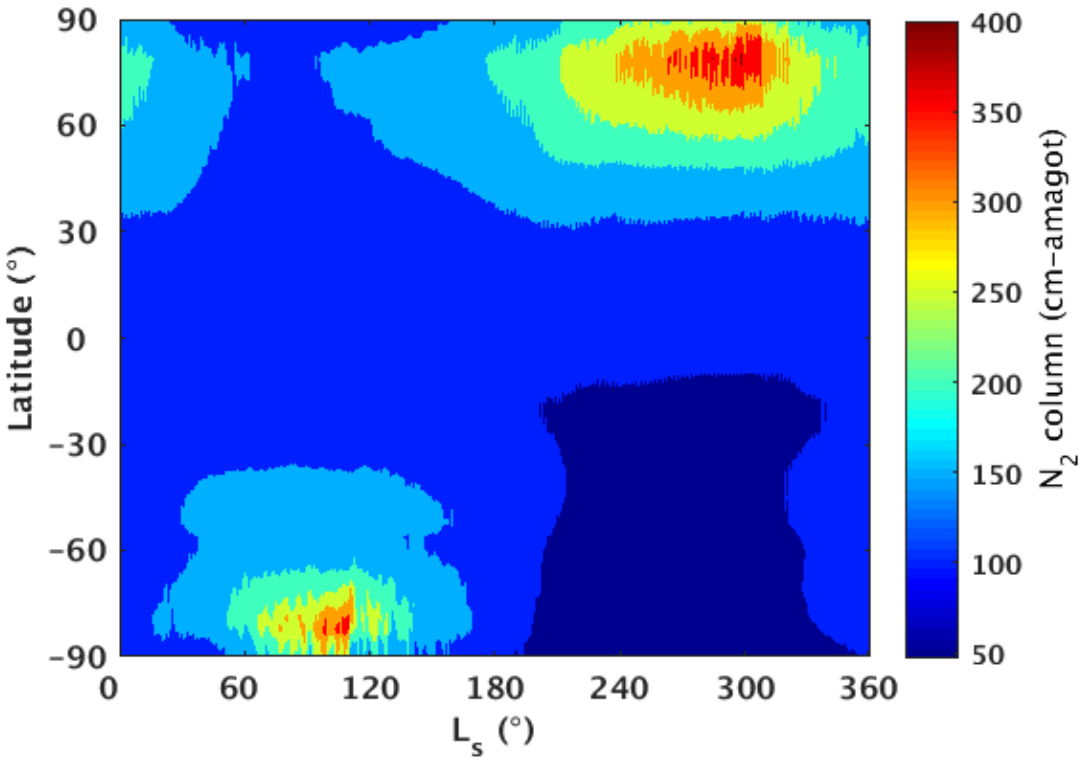

Figure 3.3: N_2 columnar distribution (cm-amgot) as a function of latitude and season for MY 27.

longitudes. CO is mainly produced by the photolysis of CO_2 but due its long lifetime (~ 3.17 Earth years (González-Galindo et al., 2005), it acts as a dynamical tracer and its seasonal variation is mainly connected with the condensation of CO_2 and the dynamical transport (Krasnopolsky, 2015, Clancy et al., 2016). As discussed in the previous section, in the attempts to explain the stability of the Martian atmosphere, CO has been measured and also modeled by many researchers. A columnar value of $4.6\text{x}10^{20}$ cm^{-2} (17.1 cm-amagot) is reported by Clancy et al., 1982 from the measurements of microwave spectra

which is a result of a rotational transition of CO molecule. Our model simulation resulted in a global and annual average of $1.85 \times 10^{20} cm^{-2}$. The microwave measurements of Clancy et al. (1982) suffers from large uncertainties. The columnar value obtained by Clancy et al. (1982) matches with the columnar values retrieved by Krasnopolsky (2015) from

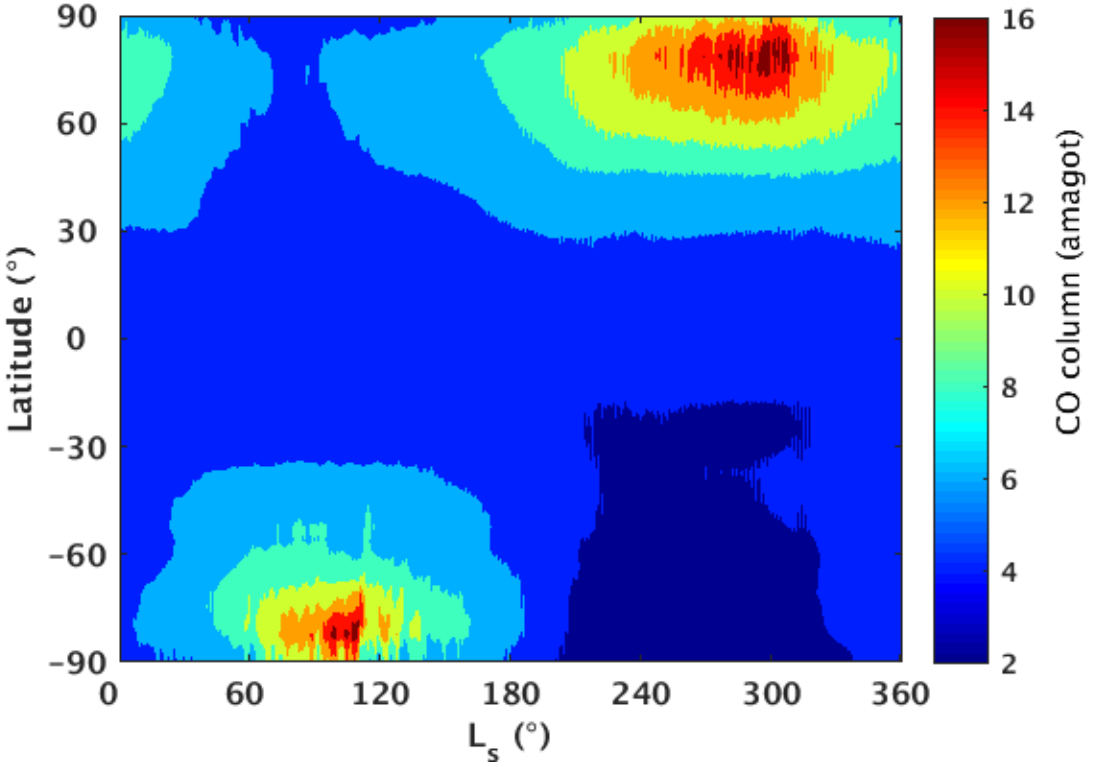

Figure 3.4: CO columnar distribution (cm-amgot) as a function of latitude and season for MY 27

the ground-based spatially-resolved high-resolution spectroscopy over the high latitudes. The seasonally and globally averaged value of CO mixing ratio obtained by their observations is 700 ppm. In our simulation, the global column averaged CO mixing ratio averaged over seasons, was 757 ppm. The observation does not show a depletion of 20%, which is predicted by our simulation over northern high latitudes during summer season. In Figure 3.2 global and seasonal plot of CO columnar values are shown, derived from the LMD-GCM simulation for MY 27. As can be seen, large seasonal variability occurs in the high latitude regions of both the hemispheres. A good qualitative comparison of our

model result can be made with those obtained from CRISM (Smith et al., 2009; Krasnopolsky, 2015). However, we have noticed that in the northern high latitudes, CO is depleted to 537.7 ppm during Ls = 50° – 100° over the latitude region 60°N-90°N, whereas CRISM observation found it to be depleted to 400 ppm.

3.4.3 Water Vapour

Water vapour is one of the most variable trace species and is important for the stability of the Martian atmosphere. It is the only source of the catalytic species HO_x in Martian atmosphere. Water vapour also has important effects on the ionosphere of Mars (Sheel

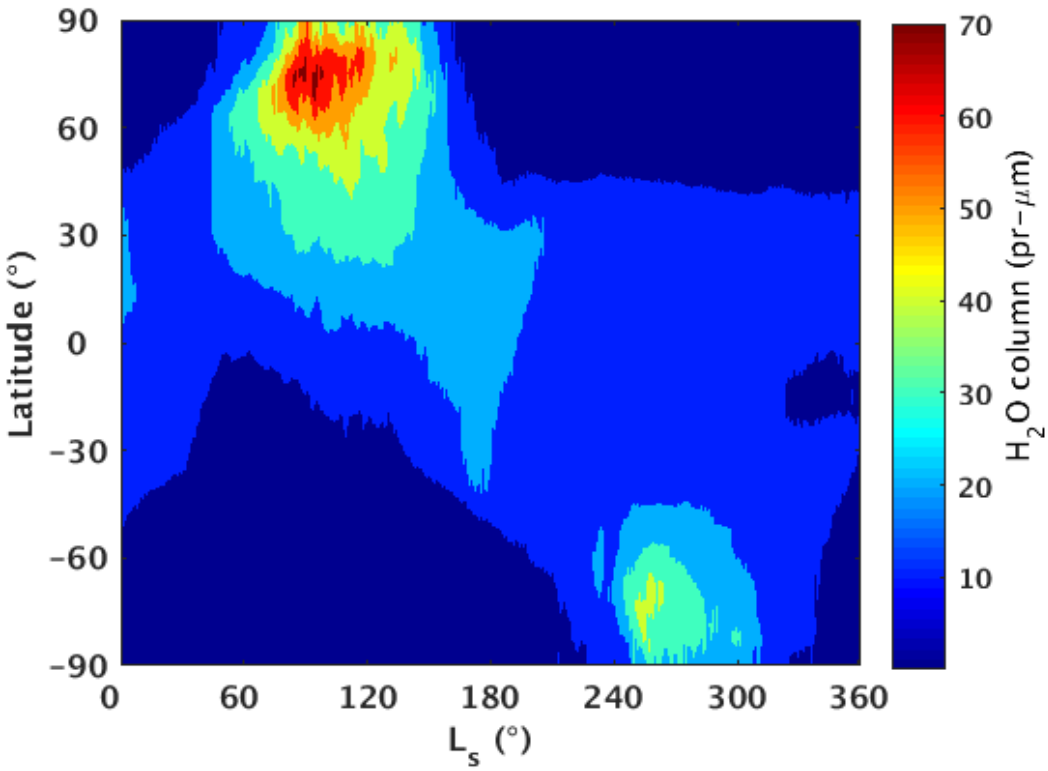

Figure 3.5: Water vapour columnar distribution (cm-amgot) as a function of latitude and season for MY 27

and Haider, 2012). In this section, we describe the columnar distribution of water vapour over the globe and its seasonal variation. Figure 3.5 shows the columnar water vapour distribution simulated by GCM. The water vapour abundance shows a maximum over northern polar region during mid-summer season. The columnar abundance is as high as

70 pr-µm which is little bit higher than those retrieved by the observations mentioned in section 3. In the northern polar region, the column values decreases below 1 pr-µm in the summer (Ls = 90°–180°). During winter, the abundance of water vapour is drastically reduced compared to its summer values. The columnar values reduce to ~ 10^{-2} pr-µm in the latitudes polewards of 60^oN. The observations are unable to measure the winter time water vapour in the polar region, due to the polar nights. Over the southern polar region, a maximum of 40 pr-µm is predicted by the GCM results during Ls = 250°-260° which is much higher than those observed by the spacecrafts. The minimum occurs during southern winter over the polar region. The winter time water vapour columnar values are smaller by a factor of 2-3 than those calculated over the northern polar region during northern winter. Over the northern equatorial and tropical regions water vapour abundance varies from 17 – 23 pr-µm. The SPICAM instrument onboard Mars Express measured water vapour column of about 12 pr-µm – 15 pr-µm at 40^oN during Ls = 120°. On the other hand, the TES instrument onboard MGS observed a water vapour column between 30 pr-µm and 35 pr-µm, while our GCM simulation yields an abundance of 35 pr-µm to 39 pr-µm. Our simulation shows a closer agreement with the observations by TES.

3.4.4 Ozone

Figure 3.6 shows the global and seasonal distribution of ozone. Our simulation produces seasonal variations in accordance with the previous observations and as expected from the modeling studies. In our simulations, ozone is found to be the highest in the northern polar region during mid-winter (Ls = 300°) when water vapour is almost absent. In this season, due to low temperature as shown in section 3, below 180 ^oK, water vapour freezes out of the atmosphere along with the CO_2 condensation. The nighttime observations are not possible from an orbiting spacecraft, but Holmes, (2018) has assimilated the ozone measurements from SPICAM, into the model, thereby predicting the ozone column in the polar nights. It has been seen from the assimilation studies, that polar night maximum over the northern hemisphere remains within 40 µm-atm (Holmes et al., 2018). However after the inclusion of heterogeneous chemistry in the photochemical module of LMD-GCM, the ozone amount has been calculated to increase (Lefevre et al.,

2008). The minimum ozone abundance from our GCM model run, is found in the southern polar region during southern winter, which is in accordance with the observations. The ozone abundance over the southern polar region during southern summer is below 1 µm-atm while that on the northern polar region during northern summer is between 1 – 2 µm-atm. Our current simulation captures the aphelion increase in the northern tropical and equatorial region, which is also seen in the SPICAM (Perrier et al., 2006) as well as MARCI (Clancy et al., 2016) observations. The ozone column, in this region, can increase up to 4-5 µm-atm during Ls = 60º – 80º.

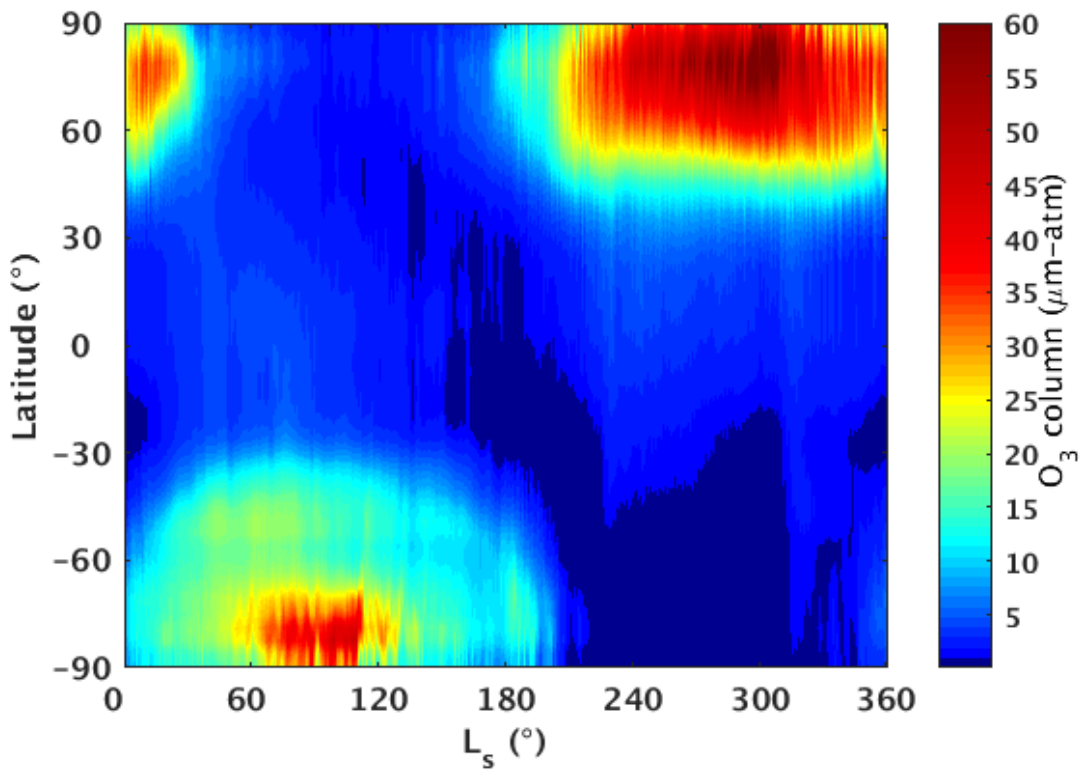

Figure 3.6: O_3 columnar distribution (µm-atm) as a function of latitude and season for MY 27.

3.5 Conclusion

In this chapter we have given an overview of the temperature distribution and composition of the Martian atmosphere based on various observations and models reported in the literature and from the photochemical-coupled-GCM simulations

performed for the current study. In the lower atmosphere, the temperature was found to vary over a wide range (120 ^{o}K – 280 ^{o}K) during a year. The general circulation model is able to reproduce the observed temperatures qualitatively, though the model cannot produce low temperatures observed in the mesosphere. As for the composition of the Martian atmosphere, the CO calculated by the model, matches well with the observational values. Ozone and water vapour simulated by the model yielded satisfactory results when compared to the observations discussed in this chapter. For the gaseous constituents such as N_2 and Ar, global observations are not available to compare with the model results. Thus, the model satisfactorily simulates the atmospheric temperature and important neutral constituents of the Martian atmosphere, which has been used in the work that will be presented in the upcoming chapters.

Chapter 4

Spatio-temporal variability of odd oxygen

Development of photochemical models along with observations has led to our present understanding of the Martian atmosphere (Read and Lewis, 2004). Modeling in one dimension and three dimensions and observations in a few cases, have provided a better knowledge of trace neutral species like odd oxygen family O_x (O and O_3), O_2, CO, H_2O, odd hydrogen family HO_x (H, OH, HO_2) and NO_x (NO and NO_2).

The primary driver of photochemistry of Mars is the photodissociation of the dominant CO_2. The end products CO and O_2 (which are the long lived species in Martian atmosphere) were overestimated by initial models of pure CO_2 chemistry. To solve this problem, models included odd hydrogen species HO_x which are mainly produced by water vapour (Parkinson and Hunten, 1972; Mc.Elroy and Donahue, 1972; Kong and McElroy, 1977). The oxidation of CO by OH radical leads to the regeneration of CO_2, which leads to better understanding of the long outstanding stability problem of Martian atmosphere. On the other hand, odd oxygen species O_x are important in producing OH radicals (Stock et al., 2012).

This chapter concentrates on the above important tracers, viz. odd oxygen species (O_x) and odd hydrogen species (HO_x), their role in the photochemistry of the Martian atmosphere and their interactions among themselves. We study the spatio-temporal variability of the competing reaction pathways that are important to odd oxygen chemistry. We do so with the help of the photochemistry coupled LMD-GCM described in Chapter 2.

Ozone possesses a special position in the chemical cycles of the Martian photochemistry as it is an efficient producer of $O(^1D)$. Ozone can also be studied as tracer of odd HO_x radicals as their direct observations are not available. Thus in this chapter, we also study the spatio-temporal variability of ozone based on observations and the GCM. The aim is to understand its variability and interaction with dust and effect of transport on the columnar ozone amount. Ozone columnar density and dust optical depth are retrieved from the radiance measurement obtained by SPICAM onboard MEX as discussed in Chapter 2. Ozone interacts with dust in a direct and indirect manner (Lefevre et al., 2004). The radiative effect of dust particles suspended in the atmosphere affect the atmospheric ozone (Lindner, 1988). Hence we discuss some aspects of the ozone-dust correlation in this chapter.

Therefore the objective of this chapter is twofold: (1) To understand the importance of competing loss pathways of odd oxygen and their inter-comparison for different seasons, latitudes, altitudes and time of the day and (2) To understand the spatio-temporal variability of ozone itself, interaction of ozone with dust particles and correlation of ozone with CO, based on observations and model.

4.1 Competing pathways in odd oxygen photochemsitry

Though the photochemistry of Mars is comparatively simple, the orbital properties of Mars and its exposure to solar influx lead to pronounced seasonal and latitudinal variations of short lived species (trace gases) such as O_x and HO_x. In previous studies, a quantitative comparison between various production and loss processes, with their relative importance in determining the abundance of these trace species, has not been performed. Here we use the photochemistry coupled LMD-GCM to study in detail the important source and sink processes of O_x and their contribution in different locations and seasons. This becomes especially important due to the high seasonal variability of water vapour involved in the photochemistry.

Members of the odd oxygen family O_x are produced from the photolysis of O_2 on Earth, which is not so abundant on Mars. On Mars production of O is through photolysis of CO_2 and O_2. 80% of the total O is produced by the photodissociation of CO_2 while O_2 photolysis represents less than 10% of the O_x production (Lefevre and Krasnopolsky, 2017).

$$CO_2 + h\nu \rightarrow CO + O, \lambda<205 \text{ nm} \quad (4.1)$$

$$O_2 + h\nu \rightarrow O+O, \lambda<242 \text{ nm} \quad (4.2)$$

Ozone is important species in Mars because it acts as a tracer of the odd hydrogen chemistry that stabilizes the CO_2-atmosphere of Mars. Important production and loss processes of O_x controlling the amount of ozone are discussed below. The only known production of ozone in any atmosphere occurs via the reaction $O+O_2+M \rightarrow O_3+M$, also known as Chapman mechanism, where M = CO_2 for the Martian atmosphere carries away the excess energy.

Various odd oxygen loss mechanisms have been proposed for the Martian atmosphere, which can be classified as loss with odd oxygen, loss with odd hydrogen and loss due to photodissociation. These mechanisms are listed below.

$$O+O+CO_2 \rightarrow O_2+CO_2, k = 8.0\times10^{-12}e^{-2060/T} \text{ cm}^{-3}\text{s}^{-1} \quad \text{(Tsang and Hampson,1986)} \quad (4.3)$$

$$O+O_3 \rightarrow O_2+O_2, k = 1.2\times10^{-10} \text{ cm}^{-3}\text{s}^{-1} \quad \text{(Sander et al., 2003)} \quad (4.4)$$

$$HO_2+O \rightarrow OH+O_2, k = 3.0\times10^{-11} e^{200/T} \text{ cm}^{-3}\text{s}^{-1} \quad \text{(Sander et al., 2003)} \quad (4.5)$$

$$OH+O \rightarrow H+O_2 , k = 2.2\times10^{-11} e^{120/T} \text{ cm}^{-3}\text{s}^{-1} \quad \text{(Sander et al., 2003)} \quad (4.6)$$

$$H+O_3 \rightarrow OH+O_2, k = 2.2\times10^{-10} e^{-470/T} \text{ cm}^{-3}\text{s}^{-1} \quad \text{(Sander et al., 2003)} \quad (4.7)$$

The photolysis of ozone occurs at all altitudes in less than 5 minutes, but is not a loss of odd oxygen, as it returns O or $O(^1D)$

$$O_3 + h\nu \rightarrow O+O_2, \lambda<320 \text{ nm} \quad (4.8)$$

$$O_3 + h\nu \rightarrow O(^1D)+O_2, \lambda<305 \text{ nm} \quad (4.9)$$

The $O(^1D)$ produced is rapidly quenched by CO_2 by the following reaction

$$O(^1D)+CO_2 \rightarrow O+CO_2,\ k = 7.4\times10^{-11}\ e^{120/T}\ cm^{-3}s^{-1} \qquad \text{(Sander et al., 2003)} \quad (4.10)$$

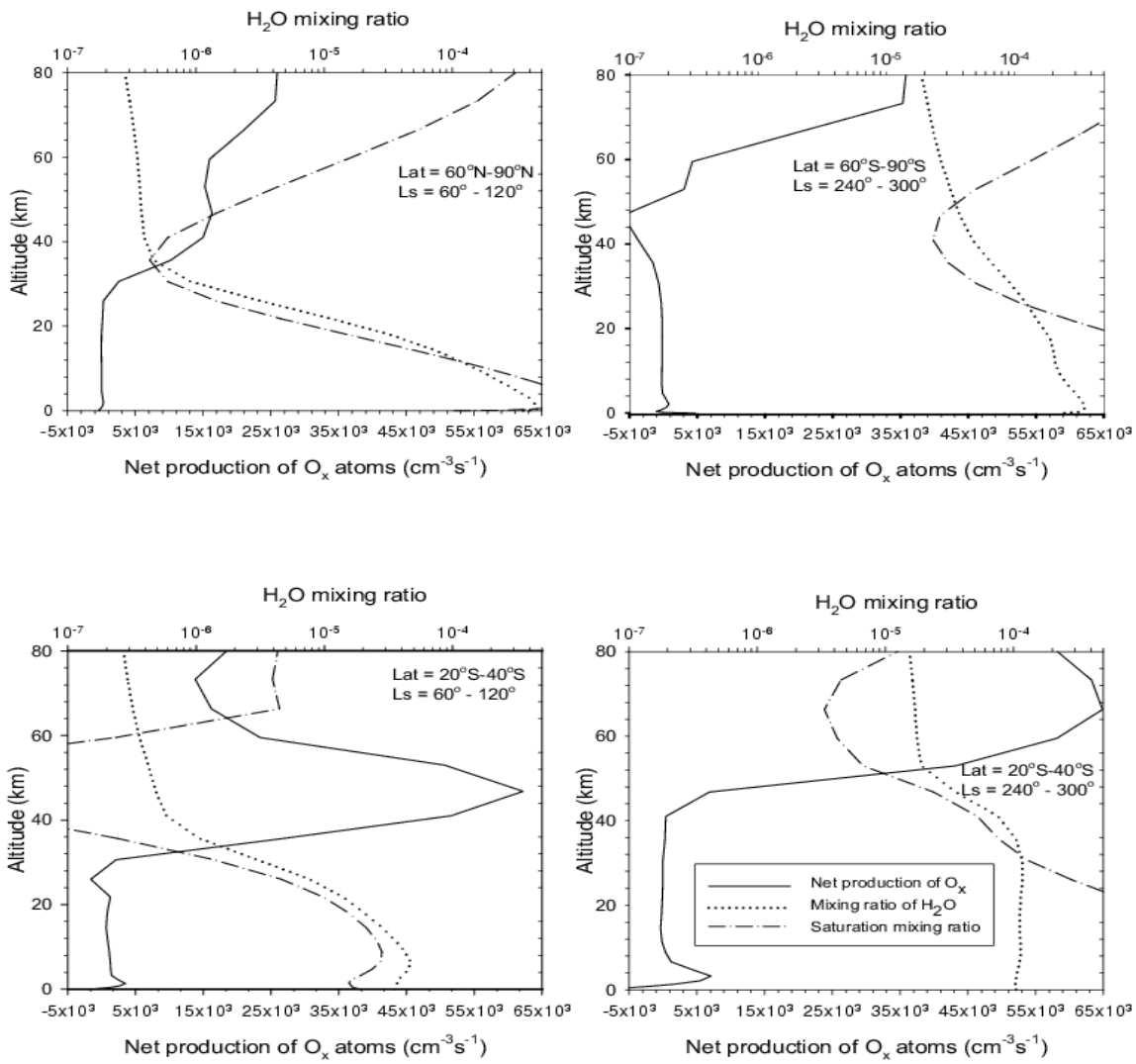

Figure4.1: Vertical profiles of net O_x production, water vapour mixing ratios, and water vapour saturation values. The net production has been obtained by considering each production and loss process of O_x species. Each panel of the figure shows values averaged over the specified latitude region and season.

Thus reactions of exchange between O, $O(^1D)$ and O_3 are fast so that each species is in equilibrium with the O_x family in daytime. O_3 is the dominant species in the O_x family up to 25 km, the concentrations of O_3 being 50–100 times those of O near the surface

(Lefevre and Krasnopolsky, 2017), and is therefore directly measurable by remote sensing due to its strong absorption in UV (255 nm).Unlike in the Earth's atmosphere, there is no stratosphere in Mars due to comparatively low concentration of ozone. This shows lower heating through the absorption of UV energy in the atmosphere of Mars in comparison to Earth's atmosphere.

In this section, we discuss the altitudinal and seasonal variability of the production and loss mechanisms of odd oxygen discussed above, for three latitude regions: 60°N–90°N, 60°S–90°S, and 20°S–40°S, zonally averaged over these latitude regions. To understand the effect on these variations of water vapour and hygropause (altitude at which water vapour saturation occurs), we look at profiles of water vapour and the net production rate (production-loss) of odd oxygen (Figure 4.1). Figure 4.1 also includes the water vapour saturation mixing ratios. We define the perihelion season (Ls=240°–300°) as the season around the perihelion (when Mars is closest to the Sun ~ Ls=251°) which corresponds to southern summer (or northern winter). Similarly the aphelion season (Ls=60°–120°) is defined as the season around aphelion (when Mars is furthest from Sun ~ Ls=71°). As can be seen from Figure 4.1, odd oxygen is strongly anti-correlated to water vapour and the hygropuase varies with season and location. The effect of this will be seen on the variability of production and loss mechanisms to be discussed in the following sub-sections.

4.1.1 Seasonal variation in production and loss rates of odd oxygen

The production and loss mechanisms described in Equations (4.1–4.7) have different contributions to odd oxygen depending on the time of the day. We consider two cases of either daytime averaged values (SZA < 70°) or nighttime averaged values (SZA > 96°). These chemical mechanisms to be discussed subsequently depend on the abundances of the reactants O, O_3, HO_2, OH, and H. These are shown in Figure 4.2 for the three latitude regions selected, for the aphelion and perihelion seasons and for daytime and nighttime.

The loss processes of O_x are shown in Figures 4.3 to 4.8. The 60°N–90°N latitude region during the season L_s= 205°–336° does not receive much sunlight, due to which

there are no model results for SZA < 70° (white regions in Figure 4.3). Similar conditions lead to missing data for Figures 4.4, 4.5 and 4.6.

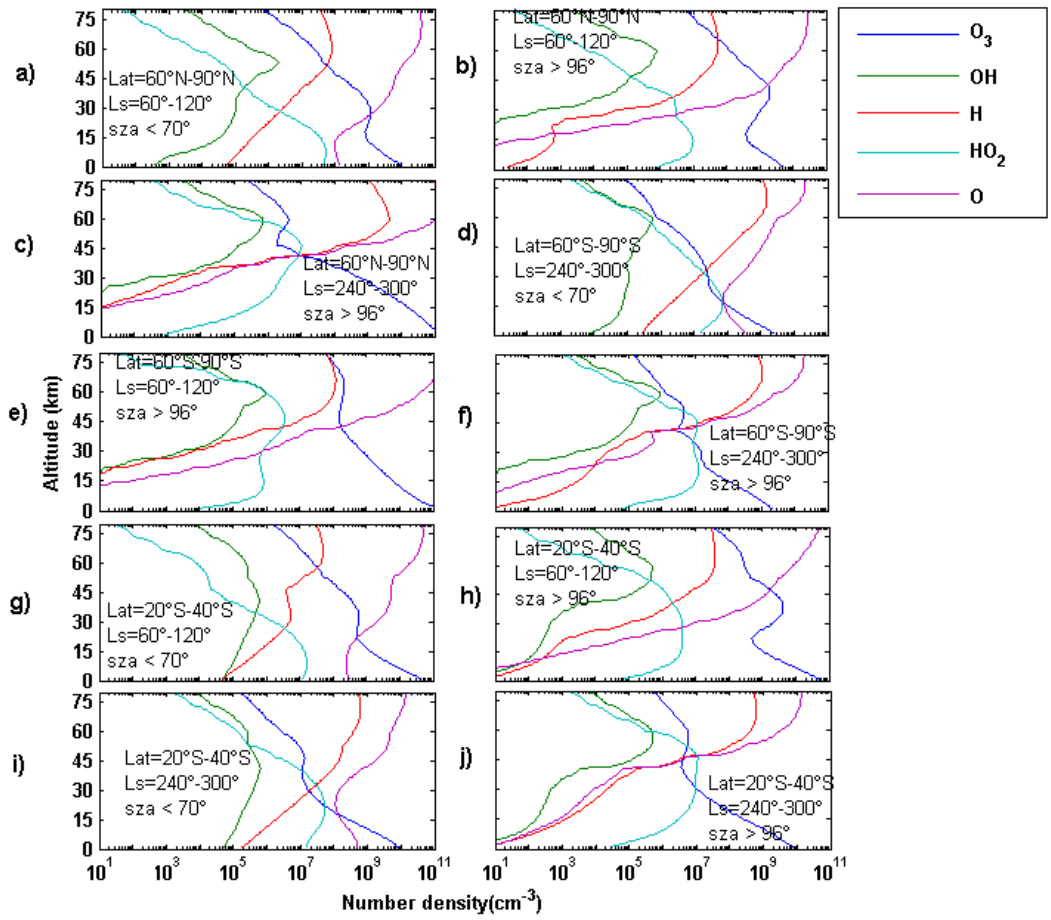

Figure 4.2: Vertical number density profiles of O, O_3, HO_2, OH, and H for the three latitude regions (60°N–90°N, 60°S–90°S and 20°S–40°S), for the aphelion and perihelion seasons and for daytime and nighttime.

Figure 4.3 describes the seasonal variation of chemical processes during day over the 60°N–90°N latitude region. The loss rate of O atoms due to O–O recombination is shown in Figure 4.3a. High loss rates ~ 10^4–10^5 $cm^{-3}s^{-1}$ are observed in the altitudes between 60 and 75 km all year round. This is due to increase of O atom concentrations by orders of magnitude above 60 km compared to the surface (Krasnopolsky 1995: Figure 4.2), related to increase in its photochemical lifetime (Lefevre and Krasnopolsky, 2017) compared to lower altitudes. The low loss rates (~few tens $cm^{-3}s^{-1}$), for a few altitudes or season is due

to high water vapour. During Ls=60º–180º a peak in O–O recombination rate occurs between 30 and 45 km, as water vapour decreases abruptly above the hygropause (Figure 4.1).

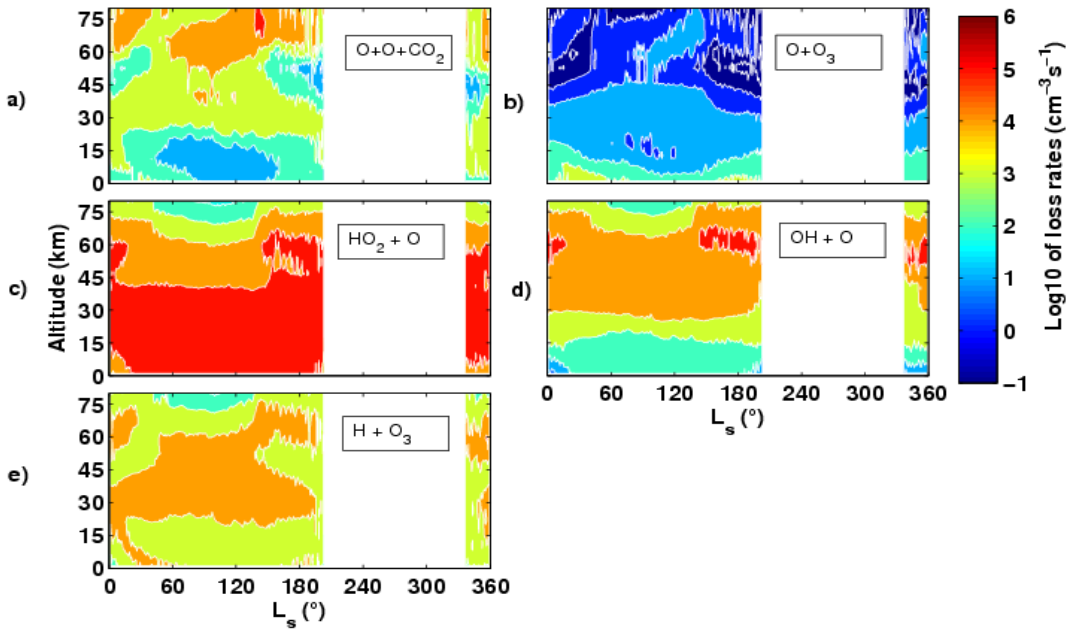

Figure 4.3: Seasonal variation of the daytime loss rates of O_x due to the reactions of Equations 4.3 to 4.7, over latitude region 60ºN–90ºN.

Figure 4.4a shows the vertical variation in the nocturnal O–O recombination rate. The rates are very low at lower altitudes and increase above ~30 km for aphelion and ~45 km for perihelion seasons. The transition heights are different due to change in hygropause altitude for the two seasons (Figure 4.1). The reaction rates are low at lower heights because in nighttime, there is not much production of O atoms and on top of that most of it is converted to O_3 rapidly (Figure 4.2). This feature can be seen for other loss processes and regions in nighttime (Figure 4).The loss mechanism of O and O_3 by reacting with each other (Eq. 4.4) is shown in Figures 4.3b (daytime) and 4.4b (nighttime) for the region 60ºN–90ºN. The loss rates are high (> 10^2 $cm^{-3}s^{-1}$) near the surface, and then decrease above 10-15 km, as O_3 is high near the surface compared to higher altitudes (Figure 2). Figure 4.3c shows the loss of O_x in daytime due to HO_2 over 60ºN–90ºN region. The

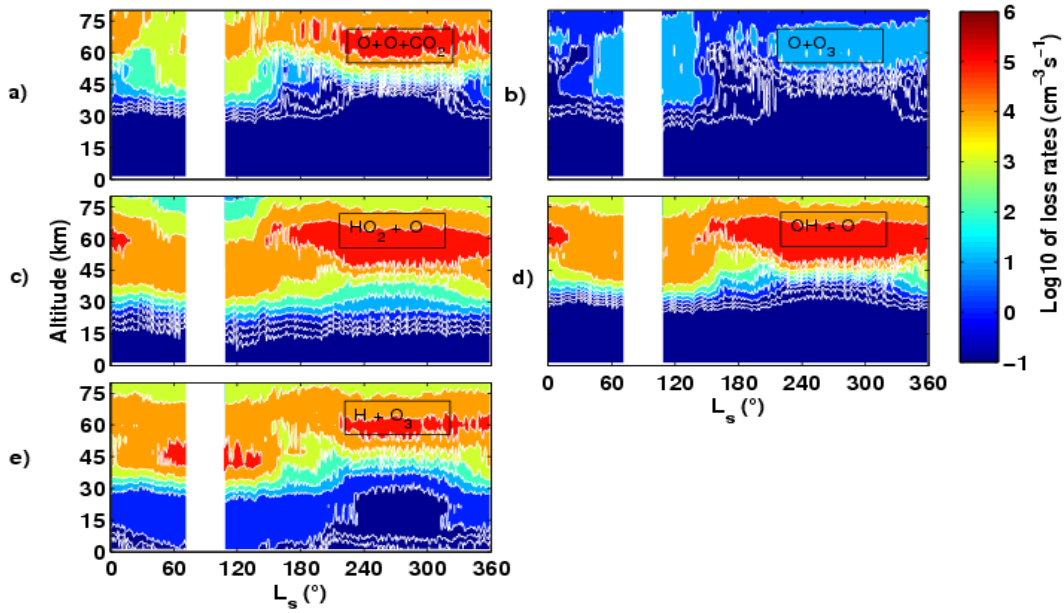

Figure 4.4: Seasonal variation of the nighttime loss rates of O_x due to the reactions of Equations 4.3 to 4.7, over latitude region 60ºN–90ºN.

reaction rates are high at lower altitudes (~ 10^5 $cm^{-3}s^{-1}$) due to high concentration of HO_2 and O (Figure 4.2), and do not show significant seasonal variability. The rates start decreasing above ~45 km for the season Ls=60º–120º, and above 60 km for seasons with Ls > 180º due to change in hygropuase level (Clancy et al., 1996). During nighttime this loss rate is quite high in the region 45-60 km (Figure 4c) as HO_2 is high during perihelion (Figure 4.2).

Figure 4.3d describes the loss of O due to OH. OH radicals which is a direct product of the photolysis of H_2O, plays important role in destroying O atoms in Mars. Due to less abundance of OH below 30 km (lifetime below 30 km < 1 sec (González-Galindo et al., 2005), the loss due to OH is less important in the lower altitudes. However for higher altitudes where lifetime of OH increases, this loss rate increases up to 10^5 $cm^{-3}s^{-1}$. During nighttime this loss rate is quite high in the region 45-60 km (Figure 4.4d) as OH is high during perihelion (Figure 4.2). Figure 4.3e shows the loss of ozone due to hydrogen atom

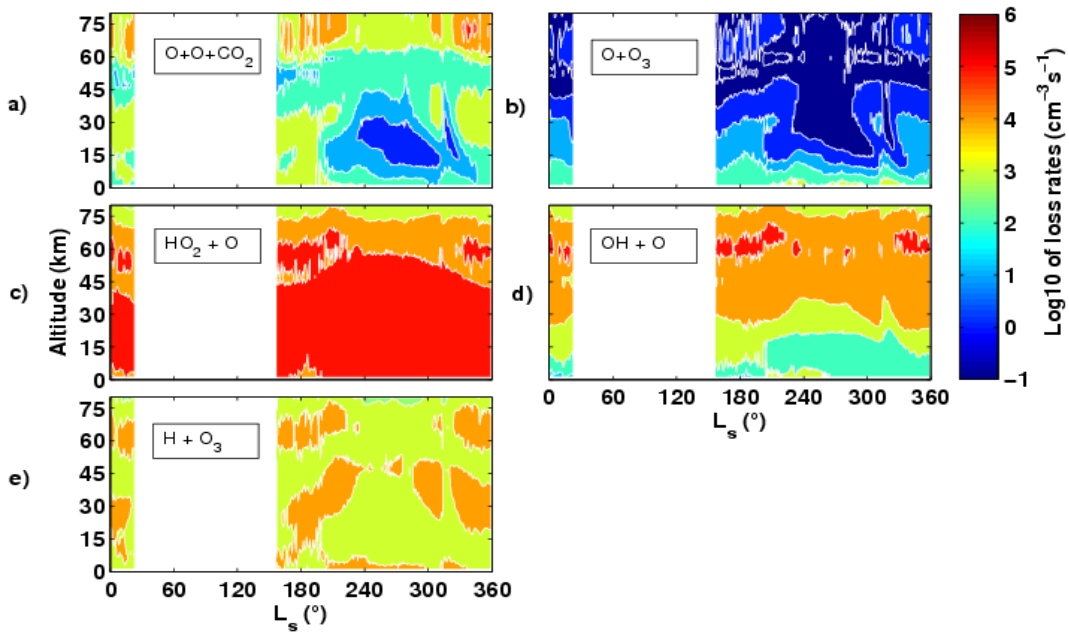

Figure 4.5: Seasonal variation of the daytime loss rates of O_x due to the reactions of Equations 4.3 to 4.7, over latitude region 60°S–90°S.

H (Eq. 4.7), in daytimes. During the aphelion season maximum loss rates (10^4–10^5 $cm^{-3}s^{-1}$) are found in the region 30-60 km, as density of H atoms increases with altitude (Figure 4.2). In nighttime (Figure 4.4e) high values of O_3 loss due to H (~ 10^5 $cm^{-3}s^{-1}$) occur around 45 km during the aphelion season as O_3 densities are high (Figure 4.2). This loss rate is also high during the perihelion season (~ 10^5 – $10^6 cm^{-3}s^{-1}$) in the region 45-65 km due to large densities of H atoms (Figure 4.2).

Figure 4.5 and Figure 4.6 show the seasonal variation in the loss rate of odd oxygen for 60°S-90°S during day and night respectively. The loss due to O–O recombination is significant above 60 km for daytime and nighttime due to reasons discussed for 60°N–90°N. Over the southern polar region, the loss of O atoms due to HO_2 shows a similar trend to that of 60°N-90°N. The loss due to OH is highest during aphelion in nighttime, when the loss of ozone due to hydrogen atoms is also highest in the region 45–75 km.

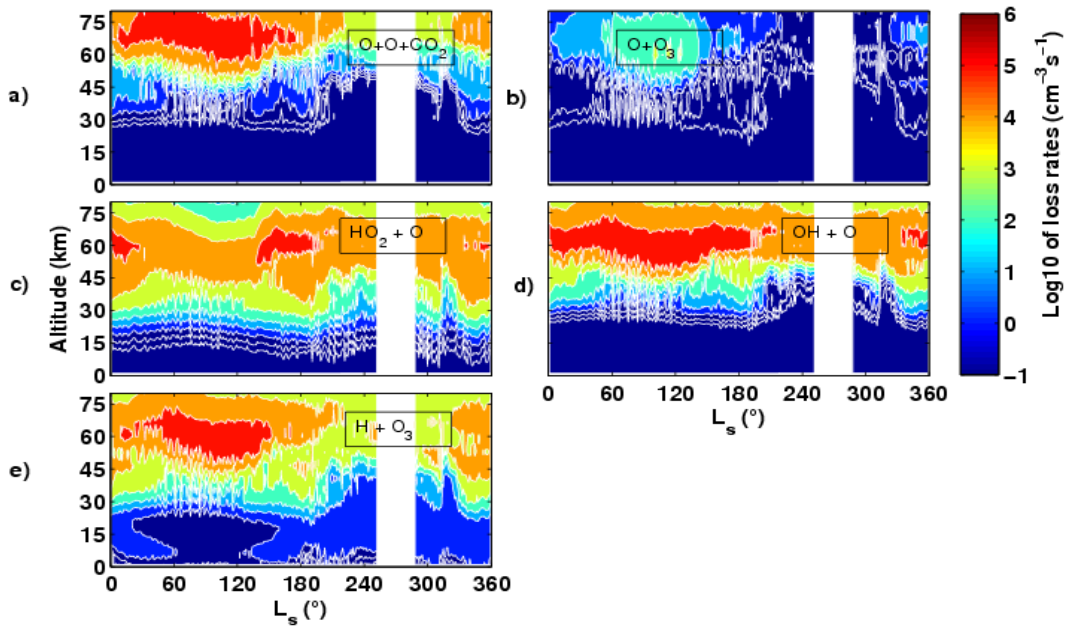

Figure 4.6: Seasonal variation of the daytime loss rates of Ox due to the reactions of Equations 4.3 to 4.7, over latitude region 60°S–90°S.

Figures 4.7 and 4.8 show the seasonal variability of odd oxygen loss rates over 20°S–40°S. During daytime, the loss due O–O recombination peaks in the altitude region 35–50 km due to anti-correlation of odd oxygen with water vapour. The O–O recombination rates increase above 30 km for aphelion season and above 50 km for perihelion season, due to difference in hygropause levels for the two seasons (Figure 4.1). This feature can also be seen for other nighttime loss processes (Figures 4.8a-e).

In daytime, the $O+O_3$ loss rates in the region 15-45 km, are higher in aphelion season by an order of magnitude compared to perihelion season, due to decrease in water vapour in aphelion season when the atmosphere is colder than perihelion season. The loss of O due to OH for daytime, during the aphelion season, increases by an order of magnitude above 35 km due to higher abundance of OH at higher altitudes. The loss of ozone by H atoms peaks in the region 20-45 km during aphelion season due to the second peak of ozone (Figure 4.2).

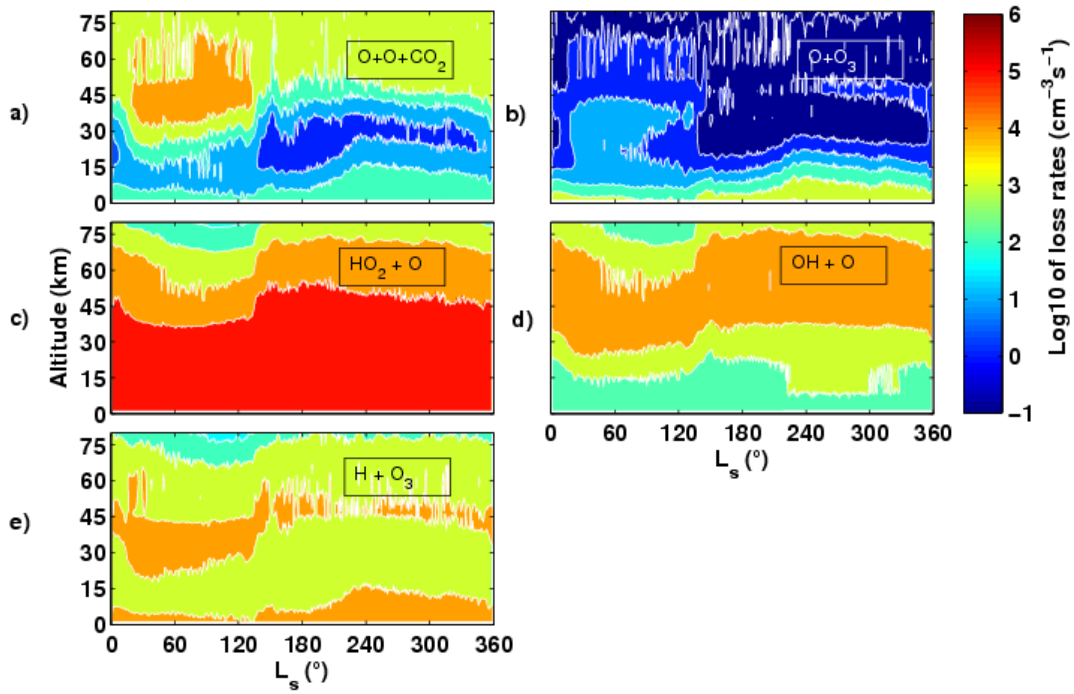

Figure 4.7: Seasonal variation of the daytime loss rates of Ox due to the reactions of Equations 4.3 to 4.7, over latitude region 20°S–40°S.

Based on the discussions above we note some differences/similarities between the different latitudes in terms of their seasonal, diurnal, and altitude variability. Looking at the perihelion season, at higher altitudes, water vapour is higher over southern polar region (60°S–90°S) compared to southern latitudes 20°S–40°S, with consequently an opposite trend for O atoms (Figure 4.1). As a result, the recombination rate between oxygen atoms becomes significant only above 60 km for latitudes 60°S–90°S whereas over latitudes 20°S–40°S, the loss rate increases above 45 km. A similar trend is seen for the loss rate of O due to HO_2, which is comparable below 40 km over these two regions. The nighttime loss rates over these two regions during perihelion are also comparable.

In the aphelion season, daytime loss of O due to HO_2 does not vary significantly with latitude and seasons. O–O recombination shows a higher peak in 35–45 km for 20°S–40°S compared to 60°N–90°N, due to a steeper increase rate in O_x production (Figure 4.1). For nighttime, O+O and O+O_3 loss rates are maximum above 60 km for all latitudes, with

higher values for southern polar region. Nighttime peak of $H+O_3$ loss rates is higher in altitudes for 60°S–90°S compared to other latitudes.

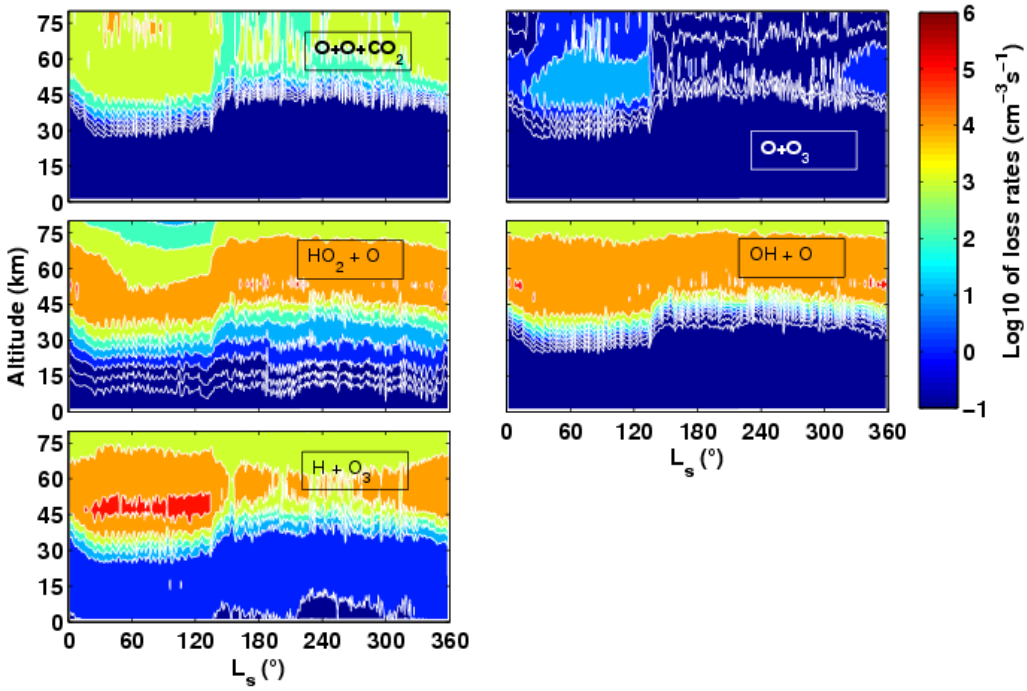

Figure 4.8: Seasonal variation of the nighttime loss rates of Ox due to the reactions of Equations 4.3 to 4.7, over latitude region 20°S–40°S.

4.1.2 Comparison among the production and loss rates

As discussed in section 4.1.1, in particular two seasons Ls=60°–120° (aphelion) and Ls=240°–300° (perihelion) show features of loss mechanisms, that are different than other seasons. In this section we concentrate on these two seasons and the three latitude regions, to study the altitude variations of the relative importance of various pathways. Figure 4.9 shows vertical profiles of the production and loss processes of O_x averaged during two seasons Ls=60°–120° and Ls=240°–300°. In each of the latitude regions (60°S–90°S, 60°N–90°N and 20°S–40°S), the production and loss rates are averaged, considering volume weights over grid cells. Column integrated production and loss rates for various latitudes and seasons are presented in Table 4.1. We also calculate the quantitative contribution of each loss process to the total loss of odd oxygen. For this we consider a

few altitude regions where the trends are similar. For each altitude region, we find the percentage contribution of the columnar loss rate for a particular process, to the total columnar loss rate (sum of all loss processes). The results are shown in Table 4.2.

Northern polar region summer day

We consider here chemical pathways in the daytime for the northern polar region (60°N to 90°N), where availability of water vapour is high in the aphelion season. Figure 4.9a shows the contributions of the competing loss and production processes for the O_x species in the Martian atmosphere. The production rate due to CO_2 photolysis and the loss rate of O atoms due to HO_2 are comparable below 30 km, where this loss rate contributes 94-98% to the total loss of odd oxygen (Table 2). Above 30 km, the production rate remains almost constant while there is a sharp decrease in the loss rate of O by HO_2. The loss rate values are in the order of $10^5 cm^{-3}s^{-1}$near the surface but above 60 km, it decreases rapidly from 10^4 to few hundreds $cm^{-3}s^{-1}$, contributing 11% to the total loss (Table 2) which is comparable to the loss due to hydrogen atom H (13%). The O-O recombination loss dominates above 60 km (54%).

Below 30 km, the next significant process is the loss of ozone due to hydrogen atom H, which is about ~ $8x10^3$ $cm^{-3}s^{-1}$ near the surface though it contributes only 1-4% to the total loss below 30 km (Table 2) . Among the other processes, the loss due to reaction (O+OH) contributes less that 2% to the total loss below 30 km but dominates between 45-60 km and is comparable to ($O+HO_2$) contributing 37% to the total loss (Table 2).

Northern polar region summer night

The nighttime loss processes for the same region and season discussed in section 4.2.1, are described in Figure 4.9b. During night, O atoms are scarce below 30 km over this region for the aphelion season (Figure 4.2b), therefore the reactions involving O are insignificant below 30 km (<0.1%) except (HO_2+O) which contributes 84% (due to high density of HO_2 as can be seen in Figure 4.2b). The loss of ozone due to hydrogen atoms is the next significant loss below 30 km (16%). Between 30-60 km the loss rates due to OH and HO_2 are comparable (~25%) and the loss due to H dominates (46% of the total

loss). The loss due to ($O+O_3$) is the insignificant at all heights. The loss rate due to (O+O) becomes significant only above 60 km (20% of total loss).

Northern polar region winter night

Figure 4.9c shows the comparison among the chemical processes during the perihelion season over 60ºN–90ºN. During this season, water vapour is less abundant due to condensation over the polar caps. During the winter nights over northern polar region, the loss rates are very low below 30 km. The loss processes of O_x due to the derivatives of water vapour photolysis (OH and HO_2) are comparable in the region 30-60 km (40-46%). The peak value due to loss of O by HO_2 is six times greater than that during northern polar summer nights. For the loss of O_3 due to hydrogen atoms H, the peak value is one order higher. During night, while the O–O recombination rate is insignificant below 60 km, it becomes one of the most significant above 60 km (33%) along with OH+O.

Southern polar region summer day

Over the southern polar region (60ºS–90ºS) during the perihelion season, the vertical variation of the loss and production processes of O_x for daytime are shown in Figure 4.9d. The production rate remains almost similar to that of over northern polar region summer. The loss rate due to HO_2 overlaps the production rate (due to photolysis of CO_2) below 45 km (being the most dominant: 90-98%), while for northern polar summer (Figure 4.9a), the corresponding altitude is 30 km. The loss of rate O due OH increases and becomes significant above 40 km (34%), where the dominant loss due to HO_2 contributes 62%. The loss of O_3 due to hydrogen atoms H is the next important loss after the loss by HO_2 and OH, but contribution remains low at all altitudes. The O–O recombination rate and the loss rate due to the ($O+O_3$) are insignificant, though the O–O recombination has a small contribution above 60 km.

Southern polar region summer night

We now discuss the nighttime pathways for the southern polar region for perihelion season which are shown in Figure 4.9e.The contribution of the loss due to OH increases

above 30 km to 38%, while that of HO_2 decreases to 14% (from 82% below 30 km). Below 30 km, the loss of ozone due to hydrogen atoms H is the second important loss of O_x species (17%), while in the region 30–60 km it becomes the most dominant process comparable to loss due to H (38%).The loss of ozone due to O is insignificant at all heights.

Southern polar region winter night

The vertical profiles of the production and loss processes of O_x over the southern polar region night during perihelion season are plotted in the Figure 4.9f. In this season, the loss rates due to (HO_2+O) is the most dominant below 30 km (85%) followed by the loss of O_3 due to hydrogen atoms H (15%) and contribution of both decrease with altitude . The contribution of the loss processes due to OH increases with altitude. The losses of O due to O–O recombination and (O+O_3) are insignificant.

Southern hemispheric day

Over the region 20ºS–40ºS, the daytime loss and production processes are shown in Figures 4.9g and 9i for the aphelion and perihelion seasons respectively. As can be seen from Figure 4.9g, the loss due HO_2 is comparable with the production rate up to 30 km where this loss rate has the largest contribution (94–98%), while above 30 km it decreases rapidly to values lower than the production rate (Figure 4.9g). Contrary to that, the loss process remains comparable to the production rate up to a higher altitude 45 km during the perihelion season (Figure 4.9i). This is due to change in the hygropause (Figure 4.1). The next significant loss process is the loss of O due to OH in the altitudes above 40 km (18–29%). The O–O recombination is significant only above 45 km, becoming the most dominant loss (34-73%). The loss of ozone due to H is the next most effective losses of O_x near the surface after (O+ HO_2), as it has values ~ $6x10^3$–$1.3x10^4$ $cm^{-3}s^{-1}$below 10 km. The loss rate shows a peak ($2x10^4$ $cm^{-3}s^{-1}$) at 30 km.

During the perihelion season (Figure 4.9i), the loss of O due to OH increases two to three times near the surface compared to aphelion season, and the peak is also larger ($9x10^4$ $cm^{-3}s^{-1}$) at a higher altitude (~45 km). This loss rate is the next significant loss after

the loss due to HO_2 above 30 km (6–50%), followed by loss due to H (2–5%) and then O–O recombination. The loss rate of ozone with O remains insignificant.

Southern hemispheric night

The nighttime losses for the southern hemispheric region are shown in Figures 4.9h and 4.9j. Figure 4.9h shows the vertical variation during the aphelion season, when the nighttime losses have significant values above 30 km. The three loss rates due to HO_2, H, and OH contribute to the total loss by 69%, 29%, and 1% in these altitudes up to 60 km, above which loss by HO_2 is insignificant and loss by O–O recombination takes over. During the perihelion season (Figure 4.9j) the loss due to H has a higher contribution below 30 km (48%) where loss due to OH has a higher contribution (35%) between 30–60 km. Also above 60 km, the O–O recombination rate has a lower contribution during perihelion (3%) than during aphelion (24%).

4.1.3 Comparison with one dimensional models

1D globally averaged photochemical models of the Martian atmosphere have been used to study vertical profiles of trace species and reaction rates. One such model by Nair et al. (1994) discussed the loss rates for oxygen atoms. They consider a case of high water vapour (H_2O ~ 8.8 pr µm). In our study this corresponds to approximately the water vapour for perihelion at southern tropical latitudes (20°S–40°S), i.e H_2O ~ 6 pr µm (Figure 4.9i). In fact for both cases, the surface volume mixing ratio of water vapour is ~ 10^{-4}, and the water vapour profile is similar. Surface temperatures are also similar (210 °K). We compare our reaction rates with those of Nair et al. (1994) for the case of eddy diffusion coefficient, $K=10^5$ cm^2sec^{-1}. For the loss of oxygen atoms (O) by HO_2, the surface reaction rate reported by Nair et al. (1994) ~ $2x10^5$ $cm^{-3}s^{-1}$ is lower than in our work ~ $4x10^5$ cm^{-3} s^{-1} (Fig. 9i). At an altitude of 70 km, this rate is ~ $3x10^3$ $cm^{-3}s^{-1}$ for Nair et al. (1994) compared to our value of ~ $9x10^3$ $cm^{-3}s^{-1}$. Thus overall, their rates for loss of O with HO_2 are lower than ours. This is because their volume mixing ratios of O are lower than ours, when we compare vertical profiles (~10^8 cm^{-3} vs. $8x10^8$ cm^{-3} near the surface), most probably due to lesser production from photolysis of CO_2. The loss rates for (O+OH)

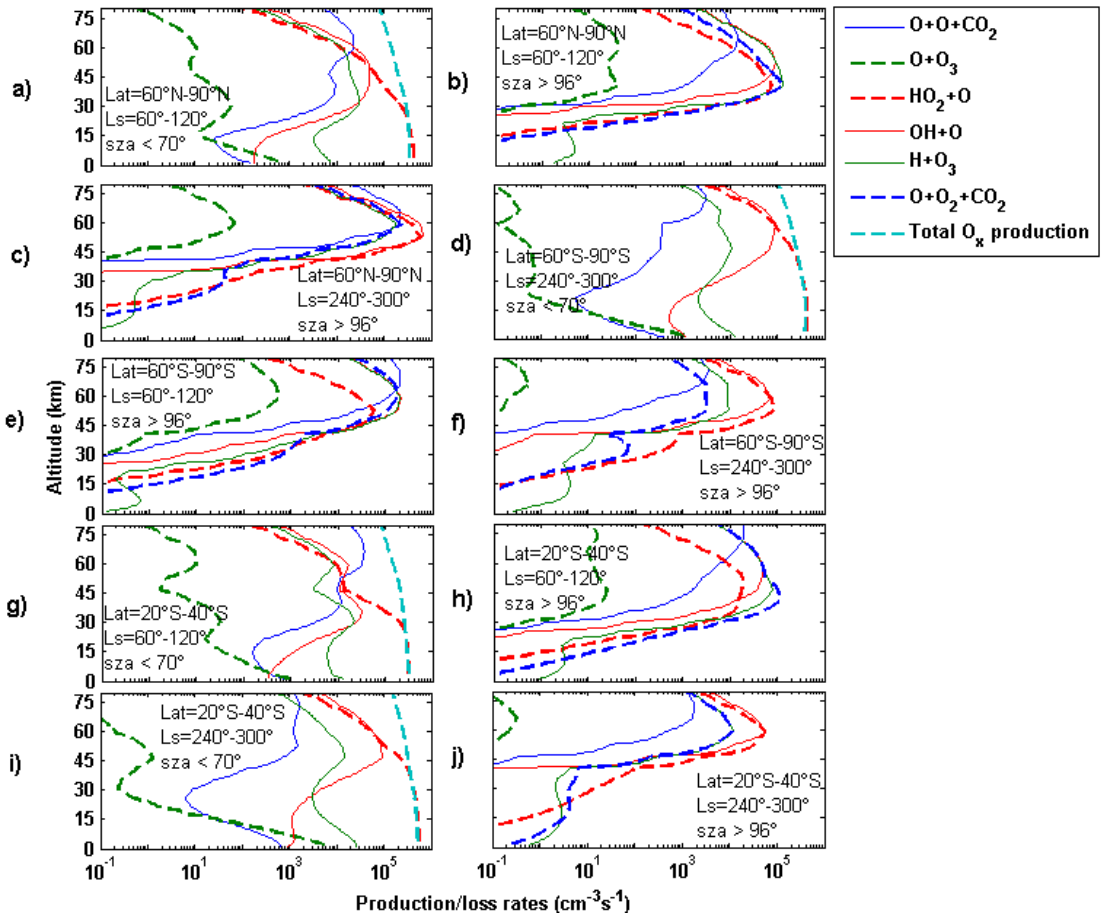

Figure 4.9: Comparison among the loss rates of O_x during the aphelion season (Ls=60°–120°) and the perihelion season (Ls = 240°–300°) over the latitude region 60°N–90°N, 60°S–90°S and 20°S–40°S. Panels with Solar Zenith Angles (SZA) < 70° correspond.

reported by Nair et al. (1994) is quite similar to those in our study with surface values of 10^3 cm^{-3} s^{-1} for both the studies, while the peak altitudes differ – 65 km and 50 km respectively. The surface loss rates of $O+O_3$ are much lower for Nair et al. (1994) (300 $cm^{-3}s^{-1}$) compared to ours (10^4 $cm^{-3}s^{-1}$), but are similar to our study between 40-60 km. As for the O+O recombination rates, these differ substantially in the nature of the profile as well as the surface values of Nair et al. (1994) are much lower than ours (20 $cm^{-3}s^{-1}$ vs. 10^3 $cm^{-3}s^{-1}$).

Another study using a 1D model for the Martian photochemistry (Krasnopolsky, 1995) reports the reaction rates of the loss process (O+H). The loss rates are $6x10^4$

between 45–50 km and 10^2 at 15 km. This is again similar to our Figure 4.9i, where the rates are 10^5 at 45 km and 10^3 at 15 km, though our rates are higher. The surface water vapour mixing ratio is again ~ 10^{-4} for both cases.

As discussed in previous sections the loss rates reported in this study, vary with latitudes and season – a feature that cannot be simulated by 1D models which do not capture the nighttime results as well. The loss rates discussed here result from a more realistic temperature structure and water vapour cycle, that a 1D model cannot account for (for example water vapour getting trapped in the polar caps over high latitudes). One fundamental advantage of a three dimensional model is that it can represent the effect of three dimensional transport on tracer distribution. However, the effect of transport will be studied in the below section where we concentrate on the atmospheric factors such as suspended dust and atmospheric transport affecting odd oxygen. For this purpose, we use our retrieved ozone and dust values from SPICAM.

4.2 Ozone and dust from observations and comparison with model

Unfortunately, observations for all the member of odd oxygen are not available for global study which bound us to study only ozone and its variation due to transport and dust. The ozone and dust optical depths retrieved from SPICAM observations (see Chapter 2) are used to study their dependence. Longitudinally averaged columnar values of ozone retrieved from SPICAM for MY 27 are shown as a function of latitude and season (Solar Longitude, Ls) in Figure 4.10. For the current retrieval, the highest ozone columnar values are within 25µm-atm over northern polar region during spring and winter. The ozone retrieved for this work matches well with those retrieved by Willame et al. (2017) and Clancy et al. (2016), who have reported similar maximum values. However, Perrier et al. (2006) reported high columnar ozone amounts of about 40µm-atm. The seasonal and regional features of ozone column can be seen in Figure 4.10. In the Martian atmosphere ozone is anti-correlated with the water vapour (Lefevre et al., 2004; Nair et al., 1994; Krasnopolsky, 1993), since ozone is destroyed by the odd H radicals produced from water

vapour. This results in higher column values for ozone during winter and almost negligible values during summer. During winter, water vapour condenses on the poles leading to less loss of ozone and thus high column amounts. Over the high northern latitudes in spring, high ozone values in the range 12–21µm-atm are retrieved. During the polar winter nights observations are not available. During summer around Ls = 120°, ozone values are of the order of 1µm-atm while they increase at the end of summer to 5 µm-atm. During the southern summer columnar values of ozone are less than 0.1µm-atm, which is a direct effect of increased hygropause elevation.

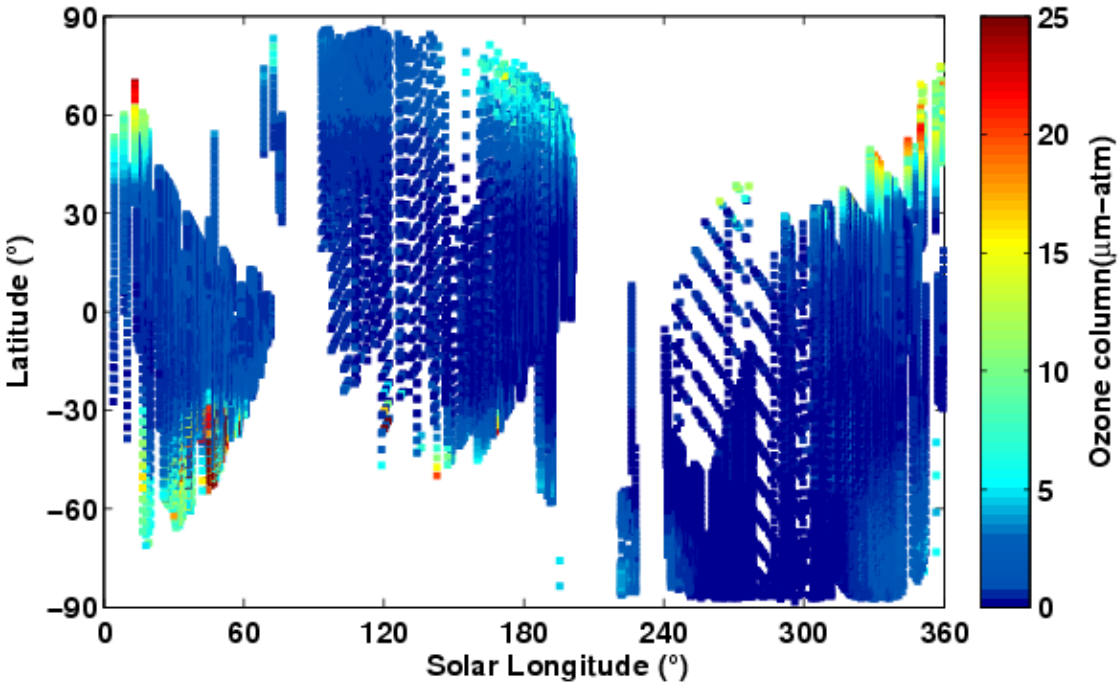

Figure 4.10: Ozone columnar values retrieved from SPICAM for MY 27 as a function of latitude and season.

4.2.1 Comparison of observed ozone with GCM simulations

The ozone data retrieved and discussed above, are averaged over Latitude intervals of 30° and Solar Longitude (Ls) intervals of 2° and its comparison with simulations from the LMD-GCM is shown in Figure 4.11 for MY 27 and MY 28 and for the six latitude regions: tropical (0 to ±30), mid (±30 to ±60) and high (±60 to ±90) latitudes. Certain features are clearly visible in the GCM simulated ozone variability. Firstly, maximum

ozone columns (~ 20µm-atm) are seen at high latitudes and polar region in southern

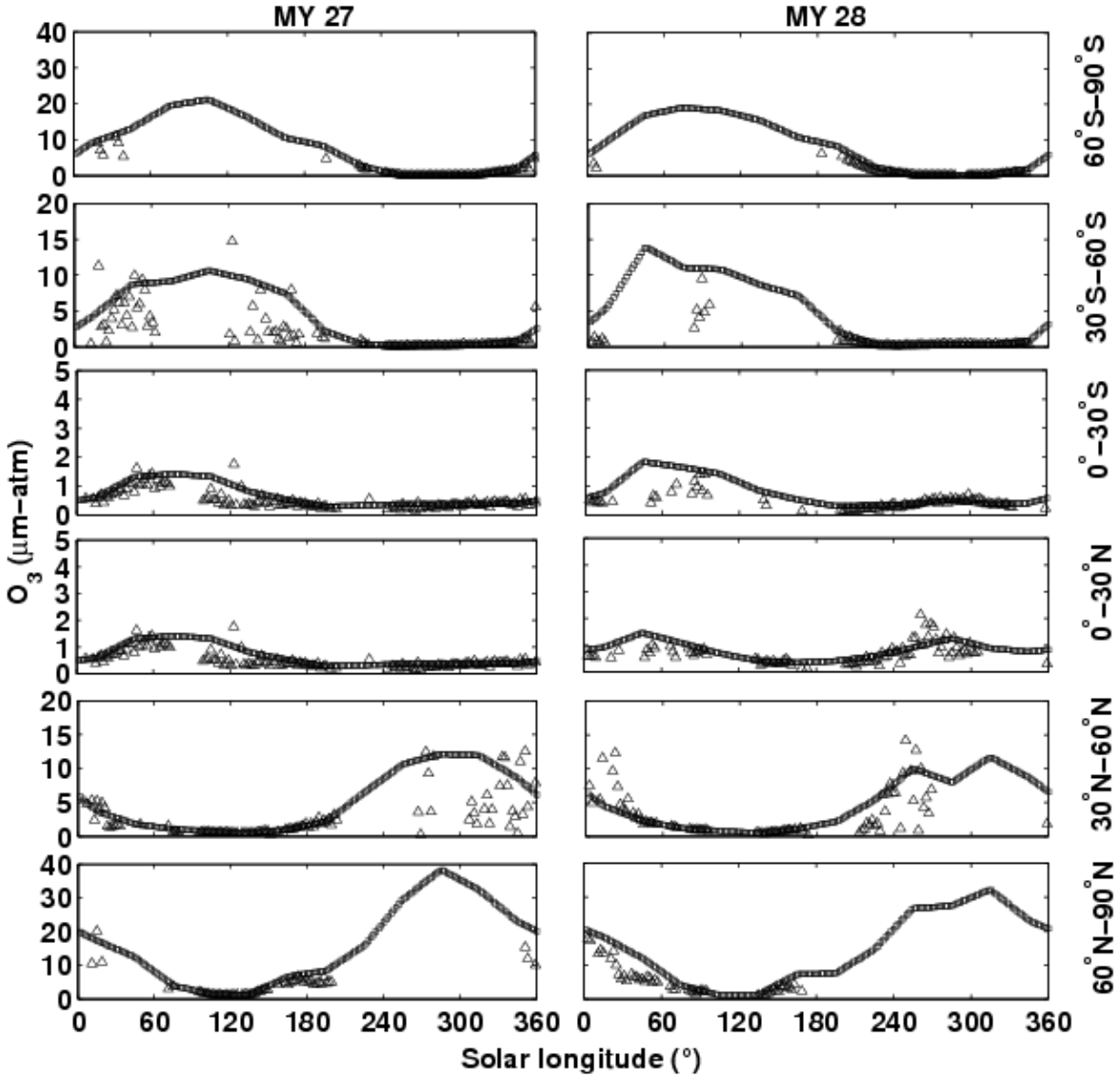

Figure 4.11: Zonally averaged ozone retrieved from SPICAM and its comparison with simulations from the LMD-GCM for MY 27 and MY 28, averaged over the six latitude regions: tropical (0 to ±30), mid (±30 to ±60) and high (±60 to ±90) .

fall/winter due to low water vapour. This model simulated peak occurs at Ls=100° for polar latitudes and between Ls=50° to 100° for high latitudes (30°S–60°S). The ozone columns retrieved from SPICAM observations also show high latitude ozone maxima but

for polar winter, data was not available. On the contrary, very low ozone due to the release of water vapour from the polar cap can be seen from Ls= 240° to 360° (southern summer) in southern polar region. Ozone retrievals for southern polar region for L_s=30°–190° are not available, as SPICAM cannot observe the winter poles due to absence of solar irradiance. But from the comparison with GCM results, a reasonable match is seen with the retrieved ozone data in different regions. In the equatorial regions, seasonal variation of ozone is not as pronounced as in the polar region.

4.2.2 Dust optical depths retrieved from SPICAM

The global map of dust optical depth retrieved from SPICAM is shown in Figure 4.12 as a function of season for MY 28. The Figure indicates a background aerosol loading with optical depths less than 0.5 between Ls=0° and 160°. Optical depths measured by

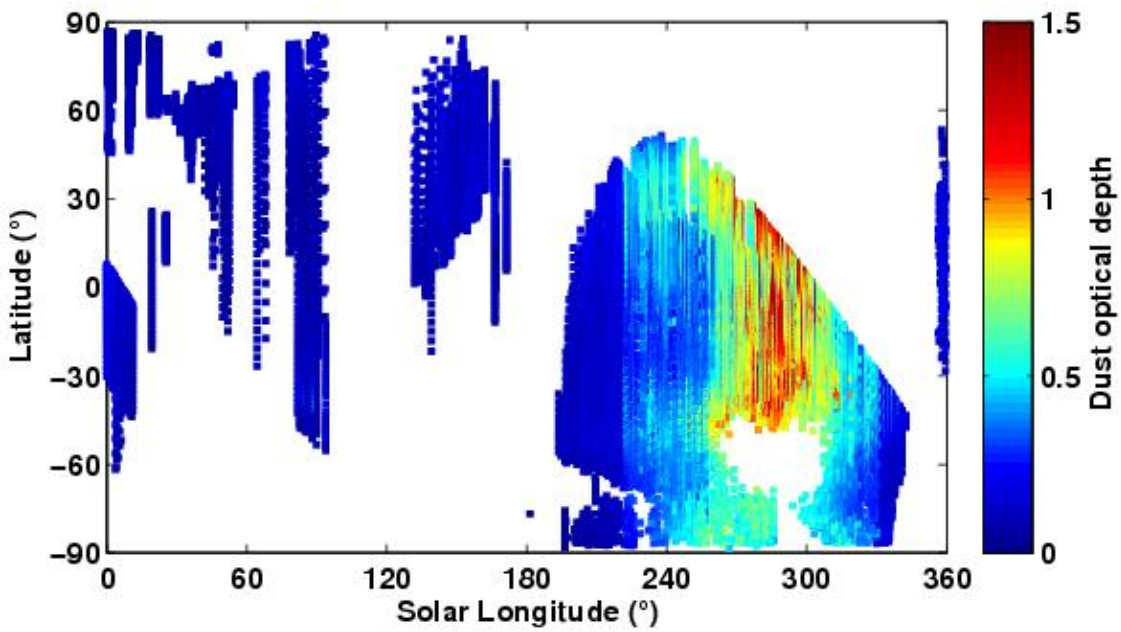

Figure 4.12: Dust optical depth retrieved from SPICAM at λ=300nm for MY 28 as a function of latitude and season.

THEMIS at 9.3 µm start to increase after Ls=220° during MY 28, reaching to about 1.2 at Ls=280° during the global dust storm period of that year (Sheel and Haider, 2016). Similarly the global dust storm can be seen from the current retrieval of dust optical depth

(Figure 4.12), when optical depths start increasing only after Ls=220° and during Ls=240°–330° the values increase to greater than 1.0. The retrieval is thus able to capture the global dust storm and thus compare qualitatively with THEMIS observations (Smith, 2009). The major storm took about a few months for the dust to settle down to the background dust loading. Many of these major dust storms begin in the sub–tropical region in the southern summer season after perihelion, when Mars receives a higher amount of radiative energy from the Sun compared to other seasons. The increased solar insolation increases the temperature and wind speeds that lift dust from the surface into the atmosphere of Mars (Lemmon et al., 2015). The retrieval of dust optical depths can be affected by the presence of clouds, as the retrieval methods yields artificially high dust optical depths, possibly due to the presence of water-ice clouds (which we do not retrieve). In general clouds occur in the cold aphelion seasons. For example, dust optical depths are found higher in the southern polar region during Ls=0°-50° in MY 27. Due to lack of data in the southern polar region those high values of dust optical depth affected by clouds could not be seen during MY 28.

4.2.3 Ozone and dust

Ozone is a very reactive and apart from being sensitive to changes in water vapour in the atmosphere, it is also affected by the dust loading. Dust, which is known to affect various other parameters in the atmosphere, including the ionosphere (Sheel and Haider, 2016), is highly variable. Many dust storms originate in the southern hemisphere and some of these grow into global dust storms in certain years, while regional or local dust storms occur almost every year (Sheel and Haider, 2016). A climatology of nine Martian years of dust loading has revealed that there is always a background aerosol loading of optical depth of about 0.1 between Ls = 0° and 160°, corresponding to a period when dust storms are absent, while the optical depth increases every year (for example, by a factor of 5 at the southern summer tropics), to values in the range 0.3–0.5 corresponding to regional dust storms which typically occur at Ls = 220° (Sheel and Haider, 2016). For global dust storms, the peak optical depth can reach up to for example 1.7 in the southern tropics

during the MY25 global dust storm at Ls=210°. During the regional and global dust storms, detached dust layers have also been observed and modeled (cf. Sheel and Haider, 2016), which could lift dust to altitudes up to 50 km, between L_s=150° and 280°. We consider here two cases: (i) MY 28 which witnessed a global dust storm and (ii) the preceding year MY27, in which a regional storm did occur, though it could not eventually

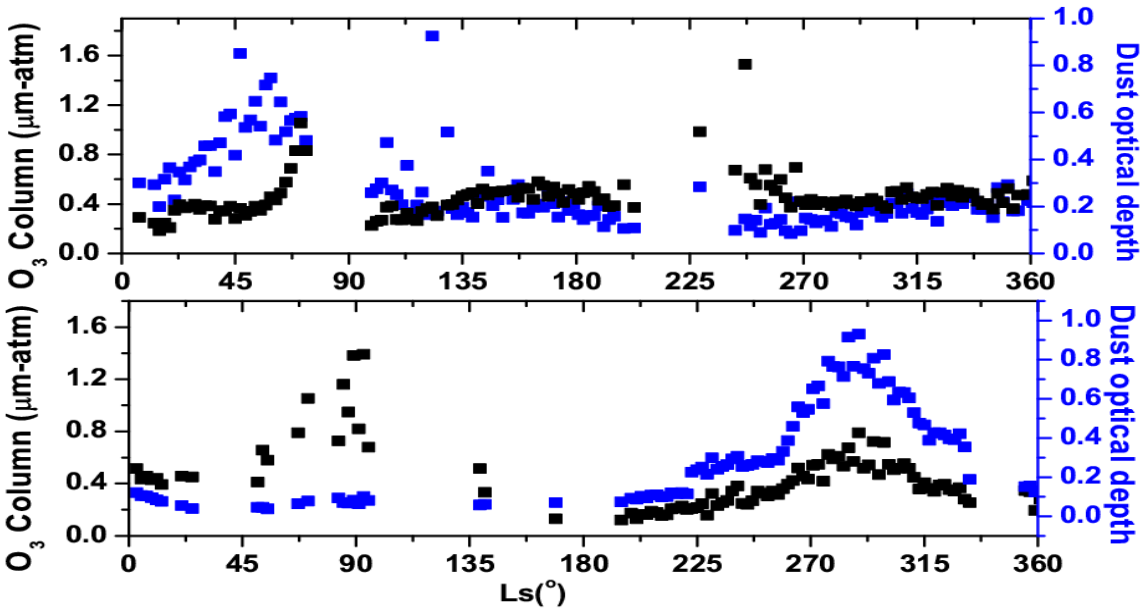

Figure 4.13: Correlation of ozone and dust retrieved from observations by SPICAM, for the latitude region 0°-30°S. The upper panel is for MY 27 (no global dust storm) and lower panel is for MY 28 (global dust storm).

turn into a global storm. In Figure 4.13, we have shown the seasonal behavior of ozone and dust (total optical depth) for MY 27 and MY28 for southern low latitudes (0°-30°S).

A comparison of the panels of Figure 4.13 indicates towards increase of ozone with the increase of dust. As discussed above (Figures 4.10 & 4.11), not much variation in ozone is seen in tropical latitudes. However, in Figure 4.13 we can see a striking feature of ozone increasing with dust during the global dust storm year of MY 28 from Ls=210° to Ls=330°. The ozone columnar values continue to increase after Ls=225° in MY 28 (Figure 4.13), for dust optical depths more than 0.5.

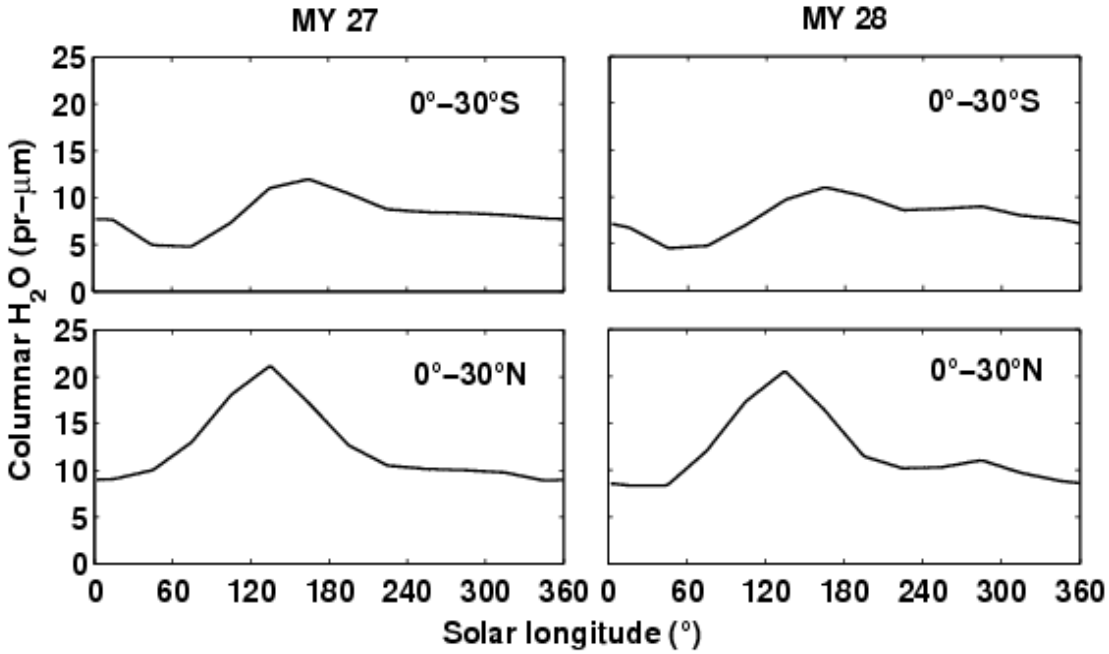

Figure 4.14: Seasonal variation of zonally averaged water vapour columnar abundance simulated by the LMD-GCM for MY27 and MY28 and for the latitude regions 30ºS-0º and 0º-30ºN.

The water vapour column shown in Figure 4.14 indicates that for the two years the amount of water vapour available in the atmosphere is constant (Navarro et al., 2014), therefore the increase in ozone can be attributed to the increased dust loading and its radiative impact. This behavior of ozone column during the global dust storm can be validated with the LMD-GCM simulation for MY 28 with high dust (see Figure 4.15). Other model simulations show that photodissociation rates are drastically reduced during dust storms due to radiative impact of dust, thereby increasing ozone abundances which may be typically increased by 10-50 % (Lindner, 1988).

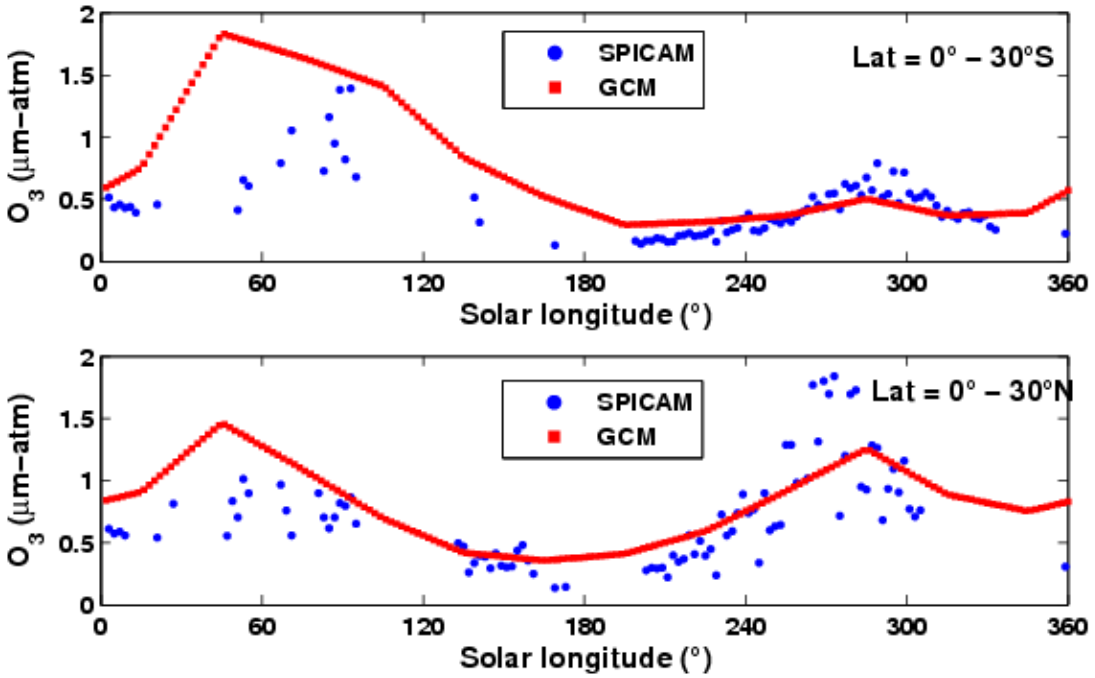

Figure 4.15: Comparison of the retrieved ozone column from SPICAM observation with the GCM simulated values for MY 28 and the latitude regions 30°S-0° and 0°-30°N.

4.2.4 CO-O_3 correlation

Carbon monoxide (CO) in the Martian atmosphere has been observed in the 1.6 and 2.35 µm region by ground based and spacecraft spectroscopy by OMEGA and PFS on Mars Express, CRISM on Mars Reconnaissance Orbiter, and the Heterodyne Instrument for the Far Infrared (HIFI) on board the Herschel space observatory (cf. Hartogh et al., 2010). CO and O_3 are closely related via their common source (photolysis of CO_2) and their common sink (loss with HO_x radicals). Chemical lifetime of CO in the Martian atmosphere is in order of years while ozone lifetime is of few minutes, therefore CO-O_3 correlation cannot be expected based on their chemistry. However it has been shown that the dynamical transport of O atoms from sunlit latitudes increases ozone over the southern polar region (Lefèvre et al., 2008). CO being a non-condensable and stable gas is also used as a dynamical tracer. Therefore in order to investigate the dynamical effect on ozone columnar amount, we evaluate the correlation of GCM simulated O_3 column (as SPICAM

observations for polar nights are not available) with the GCM simulated CO column for each season and over six latitude regions as shown in Figure 4.16. Modeled CO concentrations qualitatively compare well with observations (Smith et al., 2009). As can be seen from the Figure 4.16, CO does not show much variation with O_3 over the latitude region 60°S–60°N compared to over polar region, indicating insignificant dynamical contributions to the ozone column. However during winter over the polar region, CO column increases with ozone column, the correlation being greater over southern polar region compared to the northern region. This indicates a higher dynamical contribution towards the increase in ozone columnar value over southern polar winter.

To derive the percentage contribution of dynamics, we compare the ozone vertical profile from the 3D as well as the 1D version of the LMD General Circulation Model, as the 3D version includes the large scale Martian dynamics. Apart from this, all other physical processes such as CO_2 condensation, radiative interaction within the atmosphere, water cycle, dust condition and solar insolation are kept same. Both the models were initiated at Ls=0 and ran with the full photochemistry module of Lefevre et al. (2004). For the 1D model, we input a reference surface pressure of 610Pa and a temperature profile for polar region. In Figure 4.17 we show the number density of ozone derived from both model calculations over 70°S during Ls = 45°. In polar nights, concentration of O atoms reduces drastically due to absence of its major source (photolysis of CO_2 and O_2) as well as absence of transport. This leads to decrease in ozone concentrations too, reflecting a decrease in ozone column of about ~24μm-atm compared to the case when dynamics is present (Figure 4.17). The shape of the ozone vertical profile is decided by the H_2O profile and the hygropause altitude. In case of 3D simulation hygropause occurs at lower altitude and hence the second peak in ozone is occurring at a lower altitude compared to the 1D simulation. The exact cause of the increase in water vapour saturation level in 1D simulation could not be pointed out.

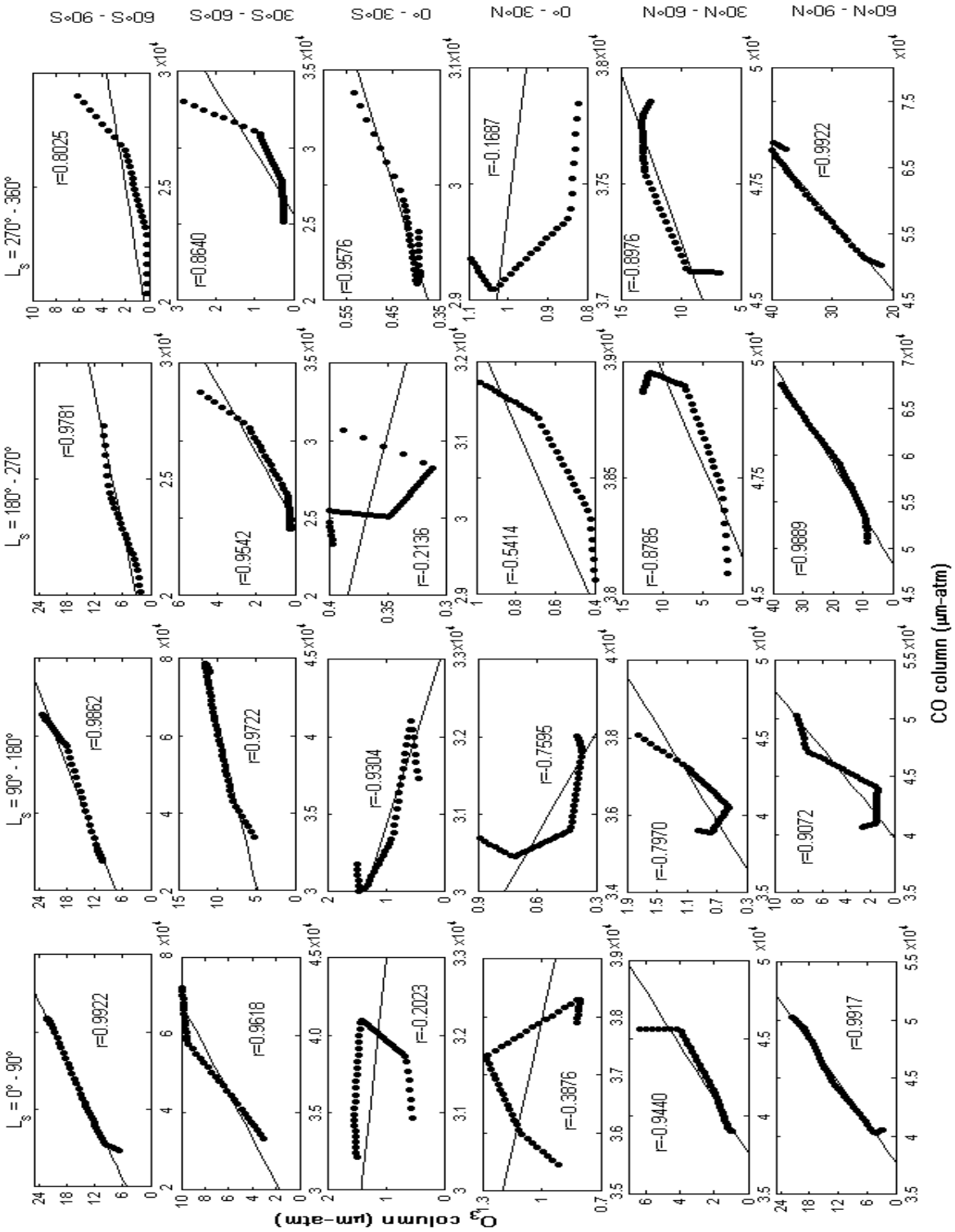

Figure 4.16: Correlation between O_3 and CO from the LMD-GCM, for the four seasons: spring, summer, autumn and winter, and the six latitude regions as in Figure 4.11.

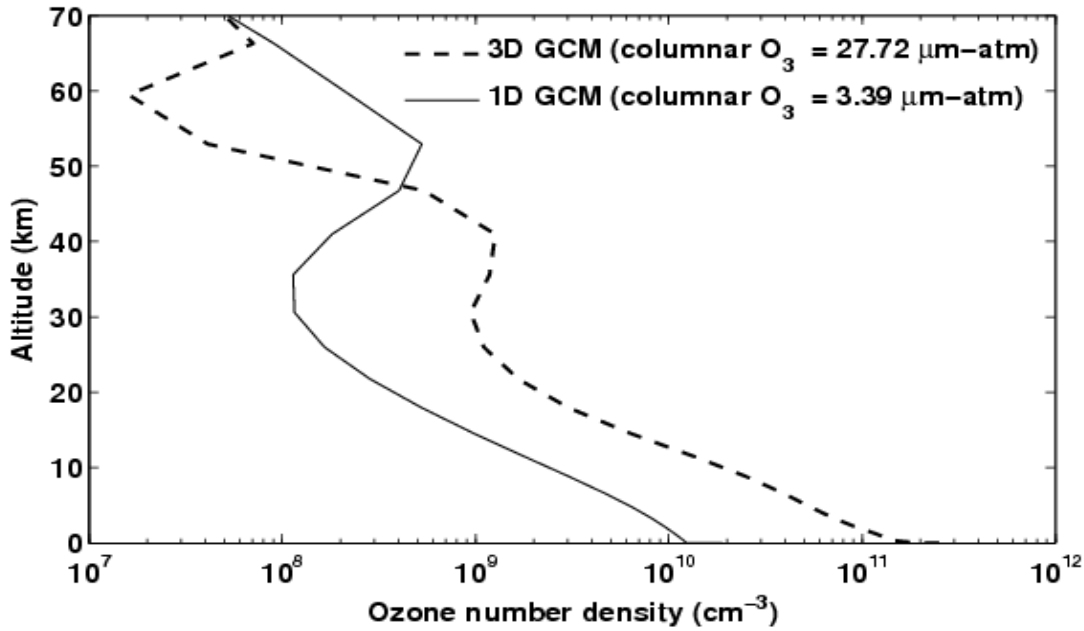

Figure 4.17: Ozone vertical profiles simulated for 3D and 1D version of LMD-GCM. 3D version includes dynamics whereas the 1D version does not include dynamics.

4.3 Conclusion

The above study satisfies one of the objectives namely the seasonal and spatial variation in the of the trace species. The chemistry and behaviour of O, O_3, and H_2O over Martian globe and seasons have been studied in detail. The study also gives spatio-temporal behaviour of the catalytic radicals (H, OH, and HO_2) in the atmosphere. The seasonal variability of ozone is closely related to the production and loss of the odd oxygen family (O_x). We have studied the relative importance of various reactions involved in the production and loss of O_x as a function of season and height. We observe that the seasonal variability of ozone is broadly connected to the abundance of water vapour below 60 km, which in turn is related to the hygropause. Above the hygropause, water vapour mixing ratios decrease very fast. Over northern polar region during aphelion season, water vapour saturates above 20 km (Figure 4.1). Thus, destruction of odd oxygen due to catalytic HO_x radicals remain mostly bound to the lower atmosphere. For the southern polar region during perihelion season, atmosphere of Mars is warmer and can carry more water vapour,

leading to increase of Ox-destroying hydrogen radicals. The hygropause in this case is higher and water vapour slowly falls off with negligible densities only near 80 km, which increases the column integrated loss rates compared to aphelion season (Table 1). A similar behavior is noted over 20°S–40°S, where the hygropause height increases in the perihelion season compared to aphelion season. Thus during the perihelion season, more water vapour is available at heights relevant to the present work, due to rise of hygropause. The largest direct loss process of ozone occurs via reaction $H+O_3$. However, the largest overall loss of ozone occurs indirectly via the loss of O atoms (as part of O_x family) through reaction HO_2+O. On the other hand, OH plays important role in ozone destruction by destroying O only in the upper atmosphere. For a particular latitude and season, the loss rate due to H is always higher in nighttime than in daytime. Therefore, we conclude that O_x is in photochemical equilibrium between production and loss processes up to about 30 km in the aphelion season, and up to 45 km in the perihelion season. Photochemical equilibrium occurs when chemistry dominates over transport, or when photochemical lifetime is much smaller than the dynamical lifetime. In the domain of photochemical equilibrium, the HO_2 + O reaction is by far the dominant loss process of O_x. Above the domain of photochemical equilibrium, the HO_x+O, $H+O_3$ and O+O reactions have comparable contributions to the O_x loss. The $O+O_3$ reaction is always a minor contribution to the O_x loss.

We have also retrieved ozone columnar abundances and dust for MY27-MY28 from raw spectral radiances recorded by SPICAM onboard Mars Express and by using a forward radiative transfer model. We have also run the photochemistry coupled LMD-GCM on our HPC cluster, to simulate ozone, carbon monoxide and water vapour.

Seasonal variability of total columnar ozone was studied for two Martian years at tropical, mid and high latitudes. Seasonal variations in ozone are not prominent in tropical latitudes, with ozone column values observed in this region below 10µm-atm. For mid-latitudes, ozone exhibits a peak in both northern and southern winters. The GCM simulations compare reasonably well with observations in these regions. A pronounced seasonal variability of ozone is seen in the GCM results in high latitudes of both

hemispheres, with a maximum in winter and minimum in summer. Unfortunately, SPICAM observations are not available very frequently in the polar region. An ozone-water vapour anti-correlation is seen at high latitudes.

We have also retrieved dust optical depths from SPICAM along with ozone, and find that during dust storms, ozone columnar amounts increase with increase in dust optical depth due to radiative impact of dust. The increase of ozone can be as high as 50% of the ozone without global dust storm. A similar result can be seen in ozone simulated by the LMD-GCM for the dark dust storm of MY 28.

The GCM model simulations of O_3 and CO have been used to study their correlation as the amount of CO can indicate the dynamical effect on the ozone column. We find that the southern polar region exhibits a higher increase in ozone column due to the dynamically carried O atoms. During Ls = 45°, the ozone column over the southern polar region can increase from 3 to 27 µm-atm due to dynamical effect. On the other hand, in the northern polar region, the dynamical contribution is much less than the chemical contribution, while over the equator and tropical region, the dynamical effect is insignificant.

Table 4.1. Column integrated production and loss rates for various pathways of O_x chemistry, locations and seasons.

	O+O+M	$O+O_3$	$O+HO_2$	O+OH	$H+O_3$	$O+O_2+CO_2$
Daytime rates ($cm^{-2}s^{-1}$)						
Lat =60°N–90°N L_s=60° – 120°	6.87Ex10^5	4.66 x10^3	1.41 x10^7	1.47 x10^6	9.93 x10^5	2.13 x10^8
Lat = 0°N – 20°N L_s =60° – 120°	7.46Ex10^5	5.18 x10^3	1.57 x10^7	8.76 x10^5	6.37 x10^5	2.14 x10^8
Lat=0°S – 20°S L_s =60° – 120°	1.33 x10^6	4.76 x10^3	1.42 x10^7	9.60 x10^5	6.99 x10^5	2.17x10^8
Lat=20°S – 40°S L_s =60° – 120°	1.14 x10^4	5.79 x10^3	1.06 x10^7	8.06 x10^5	6.19 x10^5	4.42 x10^8
Lat =0°N – 20°N L_s=240°– 300°	1.29 x10^5	3.46 x10^4	1.96 x10^7	1.77 x10^6	6.35 x10^5	2.91 x10^8
Lat = 0°S – 20°S L_s =240° – 300°	8.95 x10^4	3.33 x10^4	2.23 x10^7	1.99 x10^6	6.75 x10^5	2.19 x10^8

Lat=20°S – 40°S L_s =240° – 300°	6.20 x10^4	3.18 x10^4	2.34 x10^7	2.15 x10^6	6.28 x10^5	1.63 x10^8
Lat=60°S – 90°S L_s =240° – 300°	6.71 x10^4	5.40 x10^3	1.98 x10^7	2.45 x10^6	4.49 x10^5	4.63 x10^7
Nighttime rates ($cm^{-2}s^{-1}$)						
Lat= 60°N – 90°N L_s= 60° – 120°	3.98 x10^5	1.29 x10^3	1.39 x10^6	1.97 x10^6	2.88 x10^6	2.10 x10^6
Lat= 0°N – 20°N L_s= 60° – 120°	2.76 x10^5	8.60 x10^2	3.76 x10^5	1.45 x10^6	2.38 x10^6	3.28 x10^6
Lat= 0° – 20°S L_s= 60°– 120°	4.59 x10^5	1.17 x10^3	4.81 x10^5	1.88 x10^6	2.71 x10^6	3.33 x10^6
Lat= 20°S – 40°S L_s= 60° – 120°	5.46 x10^5	7.87 x10^2	4.92 x10^5	1.30 x10^6	1.93 x10^6	2.66 x10^6
Lat= 60°S – 90°S L_s= 60° – 120°	4.94 x10^6	1.10 x10^4	9.04 x10^5	4.14 x10^6	4.09 x10^6	3.93 x10^6
Lat= 60°N – 90°N L_s= 240° – 300°	3.74 x10^6	1.01 x10^3	7.68 x10^6	9.71 x10^6	2.39 x10^6	2.83 x10^6
Lat= 0°N – 20°N L_s= 240° – 300°	5.10 x10^4	1.16 x10^1	1.09 x10^6	1.02 x10^6	2.87 x10^5	2.76 x10^5
Lat= 0° – 20°S L_s= 240° – 300°	4.02 x10^4	5.48 x10^0	8.32 x10^5	7.85 x10^5	2.08 x10^5	2.00 x10^5
Lat= 20°S – 40°S L_s= 240° – 300°	4.37 x10^4	6.07 x10^0	8.79 x10^5	8.13 x10^5	2.08 x10^5	2.01 x10^5
Lat= 60°S – 90°S L_s= 240° – 300°	6.77 x10^4	1.01 x10^1	1.54 x10^6	1.19 x10^6	2.28 x10^5	8.20 x10^4

Table 4.2. Percentage contribution (in %) of each loss process to the total loss of odd oxygen (sum of all loss processes), corresponding to Figure 9. For each height interval, the column integrated loss rate (cm^{-2} s^{-1}) is considered for that interval to arrive at the estimate.

Lat = 60°N - 90°N, Ls = 60°-120°, sza< 70°

	O+O+M	O+O_3	HO2+O	OH+O	H+O_3
0 – 15 km	0.01	0.04	98.80	0.05	1.09
15 – 30 km	0.32	0.01	94.31	1.78	3.58
30 – 45 km	3.72	0.02	65.39	18.59	12.28
45 – 60 km	10.15	0.01	37.60	37.12	15.12
60 – 80 km	53.85	0.02	10.93	22.59	12.61

Lat = 60°N - 90°N, Ls = 60°-120°, sza>96°

	O+O+M	O+O_3	HO2+O	OH+O	H+O_3
0-30 km	<<0.01	0.01	83.88	0.12	15.99
30-60 km	1.69	0.01	24.60	27.94	45.76

60-80 km	20.29	0.04	5.48	38.79	35.39

Lat = 60ºN - 90ºN, Ls = 240º-300º, sza>96º

	O+O+M	$O+O_3$	HO2+O	OH+O	$H+O_3$
0-30 km	<<0.01	<<0.01	92.71	0.01	7.29
30-60 km	6.08	<<0.01	39.70	45.55	8.67
60-80 km	32.88	0.01	20.62	33.86	12.63

Lat = 60ºS - 90ºS, Ls = 240º-300º, sza< 70º

	O+O+M	$O+O_3$	HO2+O	OH+O	$H+O_3$
0 – 15 km	0.02	0.06	98.38	0.15	1.39
15 – 30 km	<<0.01	<<0.01	98.90	0.48	0.62
30 – 45 km	0.05	<<0.01	90.06	7.77	2.13
45 – 60 km	0.15	<<0.01	62.27	34.00	3.58
60 – 80 km	2.99	<<0.01	40.70	51.14	5.17

Lat = 60ºS - 90ºS, Ls = 60º-120º, sza>96º

	O+O+M	$O+O_3$	HO2+O	OH+O	$H+O_3$
0-30 km	0.02	0.02	81.85	0.78	17.33
30-60 km	9.79	0.07	13.57	38.05	38.53
60-80 km	47.65	0.09	1.98	25.63	24.64

Lat = 60ºS - 90ºS, Ls = 240º-300º, sza>96º

	O+O+M	$O+O_3$	HO2+O	OH+O	$H+O_3$
0-30 km	<<0.01	<<0.01	85.18	0.01	14.81
30-60 km	0.09	<<0.01	62.01	31.27	6.63
60-80 km	3.55	<<0.01	39.81	48.23	8.40

Lat = 20ºS - 40ºS, Ls = 60º-120º, sza< 70º

	O+O+M	$O+O_3$	HO2+O	OH+O	$H+O_3$
0 – 15 km	0.08	0.08	97.52	0.17	2.14
15 – 30 km	0.26	0.01	93.57	2.47	3.70
30 – 45 km	6.29	0.01	66.03	17.89	9.77
45 – 60 km	33.52	0.01	27.29	28.61	10.57
60 – 80 km	73.16	0.01	6.18	13.13	7.52

Lat = 20ºS - 40ºS, Ls = 60º-120º, sza>96º

	O+O+M	$O+O_3$	HO_2+O	OH+O	$H+O_3$
0-30 km	0.03	0.01	69.03	1.26	29.67
30-60 km	1.88	0.02	15.87	29.04	53.20
60-80 km	23.93	0.02	4.04	36.66	35.35

Lat = 20ºS - 40ºS, Ls = 240º-300º, sza< 70º

	O+O+M	$O+O_3$	HO_2+O	OH+O	$H+O_3$
0 – 15 km	0.05	0.30	96.71	0.20	2.74
15 – 30 km	<<0.01	<<0.01	98.85	0.41	0.74
30 – 45 km	0.03	<<0.01	91.93	6.43	1.61
45 – 60 km	0.52	<<0.01	58.46	35.75	5.27
60 – 80 km	2.98	<<0.01	40.97	50.31	5.75

Lat = 20ºS - 40ºS, Ls = 240º-300º, sza>96º

	O+O+M	$O+O_3$	HO_2+O	OH+O	$H+O_3$
0-30 km	<<0.01	<<0.01	52.25	0.00	47.74
30-60 km	0.22	<<0.01	55.19	35.30	9.29
60-80 km	2.85	<<0.01	38.49	46.97	11.69

Chapter 5

Martian Lower Ionosphere

The study of the ionosphere of Mars is essential for estimating the importance of atmospheric escape which in turn aids in studying the evolution of the planet's climate. Ionosphere is also important to understand phenomena like atmospheric electricity and, the large scale electric currents. The Ionosphere is closely linked with the chemistry and dynamics of the neutral atmosphere and is affected by solar wind. Due to existence of the remnant magnetic field, the Martian ionosphere presents itself as a unique plasma laboratory. Thus the chemistry, dynamics and structure of the ionosphere of Mars vary with location and time as a result of variability in solar forcing, atmospheric dynamics and composition. This variability of the ionosphere due to the seasonal variability of the neutrals and dust will be studied in the present chapter.

5.1 Introduction

There have been numerous observations and modelling studies on ions of the upper atmosphere. As described in Chapter 1, O_2^+ and CO_2^+ ions constitute most of the ion densities in the upper ionosphere. The first in-situ measurement of O_2^+ and CO_2^+ was made by the retarding potential analyzer (RPA) experiment onboard Viking 1 and 2 (Hanson et al., 1977). The ionosphere has also been remotely observed starting from Mariner 4 (Kliore, 1965), and later followed by other missions such as Mariner 6, 7, and 9, Mars 2 and 3. These were followed by extensive observations of the ionospheric profiles through radio occultation experiments such as onboard the MGS (Bougher et al., 2004),

the Mars radio science experiment (MaRS) on board MEX (Patzold et al., 2005) and the Radio Occultation Science Experiment (ROSE) (Mendillo et al., 2017) onboard MAVEN (Mahaffy et al., 2015; Benna et al., 2015).

The radio occultation (RO) experiments probes the ionosphere and neutral atmosphere through the change in the path of a radio beam influenced by the planet's atmosphere, which is measured in terms of a bending angle or Doppler shift of the transmitted radio frequency. In this experiment a transmitter onboard the spacecraft emits radio waves before it is about to be occulted by the planet Mars. The radio waves while travelling through the planet's atmosphere suffer a bending or phase shift (Doppler shift), which is recorded by an Earth based receiver. The electron density profiles are determined from the Doppler shift. Only ionosphere higher than 80 km can be observed using RO experiment due to the limitation posed by the geometry (Withers, 2009) and thus probing lower ionosphere becomes a difficult task. A typical electron density profile retrieved by

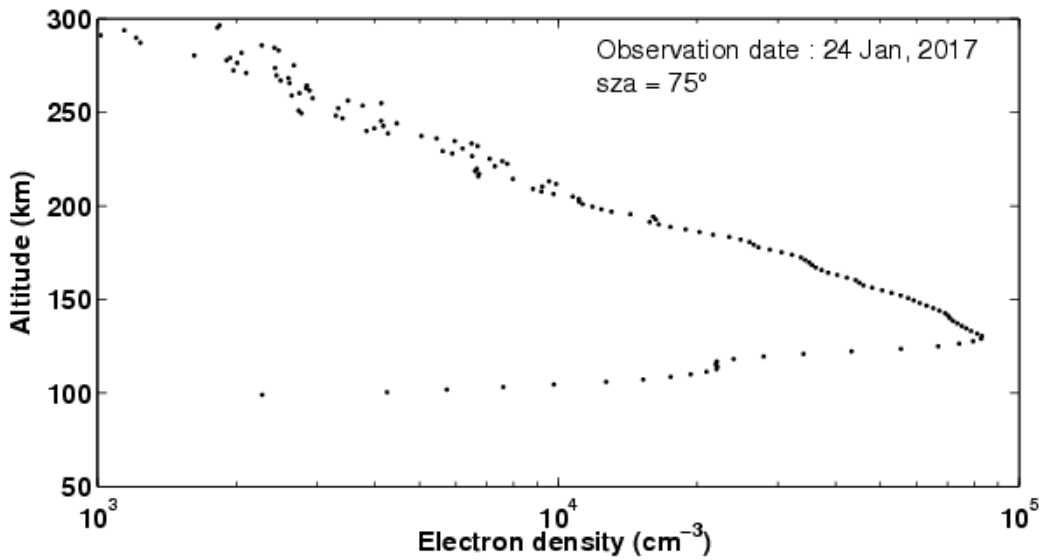

Figure 5.1: Electron density profile retrieved from radio occultation science experiment (ROSE) on board MAVEN. The figure is taken from (Withers et al., 2018).

the most recent radio occultation experiment (ROSE) on board MAVEN is shown in the Figure 5.1. The electron density corresponds to the date 24 January 2017, solar zenith

angle (sza) = 75° and latitude = 6°S – 7°S. The peak in the electron density profile occurs at the altitude around 140 km due to the solar EUV ionization. At the altitude ~120 km, a soldier type structure is found which resulted of ionization due to the soft X-rays (Withers et al., 2018).

The top side of the ionosphere has been extensively observed by ionospheric sounders such as Mars Advanced Radar for Subsurface and Ionosphere Sounding (MARSIS) onboard MAVEN (Gurnett et al., 2005). The principle of the ionospheric sounders is to transmit electromagnetic waves of (0.9-4) MHz frequencies which are reflected back to and received at the ionospheric sounders on board the spacecraft. The waves echo from the layers of ionosphere where the plasma frequency of the layer equates the signal frequency. The low frequency signal waves cannot propagate through a medium with high plasma frequency and the high frequency signal waves penetrate deep through the plasma layer. Due to this mechanism ionospheric sounder can only probe the upper side of the ionosphere from the peak layer of electron density. Plasma frequency of a layer is given by $f_p = 8980\sqrt{n_e}$ Hz (Gurnett and Bhattacharjee, 2005) where n_e is the electron density in cm^{-3} in the top side of the peak electron density.

Modelling studies to better understand Martian ionospheric electron density has been carried out since 1970's. Fox et al. (1996) modelled the upper ionosphere and thermosphere, and they found that electron density increases at peak by a factor of three during solar maxima conditions when compared with the solar minima conditioned observations. Mendillo et al. (2005) employing a photochemical model determined the total electron content over the subsolar latitudes for perihelion and aphelion position of the Sun. They observed an increase in total electron content (TEC) by a factor of 2, from perihelion to the aphelion position. Haider et al. (2009) have studied the ionosphere and defined D, E and F layer of Martian ionosphere over high latitude terminator in analogy to the Earth's ionosphere. They have identified the D layer peak between 25 and 35 km, E layer peak between 100 and 112 km, and F layer peak between 125 and 145 km (Figure 5.2). They have also inferred the maximum electron densities in the respective layers as

approximately 10^2, 10^4 and 10^5 cm^{-3}. The peak density in the F layer depends on the solar zenith angle according to the Chapman theory. The D region is produced due to the ion-

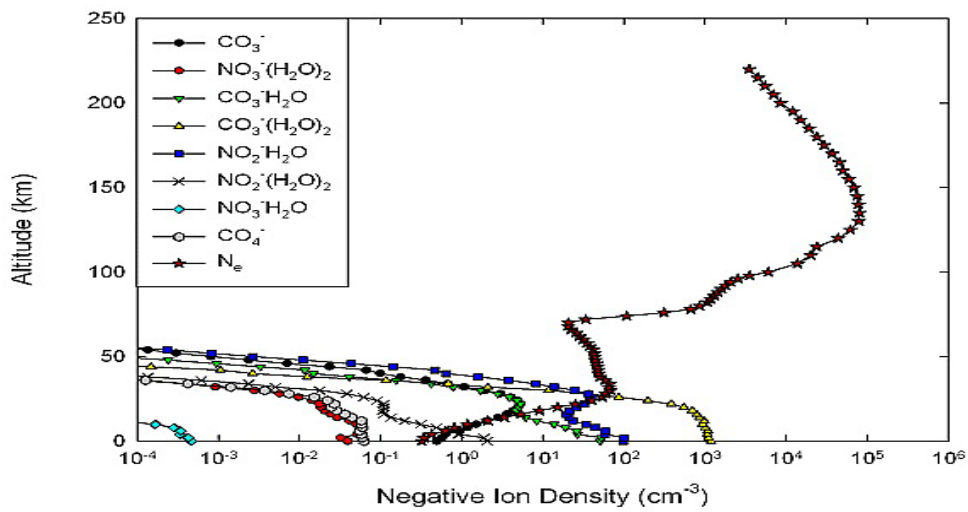

Figure 5.2: D, E, and F layers in the daytime at high-latitude terminator ionosphere of Mars (Haider et al. 2009).

ization owing to the impinging galactic cosmic rays. The interplay of chemistry in the upper ionosphere can be found out in the modelling studies of Nagy et al. (2004), Haider et al. (2009) and Haider, (2008). The immediate positive ions created due to the solar EUV and X rays are the CO_2^+ leaving the electrons free in the atmosphere.

$$CO_2 + h\nu \rightarrow CO_2^+ + e \tag{5.1}$$

The ion CO_2^+ is almost immediately removed by O leading to O_2^+ following the below scheme (Nagy et al., 2004).

$$CO_2^+ + O \rightarrow O_2^+ + CO \tag{5.2}$$

$$CO + O_2^+ \rightarrow O^+ + CO_2 \tag{5.3}$$

$$O^+ + CO_2 \rightarrow O_2^+ + CO \tag{5.4}$$

$$O_2^+ + e \rightarrow O + O \tag{5.5}$$

O_2^+ is destroyed in the dissociative recombination and produce energetic O molecules. This process mainly occurs in the upper atmosphere above 100 km because solar EUV cannot penetrate any deeper in the atmosphere. The reaction of charge removal ($CO_2^+ + O \rightarrow O_2^+ + CO$) is very fast compared to the other processes which makes $O_2^+$the most dominant ion (between 130 and 240 km) in the upper atmosphere (Withers, 2009). Other dominant ions in upper Martian ionosphere are CO_2^+, O^+ and NO^+.

The measurements of the lower ionosphere have not been possible due to the difficulties associated with the observations techniques as discussed in the above. Therefore, only tool remains to understand the lower ionosphere is numerical modelling from the knowledge of the neutral species and ionizing source, i.e, galactic cosmic rays (GCR). Whitten et al. (1971) developed the first lower ionospheric theoretical model, considering solar radiation and cosmic rays as ionizing agents. They have included 35 ion-neutral reactions in their study which infers the possibility of hydronium ions and their hydrates to be the major ionic species. Later with the better knowledge of the neutral atmosphere Molina-Cuberos et al. (2002) have developed a more sophisticated ion model with 32 ions and 12 neutrals.

Sheel and Haider (2012), in their study of the ion production in the lower atmosphere due to galactic cosmic rays impact, have found the major ion to be $H_3O^+(H_2O)_2$. They have also found that the most important process is the ion-neutral collisions after calculating the rate of the reactions between $H_3O^+(H_2O)_{2,3}$, water and air molecules. A density of free electron is constructed due to the ionization in the lower ionosphere with GCR. The presence of electrons and electron affinitive species such as O, O_2 and O_3 produces negative ions such as O^- and O_2^- through electron capture. Other negative ions such as CO_3^-, CO_4^-, are product of these initial ions with other neutrals of the atmosphere.

5.2 Objective

The photochemical models studies of the ion-chemistry mentioned in the previous section predict the possible densities of the negative and positive ions as well as that of electron. These models show the importance of the water vapour in producing hydrated

ions. Sheel and Haider (2012) has studied the lower ionosphere considering distinct dust scenarios from observations of MGS and Mars Odyssey. They have found that ion densities are lowered by an order of magnitude during major dust storm. The objective of our study is to determine the seasonal variation in the major and important ion densities over different region of the Mars. The atmosphere we used in the model corresponds to seasonal bin of width 90° and latitudinal bin of size 30°. The study is to derive a correlation between the ion content, and the dust and water vapour and to calculate the major ion densities as a function of latitude and seasons.

5.3 Ion-dust model

In the ion-dust model we solve the one dimensional continuity equation for each ionic component in order to find out the number densities of the positive and negative ions. The nature of reactions have been discussed in chapter 2. The equations are given below.

$$\frac{dI^+}{dt} = -K'_{in}.N.I^+ - K_{ie}.E.I^+ - K'_{ip}.I^+ - K_{ia}A.I^+ - I^+I^-\alpha_{ii} - \alpha_1 A^- I^+ + P_+ \quad (5.6)$$

$$\frac{dI^-}{dt} = -K'_{in}.N.I^- - K'_{ip}I^- - K_{ia}A.I^- - I^+I^-\alpha_{ii} - \alpha_1 A^+ I^- + P_- \quad (5.7)$$

$$\frac{dA^+}{dt} = K_{ia}A.I^+ - K_{ae}.E.A^+ - A^+I^-\alpha_2 - \alpha A^+ I^- + P_- \quad (5.8)$$

$$\frac{dA^-}{dt} = K_{ia}.A.I^- - \alpha_1.A^-.I^+ - \alpha.A^+.A^- \quad (5.9)$$

In the above equations $K'_{in}.N = \sum_i k_i n_i$which is the reaction rate coefficient multiplied by the neutral density. This term indicates the losses of the ions due to ion-neutral collision. $K_{ie}.E = \sum_i k_{ie}\, n_e$is the loss of positive ions due to recombination with electrons. Complex positive ions such as $O_2^+CO_2$ can be lost due to collision with photons and negative ions such as CO_4^- can lose the extra electron due to collision with photons. In the above equation photon collision is represented byK'_{ip}. K_{ia} is the coefficient for the attachment of ions to the aerosol and A denotes the aerosol density. $\alpha_{ii}$is the recombination coefficient of the ion-ion recombination, α denotes the attachment between negatively and positively charged aerosols. The attachment coefficients of positively and negatively

charged ions onto the oppositely charged aerosols are denoted by α_1 and α_2 respectively. P_+ and P_- denotes the total production rate of the positive and the negative ions respectively.

5.4 Input parameters

In the lower atmosphere neutrals such as CO_2, Ar, N_2, O_2, CO, H_2, H_2O, O, O_3, NO, NO_2 and HNO_3 get ionized and produce positive ions and electrons. The free electrons get captured by O, O_2 and O_3 due their electron affinity and give rises to negative ions in the lower regions. A full chemistry of those positive, negative and electron are discussed in details in Sheel and Haider (2012).

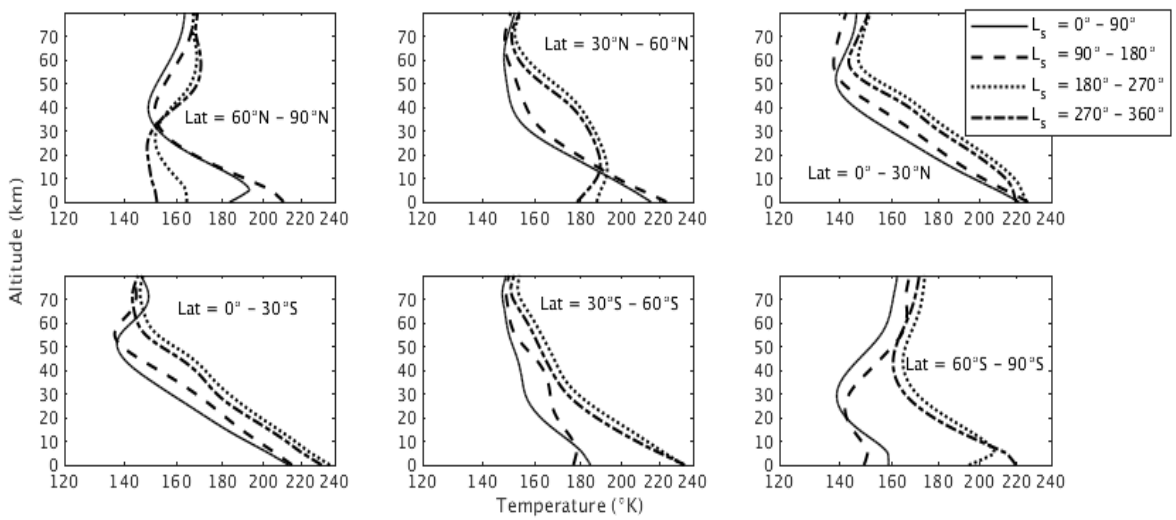

Figure 5.3: Temperature profiles corresponding to the different seasons and different regions. These profiles have been used to form the neutral atmosphere for the ion-dust model. The latitude region of the studies are given in the Figure panels while the line styles indicate different season as shown in the legend.

The ion-dust model needs a theoretical atmosphere so as to predict the possible ion densities. Input for the ion model has been prepared with the help of LMD-GCM. Twelve neutral species have been incorporated in the model namely CO_2, Ar, N_2, O_2, CO, H_2, H_2O, O, O_3, NO, NO_2 and HNO_3. The seasonal variations in the number density of the major species such as CO_2, N_2, O_2, CO, H_2 are not significant in terms of changes in ion

densities. Also the nitrogen species does not play much of a crucial role for the seasonal variation in the major ions to be discussed in next sections. An average density plot of these neutral species is given in the below Figure 5.4.

The ion densities are sensitive to temperature, water vapour and dust contents of the atmosphere (Molina-Cuberos et al., 2002; Sheel and Haider, 2012; Sheel and Haider, 2016). The ion-dust model is restricted up to altitude 70 km so that the influence of solar EUV ionization, meteor ablation and the upper atmosphere ion-chemistry cannot effect the results. To study the seasonal variation of the lower ionosphere of Mars we have divided the whole globe into six latitude bins: 0°N-30°N, 30°N-60°N, 60°N-90°N, 0°S-30°S, 30S^{o}-60°S, and 60°S-90°S. And the whole year is divided into four seasons of width 90° starting from Ls = 0° i.e Ls=0°-90°, Ls= 90°-180°, Ls = 180°-270°, and Ls = 270°-360°. Each latitude bin is corresponding to one of the latitude regions high, mid, or low. Such classification will help us to view the global and annual picture of the ions behaviour.

Figure 5.3 shows the temperature profiles over the latitude regions and for the seasons considered in this study. The latitude are indicated in every panels and the seasons are indicated by the line styles. During summer over low latitude regions surface temperature is above 220° K. The temperature falls off to around 140°K at 50 km and above which it remains fairly constant in the isothermal mesospheric region. Over the northern mid latitude the temperature is around 220°K during summer which decreases to 150° K at 30 km and above that temperature variation reduces. During winter over this region, the surface temperature decreases to 180° K. Near the surface a small inversion in temperature can be seen below 10 km. At 14 km temperature rises to 192° K. Above the tropospheric altitudes an increases in temperature can be seen over mid and high latitude region during winter caused due to polar warming.

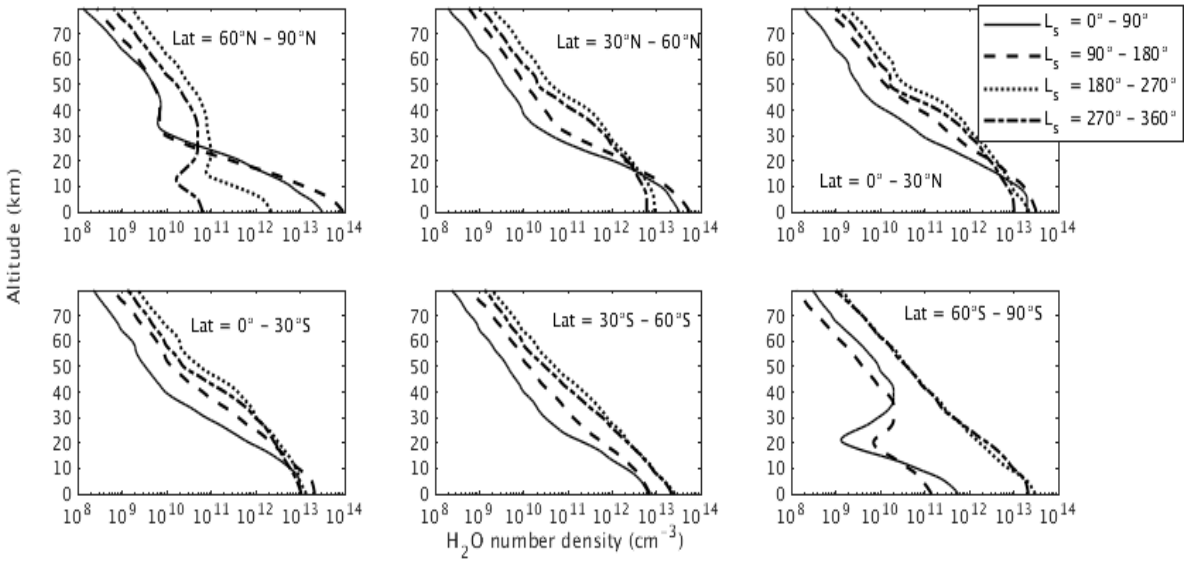

Figure 5.4: Water vapour density profile for different season over different regions. Legend of the figure is same as the Figure 5.3.

Figure 5.4 shows the seasonal and regional variation of water vapour number density. Source of water vapour in Mars are the polar caps and regolith which traps and release water vapour during winter and summer respectively. During northern summer (Ls = 90°-180°) water vapour density is the maximum (~ 10^{14} cm^{-3}) near surface. This maximum density decreases rapidly by four orders of magnitude at 30 km due to the decrease in temperature. During season, Ls = 180° – 360°, the density decreases by few orders at the surface. A similar contrast in the H_2O density is seen over southern polar region as well. In other regions the seasonal variation in water vapour is smaller. The vertical profile of the water vapour is governed by temperature. During season Ls = 0° – 180° temperature decreases and falls off rapidly due to which water vapour saturates at lower altitudes and thus the H_2O decreases above hygropause. However, during Ls = 180° – 360°, Mars is comparatively near the Sun, which increases temperature in southern hemisphere and in the northern mid and low latitude region above 10 km which gives rise to a greater water vapour density in the altitudes above 10 km than that during Ls = 0°-90°.

Dust is the most variable atmospheric quantity in Martian atmosphere same as water vapour for Earth's atmosphere. Martian year 27 has witnessed few regional dust storms during perihelion season (Smith, 2009). We have constructed the surface dust density as prescribed in Sheel and Haider, 2016.

$$n_s = n_0(\tau/\tau_0) \tag{5.10}$$

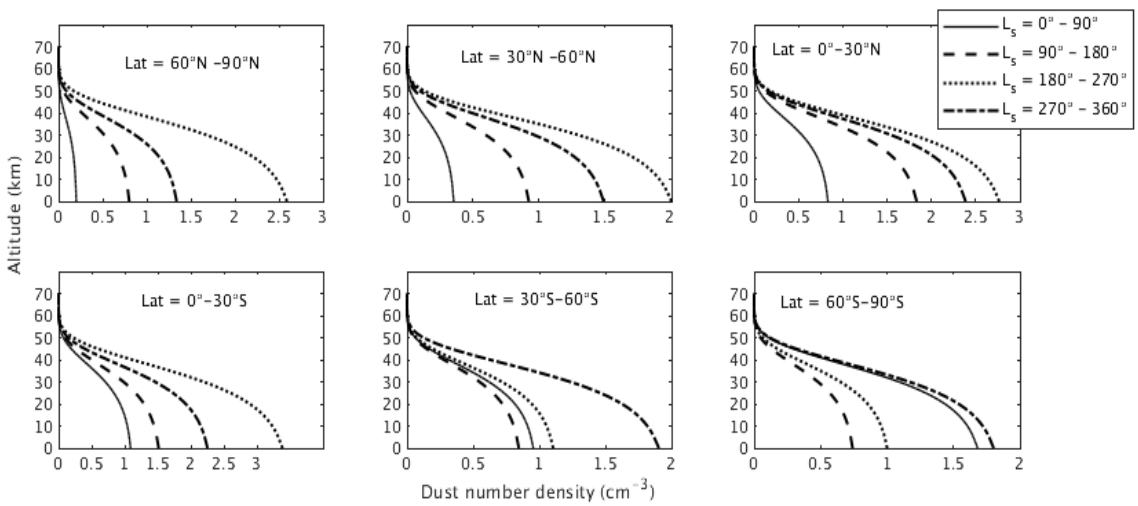

Figure 5.5: Dust number density profiles. Text in the panels and the line styles in the legend indicate latitude regions and seasons similar to Figure 5.3.

In Eq (5.10) n_0 is the surface dust number density corresponding to the optical depth $\tau_0$and $n_s$is the scaled surface dust density corresponding to τ. The optical depth for the current purpose is taken from THEMIS observations. $n_0$is calculated using the equation $\int n_0 dz = \frac{\tau_0}{Q_{ext}}.G$ (Heavens et al., 2011), where Q_{ext} represents the dust extinction coefficient and G is the averaged geometric cross section. The value of Q_{ext} (1.5) is taken from Madeleine et al., 2011 at wavelength 9 µm and the distribution for the dust size used is modified gamma distribution. With these n_0 becomes 1.2 cm^{-3} for τ_0 = 0.1. The vertical distribution of dust has been constructed according to the below equation which is known as Conrath equation (Conrath, 1975).

$$q(z) = q_0 \exp(\gamma(1 - e^{z/h})) \tag{5.11}$$

where $q(z)$ is the dust number density at height z and $q_0$is the dust number density at the surface. γ is called Conrath parameter having value equal to 0.03 which though to represent typical dust condition in Mars (Pollack et al., 1990) and h is scale height. Figure 5.5 shows the vertical dust distribution for MY 27.

Over the equator high dust densities are found during Ls = 180° – 360°. Dust densities reaches maximum over the southern low latitude region. Over the northern polar region the minimum density is calculated which are less than 0.2 cm^{-3} during aphelion season. Over the southern polar region highest dust density is found during Ls = 270° – 360° and during Ls = 0° – 90°, the dust is comparable.

5.5 Results and discussions

The obtained positive and negative ion densities obtained from the model simulation for the input parameters above are described in the following two subsections.

5.5.1 Positive ions

The source of the ionization considered in the modelling for lower ionosphere is galactic cosmic ray flux. The major positive ions found in the lower Martian ionosphere are $H_3O^+(H_2O)_2$, $H_3O^+(H_2O)_3$, $H_3O^+(H_2O)_4$, and $H_3O^+H_2O$. Initially, CO_2^+ and O_2^+ are produced in the lower atmosphere which then go through the chemical scheme described in Sheel and Haider (2012) (and as given in Chapter 2) and eventually are converted to hydronium ions H_3O^+. The hydronium ion is removed almost immediately in the lower altitudes majorly through the three body reaction resulting in hydronium hydrated ions of higher orders.

Below we discuss the seasonal variation of the important ion densities over the regions divided as low (0°-30°), mid (30°-60°) and high or polar latitudes (60°-90°). The seasonal variability is studied for four seasons: Ls = 0° – 90°, Ls = 90° – 180°, Ls = 180° – 270° and Ls = 270° – 360°. H_3O^+ is the primary precursor for the major hydrated positive ions in the Martian atmosphere. In Figure 5.6 we show the seasonal variation of H_3O^+over the regions of our investigation. The ion density is negligible in the atmosphere below

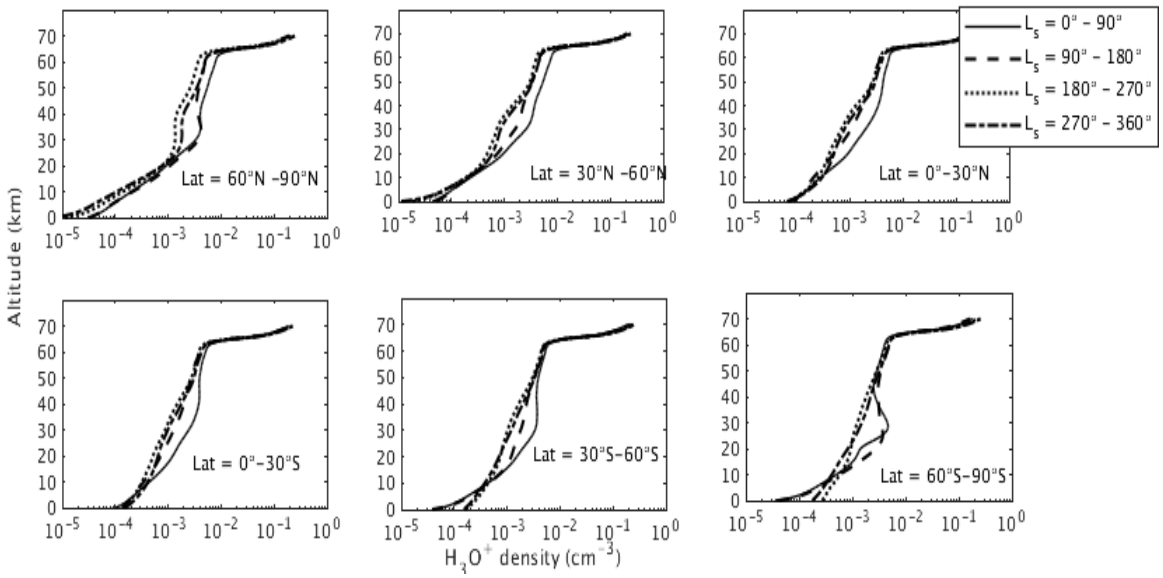

Figure 5.6: Seasonal variation of ion H_3O^+ over low, mid and high latitude during MY 27.

60 km (Figure 5.6). Over the northern polar and mid-latitude, the seasonal variation can be seen in the altitudes between 30 and 60 km where ion density is higher during Ls = 0° – 90° and Ls = 90° – 180° when water vapour in these altitudes decreases due to saturation occurring at lower height (as discussed in Chapter 4). A similar phenomenon can be seen over both the low latitude regions and southern mid-latitude region, only during Ls = 0° – 90°. Over the southern polar region, the effect can be seen in both autumn and summer. Therefore, the density of H_3O^+ is anti-correlated with the amount of water vapour present in the atmosphere at higher altitudes.

Figure 5.7 shows the seasonal variation of the ion, $H_3O^+H_2O$, obtained over each region of study. The minimum density of the ion is found near the surface. The vertical profiles, in general show increase in number density from 10^{-2} cm^{-3}at the surface to 10^2 cm^{-3}at 70 km. Over the northern high and mid-latitudes, the ion density is maximum when water vapour is high during Ls = 0° – 90° and dust in the atmosphere is minimum in the low altitudes. In the next season, during Ls = 90° – 180° when both water vapour and dust increases in the atmosphere, the ion density decreases. In the other two seasons water

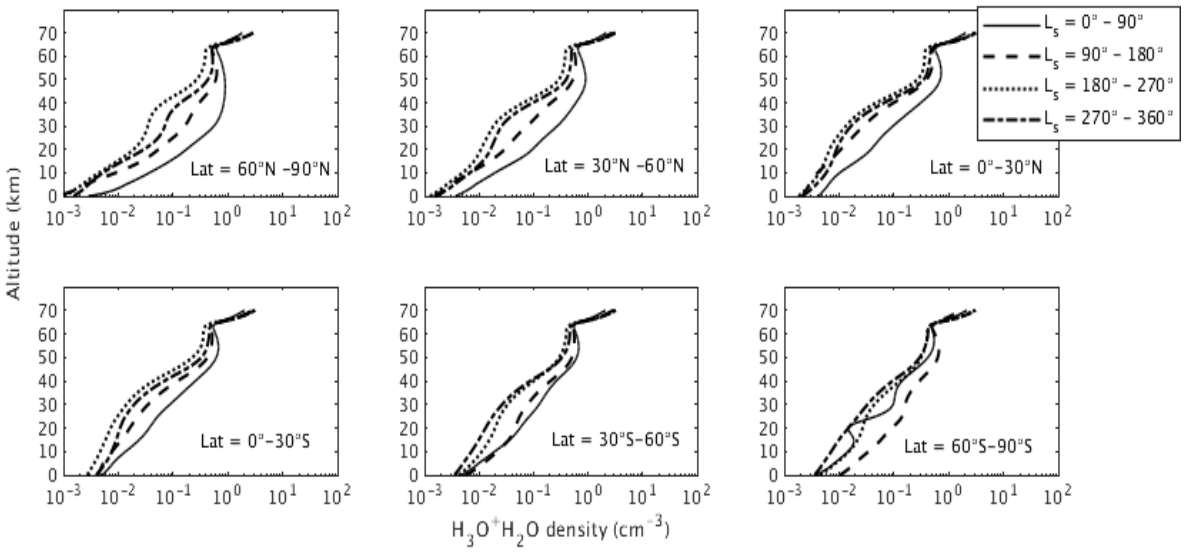

Figure 5.7: Seasonal variation of ion $H_3O^+H_2O$ over low, mid and high latitude during MY 27.

vapour decreases by orders of magnitude and dust density becomes higher by only a factor of about 2.5, over these regions. Due to this large decrease in water vapour, the ion density decreases by few factor in the near surface altitudes. Over the low latitude region seasonal variability of the ion density is not as significant, due to low seasonal variability of water vapour. However, the surface densities are comparable throughout the year and in the higher altitudes the ion density decreases in the season Ls = 180° – 270° when hygropause rises to higher altitudes compared to the season Ls = 0° – 90°. The effect of hygropause rise in the ion density is seen to be the most dominant over the northern polar region. When hygropause rises, the H_2O density increases in the altitudes above 10 km. Due to increase in water vapour in the higher altitudes, the lower order hydrated ions reacts and produce higher order hydrated ions. Over the southern mid-latitudes ion densities are comparable during Ls = 0° – 90° and Ls = 90° – 180° and minimum density is calculated when dust density is highest, i.e, during Ls = 270° – 360°. However, in the south polar region, highest density occurs during Ls = 90° – 180° when dust density is low.

The seasonal variation of the density of the second order hydronium hydrated ion, $H_3O^+(H_2O)_2$ is shown in Figure 5.8. Over northern polar and mid-latitudes, ion density is highest during Ls = 0° – 90° when dust is minimum, while the ion density decreases by a

factor of 2–3 during Ls = 90º – 180º due to increase in dust density. In the season Ls = 90º – 180º, though density of H_2O is maximum in the lower altitudes, the effect of increase in dust density destroys the ions which results in a reduced ion density. During Ls = 180º – 360º the ion density decreases to negligible values over polar region and by one order over the mid-latitude region due to scarcity of water vapour. This decrease is attributed to the water vapour since the increases in dust density during Ls = 270º – 360º is only by a factor 1.5. Over the low latitude regions a similar seasonal trend is seen though the seasonal variability is weaker than seasonal variability over northern polar and mid-latitude. Over the southern polar region, the highest ion density is seen during southern summer (Ls = 180º – 270º) due to high water vapour. The density is comparable during Ls = 270º – 360º. During southern winter the ion density decreases by orders of magnitude. Over the southern mid-latitude, similar seasonal trend is seen in the lower altitudes and in the higher altitudes the seasonal variation in the ion density increases compared to the seasonal variability in the lower altitudes. In the altitudes greater than

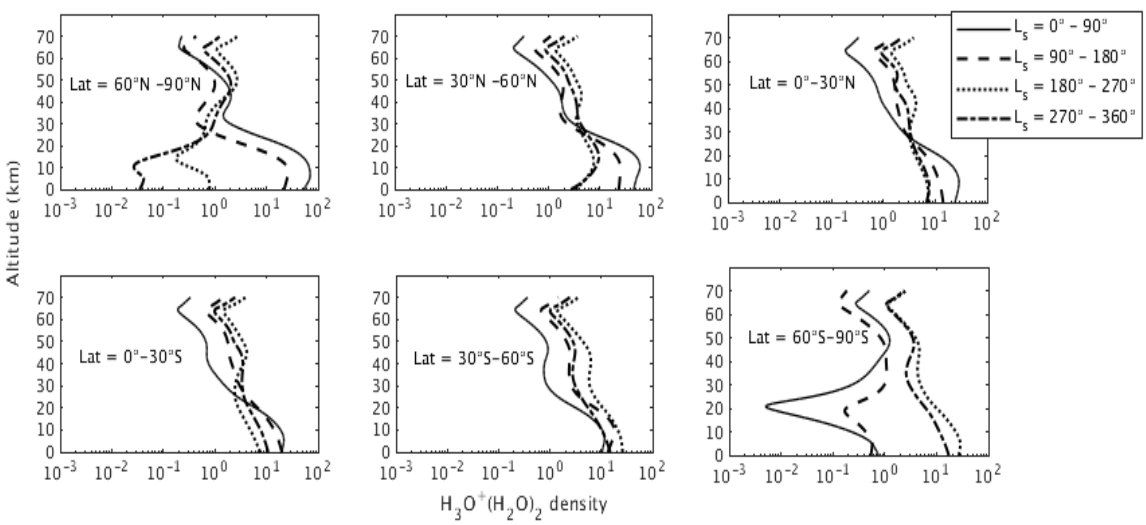

Figure 5.8: Seasonal variation of ion $H_3O^+(H_2O)_2$ over low, mid and high latitude during MY 27.

30 km, the ion density is highest during Ls = 180º – 360º, regardless of the region and lowest density is seen during Ls = 0º – 90º over the entire globe except over polar region which is an effect of decrease in water vapour density during the season.

Over the northern polar and mid-latitude region, maximum densities of the ion $H_3O^+(H_2O)_3$ are found during Ls = 0º – 90º and Ls = 90º – 180º (Figure 5.9). The surface densities are ~ 10^2 cm^{-3} which decreases to negligible values above 20 km. In these two

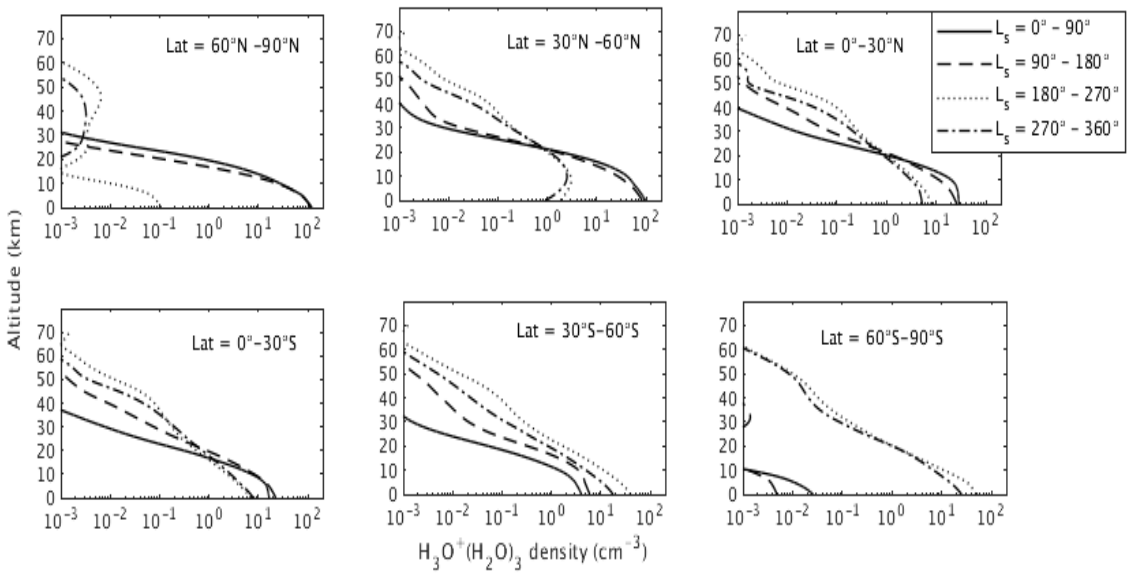

Figure 5.9: Seasonal variation of ion $H_3O^+(H_2O)_3$ over low, mid and high latitude during MY 27.

seasons the ion densities are fairly comparable. During winter (Ls = 270º – 360º) and autumn (Ls = 180º – 270º), ion densities become negligible over the polar region and over the mid-latitude region, the ion density decreases to few cm^{-3} near the surface.

Over the low latitude regions, the ion density is ~ few tens of cm^{-3} during Ls = 0º – 180º. During Ls = 180º – 360º, the surface ion density decreases to values < 10 cm^{-3}. The rate of decrease falls with altitude as hygropause rises in these seasons which increases the density of H_2O in the altitudes. Over the southern polar and mid-latitudes, the maximum ion density is found during Ls = 180º – 270º and the density during Ls = 270º – 360º is comparable. However, during winter (Ls = 90º – 180º), the ion density over southern mid-latitudes decreases by an order and over southern polar region, the ion density becomes negligible due to scarcity of water vapour.

Thus we have seen that water vapour and dust have competing effects on the densities of the hydrated hydronium ions. The lower order ions such as H_3O^+, $H_3O^+H_2O$ do not show significant seasonal variation. In the altitudes between 30 km and 40 km, seasonal variation in these ions becomes noticeable. During Ls = 180° – 360°, when water vapour increases in the upper heights due to the rise in hygropause, the loss in these ions increases which results in lower density compared to the densities obtained in seasons Ls = 90° – 180°. The density of $H_3O^+H_2O$ over low latitude region during Ls = 0° – 90° for low dust density is comparable with the study of Sheel and Haider (2016) in low dust scenario. However, our analysis shows the seasonal variation discussed above due to water vapour densities. The higher order ions such as $H_3O^+(H_2O)_2$ and $H_3O^+(H_2O)_3$ shows positive correlation with H_2O in presence of dust. In the low dust scenarios, the ion density over northern polar region during northern summer is higher by a factor of 4 compared to the ion densities compared over the southern polar region during southern summer. The positive correlation is also visible in the higher altitudes, where ion density increases due to rise in hygropause during seasons Ls = 180° – 360°.

5.5.2 Negative ions

Negative ions in the Martian lower atmosphere form initially due to the electrons captured by the highly electron affinitive neutrals O, O_2 and O_3 leading to formation of ions O^-, O_2^- and O_3^-. These ions then undergo a series of chemical reactions and result in major negative ions such as CO_4^-, CO_3^-, NO_2^- and their hydrated ions $CO_3^-H_2O$, $CO_3^-(H_2O)_2$, and $NO_2^-H_2O$. Other ions such as O^-, O_2^-, O_3^- and $NO_3^-(H_2O)_2$ are insignificant compared to the major ions. Below we discuss the seasonal and latitudinal variation of the major negative ions.

CO_4^- ion is produced in the three body reaction of O_2^-, CO_2 and a third molecule and is mostly destroyed by the presence of odd oxygen O_x ($O+O_3$). Over the high and mid northern latitude regions maximum ion density is calculated during Ls = 90° – 180° which is reduced by a factor of 5 – 10 during Ls = 0°-90° when dust density decreases in the atmosphere compared to the density during Ls = 90°-180° (Figure 5.10). A peak in the ion

density occurs in different heights for different seasons as a results of loss of ions near surface. During Ls = 90° – 180°, peak density occurs between 8 and 10 km and during Ls = 0° – 90°, the peak occurs at 15 km over Lat = 60°N – 90°N and at 21 km over Lat = 30°N – 60°N. In the other two seasons viz Ls = 180° – 270° and 270° – 360° when water vapour is low, the ion density decreases and peak occurs at greater heights.

Over the low latitude regions, the densities are comparable throughout the year. During Ls = 0° – 180° the ion density peak occurs at lower altitudes than during Ls = 180° – 360°. Over the southern polar and mid-latitudes, the peak density is maximum during Ls = 180° – 360° and during winter, the density reduces by orders and becomes negligible. In the southern winter season, the ion density becomes negligible.

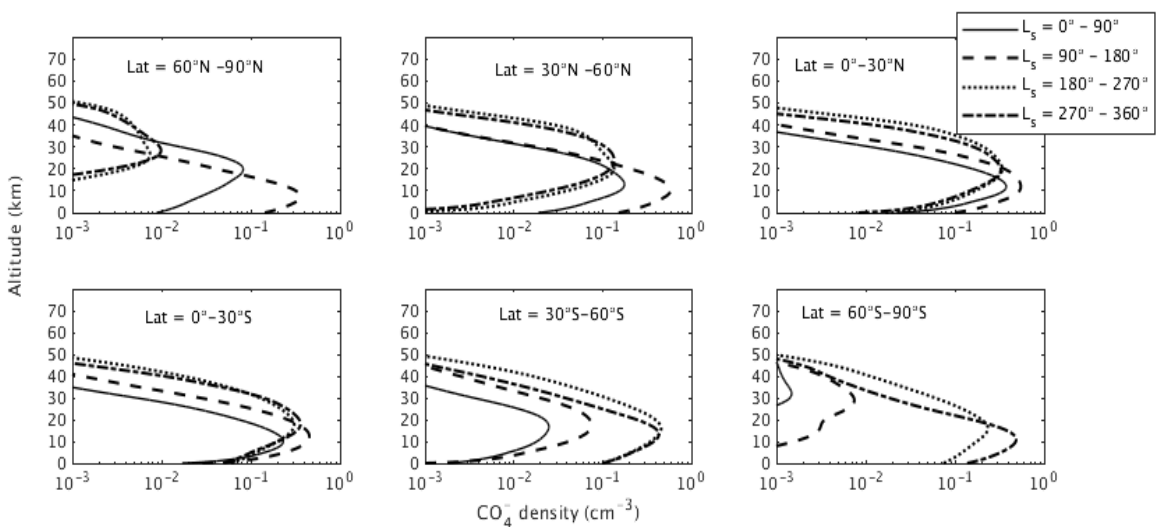

Figure 5.10: Seasonal variation of ion CO_4^- over low, mid and high latitude during MY 27.

The seasonal variation of the ion density $CO_3^-H_2O$ is shown in Figure 5.11. Over polar and mid northern latitude regions during Ls – 0° – 90°, the ion density is calculated maximum when northern polar region is cold due to aphelion and hygropause occurs below 10 km. A peak occurs at 20 km over these latitudes and in these altitudes the water vapour amount is reduced due to saturation. Over the polar region, the density decreases near the surface whereas over the mid-latitude the maximum density is calculated near the surface. During Ls = 90° – 180°, similar ion density profiles are obtained, though over

polar region the near surface ion density exceeds the peak value of the ion density. During Ls = 180º – 360º, near surface densities become negligible and the peak occurs at a higher altitude (~ 25 km). Over the southern and northern low latitudes, the ion densities are comparable for all the seasons throughout the year. The maximum density occurs near the surface and the peak occurs at 20 km during Ls = 0º – 90º which shifts to higher altitude during Ls = 180º – 270º due to increase in water vapour in the altitudes.

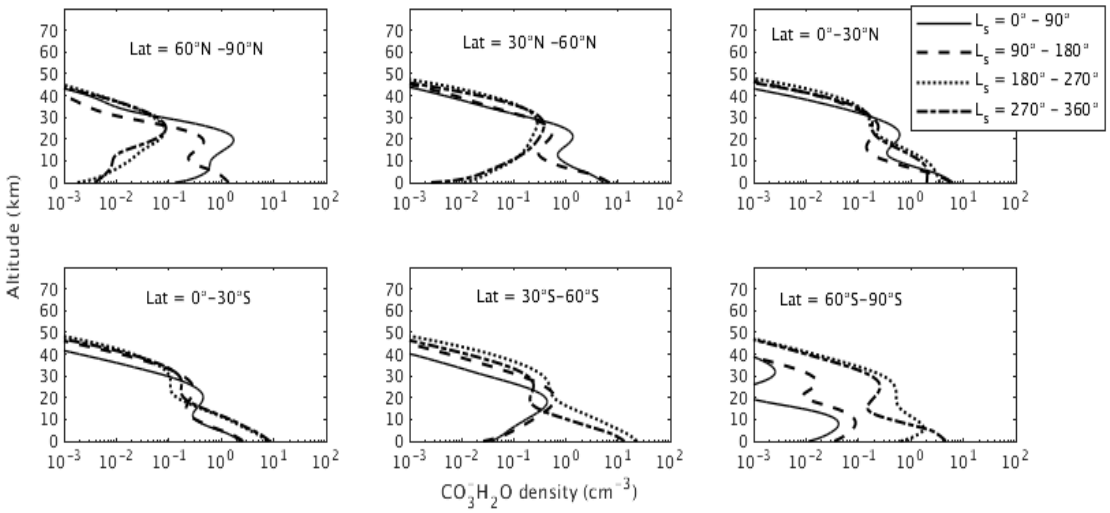

Figure 5.11: Seasonal variation of ion $CO_3^-H_2O$ over low, mid and high latitude during MY 27.

Over the southern mid and high latitude the maximum ion density occurs during Ls = 180º – 270º. The ion densities are ~ 10 cm^{-3} near the surface and attains a peak at 27 km of relatively smaller value. During Ls = 0º – 90º, the ion density becomes negligible over the polar and mid-latitude region. However, a peak density of 0.5 cm^{-3} occurs over the mid-latitudes during this season.

The ion $CO_3^-H_2O$ is sensitive to water vapour due to its production process which involves H_2O and requires a third molecule presence. Water vapour also act as a loss agent for this ion. However the production dominates in the lower altitudes where third body reactions are more favoured than the loss process. The loss dominates in the altitudes above 10 km where the probability of third body reaction has reduced. Above, hygropause the water vapour density decreases which increases the ion density resulting in a peak.

The Figure 5.12 shows the seasonal variation in density of $CO_3^-(H_2O)_2$ over the high, mid and low latitude regions. Over the northern and southern polar regions, highest density of the ion $CO_3^-(H_2O)_2$ occurs (Figure 5.12) near the surface during respective summer seasons. Over the southern polar region, the ion density is few tens cm^{-3} whereas over the northern polar region the density can reach few hundred near the surface. This difference in the ion density comes from the available water vapour density. Over the northern mid-latitude and both the low latitude regions highest densities are achieved during Ls = 0° – 90° and a comparable density occurs during Ls = 90° – 180°. However, in later half of the year, the surface ion density decreases to a few cm^{-3} only. Over the

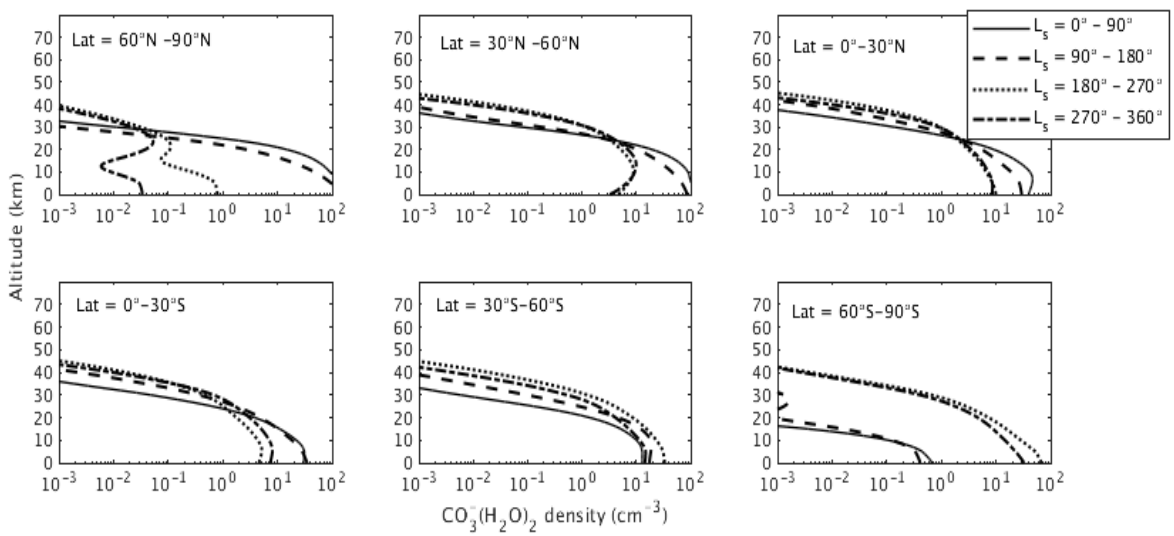

Figure 5.12: Seasonal variation of ion $CO_3^-(H_2O)_2$ over low, mid and high latitude during MY 27.

southern mid-latitudes, the ion densities are comparable throughout the year and the maximum occurs during Ls = 180° – 270°.

Figure 5.13 shows the seasonal variation in the density of ion $NO_2^-H_2O$. Over polar, mid and low northern latitudes, maximum density of the ion, $NO_2^-H_2O$ is found during Ls = 0° – 90°, i.e, during northern spring when water vapour in the atmosphere is low. A peak in the ion density occurs at around 20 km. The value of this peak is highest over the polar region and decreases towards low latitudes. The surface-values in this season is higher

than the peak value over the mid and low latitudes. However, over northern polar region, the surface value is ~0.1 cm^{-3} whereas the peak value is 10-20 times larger.

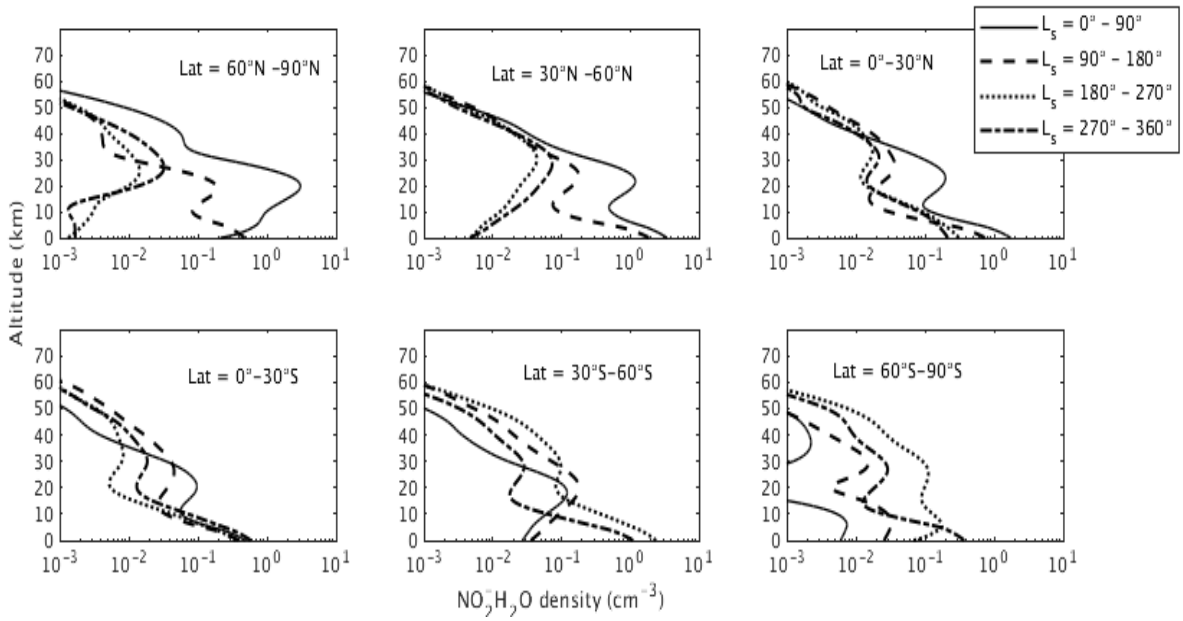

Figure 5.13 Seasonal variation of ion $NO_2^-H_2O$ over low, mid and high latitude during MY 27.

During Ls = 90° – 180°, similar kind of vertical profile is calculated over mid and low latitudes whereas over polar region, the surface ion density is higher than the high altitude peak ion density. In the low latitude regions structure of the ion density profile does not vary with seasons. However, the peak occurs at a higher altitude during Ls = 180° – 270° and the peak density decreases. The ion densities near the surface remain comparable throughout the year over these regions.

In the mid and high southern latitudes maximum ion density is calculated near surface and reaches up to 2 cm^{-3} and a peak of 0.1cm^{-3} occurs at around 30 km. The ion density profile is somewhat similar during Ls = 270° – 360°. During Ls = 0° – 90° ion density over these regions becomes negligible. In the both low latitude regions the profile structure does not vary much with seasons. However, the peak occurs at a higher altitude during Ls =180° – 270° compared to the peak during Ls = 0° – 90°. The surface values remains comparable throughout the year.

The vertical profile of the ion density $NO_3^-H_2O$ resembles the vertical structure of the ion $CO_3^-H_2O$. In the Martian atmosphere the ion $NO_3^-H_2O$ is produced by the ion $CO_3^-H_2O$. Other production processes are negligible in comparison and thus the resemblance. Therefore similar dependence on water vapour for the ion $NO_3^-H_2O$ existed in the Mars. The hydrated ions $CO_3^-H_2O$ depends on the density of its precursors CO_3^- and H_2O. The abundance of CO_3^- again depends on odd oxygen ($O+O_3$). Therefore the shape of the vertical profile is determined by the profiles of water vapour and O_x. For example over northern hemisphere when water vapour near surface increases, the ion density also increases and the high altitude peak is most strong when the odd O_x peak is strong. The dependence of the seasonal behaviour on dust is only noticeable near the surface. The higher order ion $CO_3^-(H_2O)_2$ is positively correlated with water vapour, thus the ion is maximum during summer. In MY 27 dust may affect the ion density by a factor of 1-2. The dependence of these hydrated ions on the water vapour density is profoundly seen over the polar regions.

The non-hydrated ion such as CO_4^- is indirectly linked with water vapour. Since it is mostly lost by odd O_x, increase in water vapour in the atmosphere facilitates the increase of the ion. During polar winter when ozone in the lower altitudes increases and become maximum over the respective regions, the ion density becomes minimum. The production rate of $NO_2^-H_2O$ is maximum due to the reaction $CO_3^-H_2O$ and NO (Sheel and Haider, 2012). In our analysis, the ion shows the dependence over the amount of $CO_3^-H_2O$ in the atmosphere.

5.6 Summary and Conclusion

We have studied, the seasonal variation in ion densities for MY27 at different latitudes, which was one of the objectives of the thesis. The study has improved our understanding of the lower ionosphere in terms of its response to the seasonal variation of dust and neutrals. In MY27, dust optical depth varied from 0.1 to 0.5 (Smith, 2009). In these dust scenarios, the role of water vapour and odd O_x becomes important in order to determine the seasonal variation in the ion densities. The lower order hydrated hydronium

ions (H_3O^+, $H_3O^+H_2O$) do not show much variation in the low altitudes despite the variation in dust and water vapour whereas in the high altitudes loss due to water vapour introduces seasonal variations. Higher order hydrated hydronium ions ($H_3O^+(H_2O)_2$ and $H_3O^+(H_2O)_3$) are positively correlated with the water vapour present in the atmosphere as they increase during summer and decrease in winter. Presence of dust decreases the density of hydronium ions due to their loss through ion-dust attachment, as found earlier by Haider et al (2010) and Sheel and Haider (2016). Odd oxygen plays an important role in determining the densities of CO_4^- and $CO_3^-H_2O$. The ion CO_4^- seems to be dependent on the amount of ozone and atomic oxygen present in the atmosphere. Odd oxygen is anti-correlated with water vapour in Martian atmosphere (as discussed in Chapter 4) which thus establishes a correlation of ion density with water vapour. $CO_3^-H_2O$ depends on water vapour in the atmosphere. The peak in the $CO_3^-H_2O$ is a result of the increased ozone. The density of the ions in the D layer of the ionosphere varies by orders over the high latitudes and the seasonal variation is comparatively weak in the low latitude regions.

Chapter 6

Summary and Scope for future work

The work presented in this thesis aims to study the seasonal and spatial variations of the trace neutral constituents and the ions of the lower atmosphere of Mars. A study of this kind which has not been done before, has been made possible through the photochemistry coupled LMD-GCM, the PRL ion-dust model and observations from the SPICAM instrument onboard the European Mars Express spacecraft. In this chapter, we present a summary of the work done highlighting the important results obtained. We also suggest future directions in which we would like to continue the investigation of the neutral photochemistry of the Martian atmosphere.

6.1 Summary

In the beginning of the thesis, we give a general introduction to the Martian atmosphere in chapter 1, comparing it with Earth's atmosphere which is more familiar to the general scientific community. The concept of seasons on Mars is introduced and the general trend of atmospheric temperature and pressure are discussed. The neutral and ion composition of the atmosphere is briefly described and finally the objective of the thesis is presented. The methodology used to fulfill the objectives of the thesis forms the content of chapter 2, where we describe the models used and the mechanism to retrieve ozone and dust from SPICAM. In chapter 3 we give an overview of the thermal structure of the Martian atmosphere and that of the major and a few minor gaseous constituents, as simulated by the LMD-GCM. This is used as an input for the work presented in subsequent

chapters. The spatio-temporal variability of odd oxygen species (O and O_3), their competing loss mechanisms and their relation with water vapour and dust is discussed in chapter 4. The three-dimensional structure of the neutral atmosphere simulated by the GCM is used as an input to the PRL ion-dust model, to study the seasonal and latitudinal variation of the lower ionosphere of Mars in chapter 5.

6.2 Major results of the study

The major results of the thesis work obtained from the model and observations (retrieval) are listed below.

6.2.1 Temperature and neutral species simulated by GCM

The photochemistry coupled LMD-GCM is used to simulate the neutral constituents and temperature of the Martian atmosphere for the MY 27. The seasonal variability of these neutrals and temperature have been described in Chapter 3. Below we summarize the important results obtained from our simulation.

1. Over the equatorial region, seasonal variation in the daytime temperature is in the range180 – 220 ^{o}K. Over the southern high latitude (pole-ward of 50°S), the temperature varies within 190 – 210 ^{o}K. However, over the northern hemisphere strongest variation in diurnal temperature is noticed. High temperature (~ 220K) are obtained during Ls = 90° for all the northern latitudes. A minimum surface temperature of 148 ^{o}K is calculated during Ls = 225° - 315°. The strong temperature variation is reflected in the strong variation in the vertical distribution of the water vapour as well in the columnar amount.
2. The temperature structure shows the occurrence of polar warming and polar vortex which matches the observational results qualitatively.
3. The water cycle established in the model produces satisfactory result for the entire globe except for the southern polar region. The water vapour amount calculated during southern summer is 40 pr-µm, which is much higher than the observed values recorded by TES onboard MGS.

4. The observed distribution of ozone is well reproduced by the model as described in Chapter 3. The seasonal variation over the equatorial region is captured by the GCM as well.

6.2.2 Spatio-temporal variability of odd oxygen species

Though the atmospheric components such as O, HO_2, OH, and H are present in trace amounts, they play an important role in the stability of the Martian atmosphere, and are also sinks for ozone. The study of these competing loss processes of odd oxygen O_x (O and O_3) and the variability of ozone and dust (chapter 4) led to the following results:

1. Variation in the rates of the loss mechanisms are a consequence of the seasonal variation of the H_2O content in the atmosphere. The effect of vertical distribution is more pronounced than the columnar amount. For example, during aphelion season though H_2O is high over the northern hemisphere, due to low temperature water vapour density is less compared to the perihelion season and thus the destruction of odd oxygen is mostly bound in the lower altitudes (< 10 km).
2. The losses of odd oxygen due to reactions such as O+O, or O+O_3 are high during aphelion season, peaking in the region 30 – 45 km. During perihelion season, these losses become comparatively negligible. During night, the loss rates become negligible in the lower altitudes due to less availability of O. However, similar seasonal variations are seen in the high altitudes above ~ 30 – 45 km.
3. The reaction H+O_3 is the most dominant loss mechanisms for ozone and second dominant loss for O_x after HO_2+O. The loss due to H+O_3, shows similar behaviour as the loss rates O+O, or O+O_3 during aphelion while during perihelion, the loss rate is only significant near the surface.
4. The loss rate HO_2+O is the most dominant loss of odd oxygen in Martian atmosphere. However, it does not show significant seasonal variability below 45 km. Above 45 km the loss rate decreases during aphelion season compared to the perihelion season.

5. The O_x is found to be in photochemical equilibrium up to about 30 km in the aphelion season, and up to 45 km in the perihelion season. In the domain of photochemical equilibrium, the HO_2 + O reaction is by far the dominant loss process of O_x. Above the domain of photochemical equilibrium, the HO_x+O, H+O_3 and O+O reactions have comparable contributions to the O_x loss. The O+O_3 reaction is always a minor contribution to the O_x loss.
6. Ozone, retrieved from radiance measurements by the SPICAM UV spectrometer onboard Mars Express, shows seasonal variability indicating anti-correlation with water vapour and conforming the our simulated results.
7. Retrieved dust values are successful to produce the regional and seasonal dust storms.

   We have also found that during dust storms, ozone columnar amounts increase with increase in dust optical depth due to radiative impact of dust. The increase of ozone can be as high as 50% of the ozone without global dust storm. A similar result can be seen in ozone simulated by the LMD-GCM for the dark dust storm of MY 28. This increase in ozone column is a consequence of the dust scattering where due to heavy dust loading, solar UV cannot penetrate deep in the atmosphere thus reducing the photolysis of water vapour (responsible for the production of HO_x radicals) and ozone.
8. We have also studied the dynamical effect on the ozone column due to dynamics using CO as a dynamical tracers. Over southern polar regions our calculations of ozone column shows an increase of 24 µm-atm obtained by the 3D LMD-GCM than the ozone column calculated by one-dimensional model using the same chemistry.

6.2.3 Martian lower ionosphere

Martian lower ionosphere contains major positive ions such as $H_3O^{+(}H_2O)_2$, $H_3O^{+(}H_2O)_3$, $H_3O^+(H_2O)_4$, and $H_3O^+H_2O$ and major negative ions such as CO_4^- $CO_3^-H_2O$, CO_3^- $(H_2O)_2$, and $NO_2^-H_2O$. The existence of the D region of the Martian ionosphere

depends on the density of these major ions. The densities of these ions are calculated using PRL ion-dust model which is described in chapter 2 and chapter 5. The densities of these ions are found to be dependent mostly on water vapour in a year without global dust storm, while variation of other neutral components of the atmosphere do not show significant effect on the ion densities. The important results obtained in the study are listed below.

1. Lower order positive ions (H_3O^+ and $H_3O^+H_2O$) do not show seasonal variation in the lower altitudes (< 20 km). The effect of seasonal variation in water vapour is seen in the ion densities above 30 km. Due rise and descend of the hygropause, the ion density changes. In the altitudes above 30 km water vapour acts as a loss agent for these ions.
2. The densities of the higher order hydrated hydronium ions ($H_3O^{+(}H_2O)_2$, $H_3O^{+(}H_2O)_3$) are determined by the competing effect of dust and water vapour. In a clear atmosphere the ion densities increases with increase in water vapour. However, the ion densities are seen to decrease during northern summer when water vapour was highest compared to the ion densities calculated during aphelion. During aphelion season dust number density was less by factors compared to the dust density during summer.
3. The density of ion CO_4^- is dependent on odd oxygen. Odd oxygen act as a loss agent for CO_4^-. The ion decreases with increase of odd O_x density in the atmosphere. The hydrated ions such as $CO_3^-H_2O$ and $CO_3^-(H_2O)_2$ are correlated with water vapour. Density of the ion $NO_2^-H_2O$ depends on its precursor CO_3^- H_2O.

6.3 Scope for future work

As discussed in one of our results obtained from the retrieval of dust and ozone, dust affects the abundance of ozone. This effect seen from the observations and described in chapter 4, indicates towards the increase in ozone in global dust storm due to a radiative feedback, where the suspended dust inhibits the incoming solar radiation. The chemical effect of dust on ozone has been observed in the Earth's atmosphere where it destroys

tropospheric ozone (Reus et al., 2005). During dust storms over Sahara desert, it has been observed through in-situ measurement that the mixing ratios of O_3, H_2O_2 and NO_x are strongly reduced (Reus et al., 2005). In the current version of LMD-GCM, the effect of heterogeneous chemistry has only been calculated for catalytic species such as HO_2 and OH which are destroyed on the dust surface. This destruction of HO_x indirectly affect the odd oxygen chemistry. Such a scheme for ozone loss with dust, has yet not been incorporated in the GCM. This is an area, where future work can be done.

The current version of the GCM does not include sulphur chemistry. The observations of SO_2 (Encrenaz et al., 2011) do not support the calculation of the density of SO_2 assuming volcanic origin in one dimensional models (Wong et al., 2003). Therefore, inclusion of heterogeneous chemistry along with sulphur chemistry in LMD-GCM may impact the current understanding of the odd oxygen chemistry and agreement of modelled SO_2 may improve with the observed values.

Despite repeated observations of methane (CH_4) in the Martian atmosphere, our knowledge of the distribution of this trace species in the atmosphere has still not reached a mature stage. This void can be filled by including CH_4 in the photochemistry of the GCM with its current knowledge of source and sinks, and compare it with observations to arrive at a meaningful methane distribution and seasonal variability.

References

Anderson, E., and C. Leovy (1978), Mariner 9 television limb observations of dust and ice hazes on Mars, *Journal of the Atmospheric Sciences*, 35 (4), 723–734.

Atreya, S., and Z. Gu (1995), Photochemistry and stability of the atmosphere of Mars, *Advances in Space Research*, 16 (6), 57–68.

Barker, E. (1972), Detection of molecular oxygen in the Martian atmosphere, *Nature*, 238 (5365), 447.

Barker, E. S., R. A. Schorn, A. Woszczyk, R. G. Tull, and S. J. Little (1970), Mars: Detection of atmospheric water vapor during the southern hemisphere spring and summer season, *Science*, 170 (3964), 1308 – 1310.

Barth, C., W. Fastie, C. Hord, J. Pearce, K. Kelly, A. Stewart, G. Thomas, G. Anderson, and O. Raper (1969), Mariner 6: Ultraviolet spectrum of Mars upper atmosphere, *Science*,165 (3897), 1004–1005.

Barth, C. A., and C. W. Hord (1971), Mariner ultraviolet spectrometer: Topography and polar cap, *Science*, 173 (3993), 197–201.

Barth, C. A., C. W. Hord, A. I. Stewart, A. L. Lane, M. L. Dick, and G. P. Anderson (1973),Mariner 9 ultraviolet spectrometer experiment: Seasonal variation of ozone on Mars, *Science*,179 (4075), 795–796.

Belton, M. J., and D. M. Hunten (1968), A search for O_2 on Mars and Venus: A possible detection of oxygen in the atmosphere of Mars, *The Astrophysical Journal*, 153, 963.

Bertaux, J. L., O. Korablev, S. Perrier, E. Quemerais, F. Montmessin, F. Leblanc, and A. Fedorova (2006), SPICAM on Mars Express: Observing modes and overview of UV spectrometer data and scientific results., *Journal of Geophysical Research.: Planets*, *111* (E10).

Benna, M., P. Mahaffy, J. Grebowsky, J. L. Fox, R. V. Yelle, and B. M. Jakosky (2015), First measurements of composition and dynamics of the Martian ionosphere by MAVEN's neutral gas and ion mass spectrometer, *Geophysical Research Letter.*, 42 (21), 8958 – 8965.

Böttger, H., S. Lewis, P. Read, and F. Forget (2005), The effects of the Martian regolith on GCM water cycle simulations, *Icarus*, 177 (1), 174–189.

Bougher, S., R. Dickinson, R. Roble, and E. Ridley (1988), Mars thermospheric general circulation model: Calculations for the arrival of Phobos at Mars, *Geophysical research letters*, 15 (13), 1511–1514.

Bougher, S. W., S. Engel, D. P. Hinson, and J. M. Forbes (2001), Mars global surveyor radio science electron density profiles: Neutral atmosphere implications, *Geophysical Research Letters*, 28 (16), 3091–3094.

Bougher, S. W., S. Engel, D. Hinson, and J. Murphy (2004), MGS radio science electron density profiles: Interannual variability and implications for the Martian neutral atmosphere, *Journal of Geophysical Research: Planets*, 109 (E3).

Brasseur, G. P., and S. Solomon (2005), Aeronomy of the Middle Atmosphere: Chemistry and Physics of the Stratosphere and Mesosphere, *Atmospheric and Oceanographic Sciences Library*, vol. 32, 3rd ed., p. 646, Springer, Netherlands.

Chaffin, M., J. Deighan, N. Schneider, and A. Stewart (2017), Elevated atmospheric escape of atomic hydrogen from Mars induced by high-altitude water, *Nature Geoscience*, 10 (3), 174.

Chamberlain, T., H. Cole, R. Dutton, G. Greene, and J. Tillman (1976), Atmospheric measurements on Mars: The Viking meteorology experiment, *Bulletin of the American Meteorological Society*, 57 (9), 1094–1105.

Chassefiére, E., and F. Leblanc (2004), Mars atmospheric escape and evolution; interaction with the solar wind, *Planetary and Space Science*, 52 (11), 1039–1058.

Clancy, R., and H. Nair (1996), Annual (perihelion-aphelion) cycles in the photochemical behavior of the global Mars atmosphere, *Journal of Geophysical Research: Planets*, 101 (E5), 12,785–12,790.

Clancy, R., B. Sandor, M.Wolff, P. Christensen, M. Smith, J. Pearl, B. Conrath, and R. Wilson (2000), An intercomparison of ground-based millimeter, MGS-TES, and Viking atmospheric temperature measurements: Seasonal and interannual variability of temperatures and dust loading in the global Mars atmosphere, *Journal of Geophysical Research: Planets*, 105 (E4), 9553–9571.

Clancy, R., B. Sandor, and G. Moriarty-Schieven (2004), A measurement of the 362 ghz absorption line of Mars atmospheric H_2O_2, *Icarus*, 168 (1), 116–121.

Clancy, R. T., M. J. Wolff, F. Lefévre, B. A. Cantor, M. C. Malin, and M. D. Smith (2016), Daily global mapping of Mars ozone column abundances with MARCI UV band imaging, *Icarus*, 266, 112–133.

Conrath, B. J. (1975), Thermal structure of the Martian atmosphere duringthe dissipation of the dust storm of 1971, *Icarus*, 24, 36–46.

Ehlmann, B. L., et al. (2008), Orbital identification of carbonate-bearing rocks on Mars, *Science*, 322 (5909), 1828–1832.

Encrenaz, T., et al. (2004), Hydrogen peroxide on Mars: evidence for spatial and seasonal variations, *Icarus*, 170 (2), 424–429.

Encrenaz, T., T. K. Greathouse, M. Richter, J. Lacy, T. Fouchet, B. Bézard, F., F. Forget, and S. Atreya (2011), A stringent upper limit to SO_2 in the Martian atmosphere, *Astronomy & Astrophysics*, 530, A37.

Encrenaz, T., et al. (2015), Seasonal variations of hydrogen peroxide and water vapor on Mars: further indications of heterogeneous chemistry, *Astronomy & Astrophysics*, 578, A127.

Evans, K.F. (1998), The Spherical Harmonics Discrete Ordinate Method for Three-Dimensional Atmospheric Radiative Transfer, *J. Atmos. Sci*., 55, 429–446.

Farmer, C., and P. Doms (1979), Global seasonal variation of water vapor on Mars and the implications for permafrost, *Journal of Geophysical Research: Solid Earth*, 84 (B6), 2881–2888.

Farmer, C., D. Davies, A. Holland, D. LaPorte, and P. Doms (1977), Mars: Water vapour observations from the Viking orbiters, *Journal of Geophysical Research*, 82 (28), 4225–4248.

Fast, K., T. Kostiuk, T. Hewagama, M. F. A'Hearn, T. A. Livengood, S. Lebonnois, and F. Lefévre (2006), Ozone abundance on Mars from infrared heterodyne spectra: Validating photochemical models, *Icarus*, 183 (2), 396–402.

Fedorova, A., O. Korablev, J.-L. Bertaux, A. Rodin, A. Kiselev, and S. Perrier (2006), Mars water vapor abundance from SPICAM IR spectrometer: Seasonal and geographic distributions, *Journal of Geophysical Research: Planets*, 111 (E9).

Forget, F., and R. T. Pierrehumbert (1997), Warming early Mars with carbon dioxide clouds that scatter infrared radiation, *Science*, 278 (5341), 1273–1276.

Forget, F., F. Hourdin, R. Fournier, C. Hourdin, O. Talagrand, M. Collins, S. R. Lewis, P. L.Read, and J.-P. Huot, 1999. Improved general circulation models of the Martian

atmosphere from the surface to above 80 km. *Journal of Geophysical Research: Planets*, 104 (E10), 24,155-24,176.

Formisano, V., S. Atreya, T. Encrenaz, N. Ignatiev, and M. Giuranna (2004), Detection of methane in the atmosphere of Mars, *Science*, 306 (5702), 1758–1761.

Fouchet, T., et al. (2007), Martian water vapor: Mars Express PFS/LW observations, *Icarus*, 190 (1), 32–49.

Fox, J. L., P. Zhou, and S. W. Bougher (1996), The Martian thermosphere/ionosphere at high and low solar activities, Advances in Space Research, 17 (11), 203 - 218.

Fox, J. L. (2004), Response of the Martian thermosphere/ionosphere to enhanced fluxes of solar soft X rays, *Journal of Geophysical Research: Space Physics*, 109 (A11).

Franz, H. B., M. G. Trainer, M. H.Wong, P. R. Mahaffy, S. K. Atreya, H. L. Manning, and J. C.Stern (2015), Reevaluated Martian atmospheric mixing ratios from the mass spectrometer on the curiosity rover, *Planetary and Space Science*, 109, 154–158.

Gierasch, P., and R. Goody (1968), A study of the thermal and dynamical structure of the Martian lower atmosphere, *Planetary and Space Science*, 16 (5), 615–646.

Gifford Jr, F. (1956), The surface-temperature climate of Mars, *The Astrophysical Journal*, 123, 154.

Good, J. C., and F. P. Schloerb (1981), Martian CO abundance from the j= 1→ 0 rotational transition: Evidence for temporal variations, *Icarus*, 47 (2), 166–172.

González-Galindo, F., M. López-Valverde, M. Angelats i Coll, and F. Forget (2005), Extension of a Martian general circulation model to thermospheric altitudes: UV heating and photochemical models, *Journal of Geophysical Research*, 110, E09008.

Gorshelev, V., Serdyuchenko, A., Weber, M., Chehade, W., Burrows, J.P., 2014. High spectral resolution ozone absorption cross-sections – Part 1: measurements, data analysis and comparison with previous measurements around 293 K. *Atmospheric Measurement Technique*. 7, 609–624.

Gurnett, D., et al. (2005), Radar soundings of the ionosphere of Mars, *Science*, 310 (5756), 1929–1933.

Gurnett, D. A., and A. Bhattacharjee (2005), Introduction to plasma physics: with space and laboratory applications, *Cambridge university press*.

Haider, S., V. Sheel, V. Singh, W. Maguire, and G. Molina-Cuberos (2008), Model calculation of production rates, ion and electron densities in the evening troposphere of mars at latitudes 67° N and 62° S: Seasonal variability, *J. of Geophys. Research: Space Physics*, 113 (A8).

Haider, S., M. Abdu, I. Batista, J. Sobral, X. Luan, E. Kallio, W. Maguire, M. Verigin, and V. Singh (2009), D, E, and F layers in the daytime at high-latitude terminator ionosphere of Mars: Comparison with earth's ionosphere using cosmic data, *Journal of Geophysical Research*: Space Physics, 114 (A3).

Haider, S.A., Sheel, V., Smith, M.D., Maguire, W.C., Molina-Cuberos, G.J., (2010). Effect of dust storms on the D region of the Martian ionosphere: atmospheric electricity. *Journal of Geophysical Research* 115, A12336.

Haider, S., and K. Mahajan (2014), Lower and upper ionosphere of Mars, *Space Sci. Rev.*, 182(1–4), 19–84.

Haider, S., I. Batista, M. Abdu, A. Santos, S. Y. Shah, and P. Thirupathaiah (2016), Flare X-ray photochemistry of the e region ionosphere of Mars, *Journal of Geophysical Research*: Space Physics, 121 (7), 6870–6888.

Hanson, W., S. Sanatani, and D. Zuccaro (1977), The Martian ionosphere as observed by the Viking retarding potential analyzers, *Journal of Geophysical Research*, 82 (28), 4351–4363.

Hartogh, P., M. I. Błęcka, C. Jarchow, H. Sagawa, E. Lellouch, M. de Val-Borro, and T. Cavalié (2010), First results on Martian carbon monoxide from Herschel/HIFI observations, *Astronomy & Astrophysics*, *521*, L48.

Heavens, N. G., M. I. Richardson, A. Kleinböhl, D. M. Kass, D. J. McCleese, W. Abdou, J. L. Benson, J. T. Schofield, J. H. Shirley, and P. M. Wolkenberg (2011), The vertical distribution of dust in the Martian atmosphere during northern spring and summer: Observations by the Mars Climate Sounder and analysis of zonal average vertical dust profiles, *Journal of Geophysical Research*.,

Hess, S., R. Henry, C. B. Leovy, J. Ryan, and J. E. Tillman (1977), Meteorological results from the surface of Mars: Viking 1 and 2, *Journal of Geophysical Research*, 82 (28), 4559–4574.

Hess, S., J. Ryan, J. Tillman, R. Henry, and C. Leovy (1980), The annual cycle of pressure on Mars measured by Viking landers 1 and 2, *Geophysical Research Letters*, 7 (3), 197–200.

Hess, S. L., R. M. Henry, and J. E. Tillman (1979), The seasonal variation of atmospheric pressure on Mars as affected by the south polar cap, *Journal of Geophysical Research: Solid Earth*, 84 (B6), 2923–2927.

Hinson, D., M. Smith, and B. Conrath (2004), Comparison of atmospheric temperatures obtained through infrared sounding and radio occultation by Mars global surveyor, *Journal of Geophysical Research: Planets*, 109 (E12).

Holmes, J. A., S. R. Lewis, M. R. Patel, and F. Lefévre (2018), A reanalysis of ozone on Mars from assimilation of SPICAM observations, *Icarus*, 302, 308–318.

Hourdin, F., P. Le Van, F. Forget, and O. Talagrand (1993), Meteorological variability and the annual surface pressure cycle on Mars, *Journal of the Atmospheric Sciences*, 50 (21), 3625–3640.

Izakov, M., and O. Krasitskii (1977), Model of the composition of the Mars atmosphere, *Kosmicheskie Issledovaniia*, 15, 455–469.

Jakosky, B. M., and C. B. Farmer (1982), The seasonal and global behavior of water vapour in the Mars atmosphere: Complete global results of the Viking atmospheric water detector experiment, *Journal of Geophysical Research: Solid Earth*, 87 (B4), 2999–3019.

Jakosky, B. M. (2017), MAVEN observations of the Mars upper atmosphere, ionosphere, and solar wind interactions. *Journal of Geophysical Research: Space Physics*, *122*(9), 9552-9553.

Kahre, M. A., J. R. Murphy, C. E. Newman, R. J. Wilson, B. A. Cantor, M. T. Lemmon, and M. J. Wolff (2017), The Mars dust cycle, *The Atmosphere and Climate of Mars*, 18, 295.

Kakar, R., J. Walters, and W. Wilson (1977), Mars: Microwave detection of carbon monoxide, *Science*, 196 (4294), 1090–1091.

Kaplan, L. D., G. Munch, and H. Spinrad (1964), An analysis of the spectrum of Mars, *Astrophysical Journal*, 139 (1), 1–15.

Kaplan, L. D., J. Connes, and P. Connes (1969), Carbon monoxide in the Martian atmosphere,*The Astrophysical Journal*, 157, L187.

Kass, D., A. Kleinbohl, D. McCleese, J. Schofield, and M. Smith (2016), Interannual similarity in the Martian atmosphere during the dust storm season, *Geophysical Research Letters*,43 (12), 6111–6118.

Kelley, M. (1989), The Earth's Ionosphere, *Elsevier, New York*.

Kliore, A., D. L. Cain, G. S. Levy, V. R. Eshleman, G. Fjeldbo, and F. D. Drake (1965), Occultation experiment: Results of the first direct measurement of Mars's atmosphere and ionosphere, *Science*, 149 (3689), 1243-1248.

Kliore, A.J., et al., 1972. The atmosphere of Mars from Mariner 9 radio occultation measurements. Icarus 17, 484–493.

Kong, T., and M. McElroy (1977), Photochemistry of the Martian atmosphere, *Icarus*, 32 (2), 168–189.

Krasnopolsky, V., and V. Parshev (1979), Ozone and photochemistry of the Martian lower atmosphere, *Planetary and Space Science*, 27 (2), 113–120.

Krasnopolsky, V.A., (1993), Photochemistry of the Martian atmosphere (mean conditions). Icarus 101, 313–332.

Krasnopolsky, V. A., 1995. Uniqueness of a solution of a steady state photochemical problem: Applications to Mars. *Journal of Geophysical Research*, 100, E2, 3263-3276.

Krasnopolsky, V., G. Bjoraker, M. Mumma, and D. Jennings (1997), High-resolution spectroscopy of Mars at 3.7 and 8 µm: A sensitive search for H_2O_2, H_2CO, HCL, and CH_4, and detection of HDO, *Journal of Geophysical Research: Planets*, 102 (E3), 6525–6534.

Krasnopolsky, V. A. (2003), Spectroscopic mapping of Mars CO mixing ratio: Detection of north-south asymmetry, *Journal of Geophysical Research: Planets,* 108 (E2).

Krasnopolsky, V. A. (2005), A sensitive search for SO_2 in the Martian atmosphere: implications for seepage and origin of methane, *Icarus*, 178 (2), 487–492.

Krasnopolsky, V. A. (2015), Variations of carbon monoxide in the Martian lower atmosphere, *Icarus*, 253, 149–155.

Krymskii, A., T. Breus, N. Ness, D. Hinson, and D. Bojkov (2003), Effect of crustal magnetic fields on the near terminator ionosphere at Mars: Comparison of in situ magnetic field measurements with the data of radio science experiments on board Mars global surveyor, *Journal of Geophysical Research: Space Physics*, 108 (A12).

Kuiper, G. P. (1952), The atmospheres of Earth and Planets, *Chicago, U. of Chicago Press Chapter XII*.

Lammer, H., H. Lichtenegger, C. Kolb, I. Ribas, E. Guinan, R. Abart, and S. Bauer (2003), Loss of water from Mars: Implications for the oxidation of the soil, *Icarus*, 165 (1), 9–25.

Lefèvre F, Bertaux JL, Clancy RT, Encrenaz T, Fast K, Forget F, Lebonnois S, Montmessin F and Perrier S. (2008), Heterogeneous chemistry in the atmosphere of Mars, *Nature*, 454(7207), 971-5.

Lefévre, F., and F. Forget (2009), Observed variations of methane on Mars unexplained by known atmospheric chemistry and physics, *Nature*, 460 (7256), 720.

Lefévre, F., S. Lebonnois, F. Montmessin, and F. Forget (2004), Three-dimensional modelling of ozone on Mars, *Journal of Geophysical Research: Planets*, 109 (E7).

Lefévre, F., J. L. Bertaux, R. T. Clancy, T. Encrenaz, K. Fast, F. Forget, S. Lebonnois, F. Montmessin, and S. Perrier (2008), Heterogeneous chemistry in the atmosphere of Mars, *Nature*, 454 (7207), 971.

Lefèvre F. and Krasnopolsky V., 2017. Atmospheric photochemistry. In:Robert M. Haberle R. Todd Clancy François Forget Michael D. Smith Richard W. Zurek (Eds.). The Atmosphere and Climate of Mars, chapter 13, Cambridge University Press, pp.405-432.

Leighton, R. B., and B. C. Murray (1966), Behavior of carbon dioxide and other volatiles on Mars, *Science*, 153 (3732), 136–144.

Lemmon, M. T., M. J. Wolff, J. F. Bell III, M. D. Smith, B. A. Cantor, and P. H. Smith (2015), Dust aerosol, clouds, and the atmospheric optical depth record over 5 Mars years of the Mars Exploration Rover mission, *Icarus*, *251*, 96–111.

Lewis, S. R. (2003), Modelling the Martian atmosphere, *Astronomy & Geophysics*, 44 (4), 4–6.

Lindner, B. L. (1988), Ozone on Mars: The effects of clouds and airborne dust, *Planetary and Space Science*, 36 (2), 125–144.

Liu, S., and T. M. Donahue (1976), The regulation of hydrogen and oxygen escape from Mars, *Icarus*, 28 (2), 231–246.

Lundin, R., et al. (1990), ASPERA/Phobos measurements of the ion outflow from the Martian ionosphere, *Geophysical Research Letters*, 17 (6), 873–876.

Madeleine, J.-B., F. Forget, E. Millour, L. Montabone, and M. Wolff (2011), Revisiting the radiative impact of dust on Mars using the LMD global climate model, *Journal of Geophysical Research: Planets*, 116 (E11).

Maguire, William C. "Martian isotopic ratios and upper limits for possible minor constituents as derived from Mariner 9 infrared spectrometer data." *Icarus* 32.1 (1977): 85-97.

Mahaffy, P. R., M. Benna, M. Elrod, R. V. Yelle, S. W. Bougher, S. W. Stone, and B. M. *Jakosky (2015),* Structure and composition of the neutral upper atmosphere of mars from the MAVEN-NGIMS investigation, *Geophysical Research Letters*, 42 (21), 8951 - 8957.

Maltagliati, L., D. V. Titov, T. Encrenaz, R. Melchiorri, F. Forget, H. U. Keller, and J.-P. Bibring (2011), Annual survey of water vapor behavior from the OMEGA mapping spectrometer onboard Mars Express, *Icarus*, 213 (2), 480–495.

Maltagliati, L., F. Montmessin, O. Korablev, A. Fedorova, F. Forget, A. Maattanen, F. Lefévre, and J.-L. Bertaux (2013), Annual survey of water vapor vertical distribution and water–aerosol coupling in the Martian atmosphere observed by SPICAM/MEX solar occultations, *Icarus*, 223 (2), 942–962.

Malicet, J., Daumont, D., Charbonnier, J., Parisse, C., Chakir, A., Brion, J., (1995), Ozone UV spectroscopy. II. Absorption cross-sections and temperature dependence. *J. Atmos. Chem.* 21, 263–273.

Martin, L. J., and R. W. Zurek (1993), An analysis of the history of dust activity on Mars, *Journal of Geophysical Research: Planets*, 98 (E2), 3221–3246.

McCleese, D., et al. (2010), Structure and dynamics of the Martian lower and middle atmosphere as observed by the Mars climate sounder: Seasonal variations in zonal mean temperature, dust, and water ice aerosols, *Journal of Geophysical Research: Planets*, 115 (E12).

McConnochie, T. H., et al. (2018), Retrieval of water vapor column abundance and aerosol properties from chemcam passive sky spectroscopy, *Icarus*, 307, 294–326.

McDunn, T., S. Bougher, J. Murphy, A. Kleinbohl, F. Forget, and M. Smith (2013), Characterization of middle-atmosphere polar warming at Mars, *Journal of Geophysical Research: Planets*, 118 (2), 161–178.

McElroy, M. B., and T. M. Donahue (1972), Stability of the Martian atmosphere, *Science*, 177 (4053), 986–988.

McElroy, M. B., and D. M. Hunten (1970), Photochemistry of CO_2 in the atmosphere of Mars, *Journal of Geophysical Research*, 75 (7), 1188–1201.

McElroy, M. B., and J. C. McConnell (1971), Dissociation of CO_2 in the Martian atmosphere, *Journal of the Atmospheric Sciences*, 28 (6), 879–884.

Melchiorri, R., et al. (2007), Water vapor mapping on Mars using OMEGA/Mars Express, *Planetary and Space Science*, 55 (3), 333–342.

Mendillo, M., C.-L. Huang, X. Pi, H. Rishbeth, and R. Meier (2005), The global ionospheric asymmetry in total electron content, Journal of atmospheric and solar-terrestrial physics, 67 (15), 1377 – 1387.

Mendillo, M., et al. (2018), Mars initial reference ionosphere (MIRI) model: Updates and validations using MAVEN, MEX, and MRO data sets, *Journal of Geophysical Research: Space Physics*, 123 (7), 5674–5683.

Millour, E., et al. (2015), The Mars climate database (MCD version 5.2), in *European Planetary Science Congress*, vol. 10.

Molina-Cuberos, G. J., H. Lichtenegger, K. Schwingenschuh, J. J. López-Moreno, and R. Rodrigo (2002), Ion-neutral chemistry model of the lower ionosphere of Mars, *Journal of Geophysical Research: Planets*, 107 (E5).

Montabone, L., et al. (2015), Eight-year climatology of dust optical depth on Mars, *Icarus*, 251, 65–95.

Montmessin, F., Forget, F., Rannou, P., Cabane, M., Haberle, R.M., 2004. Origin and role of water ice clouds in the Martian water cycle as inferred from a general circulation model. *Journal of Geophysical Research (Planets)* 109, 10004.

Montmessin, F., O. Korablev, F. Lefèvre, J.-L. Bertaux, A. Fedorova, A. Trokhimovskiy, J.Y. Chaufray, G. Lacombe, A. Reberac, L. Maltagliati, Y. Willame, S. Guslyakova, J.-C. Gérard, A. Stiepen, D. Fussen, N. Mateshvili, A. Määttänen, F. Forget, O. Witasse, F. Leblanc, A.C. Vandaele, E. Marcq, B. Sandel, B. Gondet, N. Schneider, M. Chaffin and N. Chapron (2017), SPICAM on Mars Express: A 10 year in-depth survey of the Martian atmosphere, *Icarus*, 297, 195-216.

Mumma, M. J., G. L. Villanueva, R. E. Novak, T. Hewagama, B. P. Bonev, M. A. DiSanti, A. M. Mandell, and M. D. Smith (2009), Strong release of methane on Mars in northern summer 2003, *Science*, 323 (5917), 1041–1045.

Murchie, S., et al. (2007), Compact Reconnaissance Imaging Spectrometer for Mars (CRISM) on Mars reconnaissance orbiter (MRO), *Journal of Geophysical Research: Planets*, 112 (E5).

Nagy, A., et al. (2004), The plasma environment of Mars, *Space Science Reviews*, 111 (1-2), 33–114.

Nair, H., M. Allen, A. D. Anbar, Y. L. Yung, and R. T. Clancy (1994), A photochemical model of the Martian atmosphere, *Icarus*, 111 (1), 124–150.

Navarro, T., J.-B. Madeleine, F. Forget, A. Spiga, E. Millour, F. Montmessin, and A. Maattanen, 2014. Global climate modeling of the Martian water cycle with improved microphysics and radiatively active water ice clouds, *Journal of Geophysical Research: Planets*, 119, 1479-1495.

Newman, C. E., S. R. Lewis, P. L. Read, and F. Forget (2002), Modeling the Martian dust cycle, representations of dust transport processes, *Journal of Geophysical Research: Planets*, 107 (E12), 6–1.

Nier, A., and M. B. McElroy (1977), Composition and structure of Mars' upper atmosphere: Results from the neutral mass spectrometers on Viking 1 and 2, *Journal of Geophysical Research*, 82 (28), 4341–4349.

Pankine, A. A., L. K. Tamppari, and M. D. Smith (2010), MGS TES observations of the water vapor above the seasonal and perennial ice caps during northern spring and summer, *Icarus*, 210 (1), 58–71.

Parkinson, T., and D. Hunten (1972), Spectroscopy and acronomy of O_2 on Mars, *Journal of the Atmospheric Sciences*, 29 (7), 1380–1390.

Pätzold, M., S. Tellmann, B. Hausler, D. Hinson, R. Schaa, and G. Tyler (2005), A sporadic third layer in the ionosphere of Mars, *Science*, 310 (5749), 837–839.

Perrier, S., J.-L. Bertaux, F. Lefévre, S. Lebonnois, O. Korablev, A. Fedorova, and F. Montmessin (2006), Global distribution of total ozone on Mars from SPICAM/MEX, UV measurement *Journal of Geophysical Research: Planets*, 111 (E9).

Pollack, J. B., D. S. Colburn, F. M. Flasar, R. Kahn, C. Carlston, and D. Pidek (1979),

Properties and effects of dust particles suspended in the Martian atmosphere, *Journal of Geophysical Research*: Solid Earth, 84 (B6), 2929–2945.

Read, Peter L. and Lewis, Stephen R., 2004. The Martian climate revisited: atmosphere and environment of a desert planet, Springer Praxis Books: *Geophysical Sciences* 26.

Richardson, M. I., and R. J. Wilson (2002), Investigation of the nature and stability of the Martian seasonal water cycle with a general circulation model, *Journal of Geophysical Research: Planets*, 107 (E5), 7–1.

Rodrigo, R., E. Garcia-Alvarez, M. Lopez-Gonzalez, and J. Lopez-Moreno (1990), A nonsteady one-dimensional theoretical model of Mars' neutral atmospheric composition between 30 and 200 km, *Journal of Geophysical Research*: Solid Earth, 95 (B9), 14,795–14,810.

Reus, M. de, H. Fischer, R. Sander, Valérie Gros, R. Kormann, G. Salisbury, R. Van Dingenen, J. Williams, M. Zöllner, and J. Lelieveld (2005), "Observations and model calculations of trace gas scavenging in a dense Saharan dust plume during MINATROC." *Atmospheric Chemistry and Physics* 5, 1787-1803.

Schofield, J., J. R. Barnes, D. Crisp, R. M. Haberle, S. Larsen, J. Magalhaes, J. R. Murphy, A. Seiff, and G. Wilson (1997), The Mars Pathfinder atmospheric structure investigation/ meteorology (ASI/MET) experiment, *Science*, 278 (5344), 1752–1758.

Sander, S. P., et al., 2003. Chemical kinetics and photochemical data for use in atmospheric studies, Evaluation number 14, JPL Publ. 02-25, *Jet Propul. Lab.*, Pasadena, Calif.

Schunk, R., and A. Nagy (2009), Ionospheres: physics, plasma physics, and chemistry, *Cambridge university press*.

Seiff, A., and D. B. Kirk (1977), Structure of the atmosphere of Mars in summer at midlatitudes, *Journal of Geophysical Research*, 82 (28), 4364–4378.

Sheel, V., and S. A. Haider (2012), Calculated production and loss rates due to impact of galactic cosmic rays in the lower ionosphere of Mars, *Planet. Space Sci*., 63, 94–104.

Sheel, V., and S. Haider (2016), Long-term variability of dust optical depths on Mars during MY24–MY32 and their impact on subtropical lower ionosphere: Climatology, modeling, and observations, *Journal of Geophysical Research: Space Physics*, 121 (8), 8038–8054.

Shimazaki, T. (1981), A model of temporal variations in ozone density in the Martian atmosphere, *Planetary and Space Science*, 29 (1), 21–33.

Shimazaki, T. (1986), Minor constituents in the middle atmosphere, *vol. 6, Springer*.

Shimazaki, T., and M. Shimizu (1979), The seasonal variation of ozone density in the Martian atmosphere, *Journal of Geophysical Research: Space Physics*, 84 (A4), 1269–1276.

Serdyuchenko, A., Gorshelev, V., Weber, M., Chehade, W., Burrows, J.P., 2014. High spectral resolution ozone absorption cross-sections – Part 2: temperature dependence. *Atmos. Meas. Tech*. 7, 625–636.

Sindoni, G., V. Formisano, and A. Geminale (2011), Observations of water vapour and carbon monoxide in the Martian atmosphere with the SWC of PFS/MEX, *Planet. Space Sci.*, 59 (2-3), 149–162.

Smith, D. E., et al. (2001a), Mars Orbiter Laser Altimeter: Experiment summary after the first year of global mapping of Mars, *Journal of Geophysical Research: Planets*, 106 (E10), 23,689–23,722.

Smith, M. D. (2002), The annual cycle of water vapor on Mars as observed by the thermal emission spectrometer, *Journal of Geophysical Research: Planets*, 107 (E11), 25–1.

Smith, M. D. (2004), Interannual variability in TES atmospheric observations of Mars during 1999–2003, *Icarus*, 167 (1), 148–165.

Smith, M. D. (2009), THEMIS observations of Mars aerosol optical depth from 2002–2008, *Icarus*, 202 (2), 444–452.

Smith, M. D., J. C. Pearl, B. J. Conrath, and P. R. Christensen (2001b), Thermal Emission Spectrometer results: Mars atmospheric thermal structure and aerosol distribution, *Journal of Geophysical Research: Planets*, 106 (E10), 23,929–23,945.

Smith, M. D., M. J. Wolff, R. T. Clancy, and S. L. Murchie (2009), Compact Reconnaissance Imaging Spectrometer observations of water vapor and carbon monoxide, *Journal of Geophysical Research: Planets*, 114 (E2).

Sneep, M., Ubachs, W., (2005), Direct measurement of the Rayleigh scattering cross section in various gases. *J. Quant. Spectrosc. Radiat. Transf.* 92, 293–310.

Spinrad, H., G. Munch, and L. D. Kaplan (1963), Letter to the editor: the detection of water vapor on Mars, *The Astrophysical Journal*, 137, 1319.

Sprague, A., D. Hunten, R. Hill, B. Rizk, and W. Wells (1996), Martian water vapor, 1988–1995, *Journal of Geophysical Research: Planets*, 101 (E10), 23,229–23,241.

Sprague, A. L., et al. (2007), Mars' atmospheric argon: Tracer for understanding Martian atmospheric circulation and dynamics, *Journal of Geophysical Research: Planets*, 112 (E3).

Stock, J. W., Boxe, C. S., Lehmann, R., Grenfell, J. L., Patzer, A. B. C., Rauer, H., & Yung, Y. L. (2012). Chemical pathway analysis of the Martian atmosphere: CO_2-formation pathways. *Icarus*, *219*(1), 13-24.

Thalman, R., K. J. Zarzana, M. A. Tolbert, and R. Volkamer (2014), Rayleigh scattering cross-section measurements of nitrogen, argon, oxygen and air, *J. Quant. Spectrosc. Radiat. Transfer*, 147, 171–177.

Tillman, J. E., L. Landberg, and S. E. Larsen (1994), The boundary layer of Mars: Fluxes, stability, turbulent spectra, and growth of the mixed layer, *Journal of. Atmospheirc Science.*, 51 (12), 1709–1727.

Tsang, W., and R. F. Hampson, 1986. Chemical kinetic data base for combustion chemistry. Part I. Methane and related compounds, *J. Phys. Chem. Ref. Data*, 15, 1087–1279.

Tschimmel, M., N. Ignatiev, D. Titov, E. Lellouch, T. Fouchet, M. Giuranna, and V. Formisano (2008), Investigation of water vapor on Mars with PFS/SW of Mars Express, *Icarus*, 195 (2), 557–575.

Webster, Christopher R., et al., (2013) "Low upper limit to methane abundance on Mars." *Science* 342.6156, 355-357.

Webster, C. R., et al. (2015), Mars methane detection and variability at Gale crater, *Science*, 347 (6220), 415–417.

Whitten, R., I. Poppoff, and J. Sims (1971), The ionosphere of Mars below 80 km altitude–I quiescent conditions, *Planetary and Space Science*, 19 (2), 243–250.

Willame, Y., A. Vandaele, C. Depiesse, F. Lefévre, V. Letocart, D. Gillotay, and F. Montmessin (2017), Retrieving cloud, dust and ozone abundances in the Martian atmosphere using SPICAM/ Journal of Geophysical Research: Space Physics nadir spectra, *Planetary and Space Science*, 142, 9–25.

Withers, P. (2009), A review of observed variability in the dayside ionosphere of Mars, *Advances in Space Research*, 44 (3), 277–307.

Withers, P., M. Felici, M. Mendillo, L. Moore, C. Narvaez, M. Vogt, and B. Jakosky (2018), First ionospheric results from the MAVEN Radio Occultation Science Experiment (ROSE), *Journal of Geophysical Research: Space Physics*, 123 (5), 4171–4180.

Wolff, M., M. Smith, R. Clancy, R. Arvidson, M. Kahre, F. Seelos, S. Murchie, and H. Savijärvi (2009), Wavelength dependence of dust aerosol single scattering albedo as observed by the Compact Reconnaissance Imaging Spectrometer, *Journal of Geophysical Research: Planets*, 114 (E2).

Wolff, M. J., and R. T. Clancy (2003), Constraints on the size of Martian aerosols from thermal emission spectrometer observations, *Journal of Geophysical Research: Planets*, 108 (E9).

Wolff, M. J., et al. (2006), Constraints on dust aerosols from the Mars exploration rovers using MGS overights and mini-TES, *Journal of Geophysical Research: Planets*, 111 (E12).

Wolff, M. J., R. T. Clancy, J. D. Goguen, M. C. Malin, and B. A. Cantor (2010), Ultraviolet dust aerosol properties as observed by MARCI, *Icarus*, 208 (1), 143–155.

Wong, A.S., Atreya, S.K., Encrenaz, T., (2003). Chemical marker of possible hot spots on Mars. *Journal of Geophysical Research*, 108 (E4), 5026,

Yung, Y. L., D. F. Strobel, T. Y. Kong, and M. B. McElroy (1977), Photochemistry of nitrogen in the Martian atmosphere, *Icarus*, 30 (1), 26–41.

List of Publications/Proceedings

Refereed Journal Publications

1. Retrieval of Martian ozone and dust from SPICAM spectrometer for MY27-MY28 Ashimananda Modak, Varun Sheel and Franck Montmessin (2019), *Journal of Earth Science System* (Accepted on January 14, 2019).

Presentations at conferences

1. Title: Competitive Chemical Processes in Mars' Atmosphere. Brain Storming Session on Vision & Explorations for Planetary Sciences in Decades 2020-2060, Physical Research Laboratory, Ahmedabad, INDIA, 8th -10th November 2017.

2. Loss Mechanism of odd Oxygen in the Photochemistry of Martian Atmosphere. 20th National Science Symposium, 29-31 Jan, 2019, Pune.

Publication attached with the thesis

1. Retrieval of Martian ozone and dust from SPICAM spectrometer for MY27-MY28 Ashimananda Modak, Varun Sheel and Franck Montmessin (2019), *Journal of Earth Science System* (Accepted on January 14, 2019).